TAMPEREEN TEKNILLINEN YLIOPISTO
TAMPERE UNIVERSITY OF TECHNOLOGY

Jouni Mäkitalo

Boundary Integral Operators in Linear and Second-order Nonlinear Nano-optics

Julkaisu 1297 • Publication 1297

Tampere 2015

Tampereen teknillinen yliopisto. Julkaisu 1297
Tampere University of Technology. Publication 1297

Jouni Mäkitalo

Boundary Integral Operators in Linear and Second-order Nonlinear Nano-optics

Thesis for the degree of Doctor of Science in Technology to be presented with due permission for public examination and criticism in Sähkötalo Building, Auditorium S2, at Tampere University of Technology, on the 29th of May 2015, at 12 noon.

Tampereen teknillinen yliopisto - Tampere University of Technology
Tampere 2015

ISBN 978-952-15-3522-2 (printed)
ISBN 978-952-15-3539-0 (PDF)
ISSN 1459-2045

To Suvi

Abstract

Recent advances in the fabrication of nanoscale structures have enabled the production of almost arbitrarily shaped nanoparticles and so-called optical metamaterials. Such materials can be designed to have optical properties not found in nature, such as negative index of refraction. Noble metal nanostructures can enhance the local electric field, which is beneficial for nonlinear optical effects. The study of nonlinear optical properties of nanostructures and metamaterials is becoming increasingly important due to their possible uses in nanoscale optical switches, frequency converters and many other devices.

The responses of nanostructures depend heavily on their geometry, which calls for versatile modeling methods. In this work, we develop a boundary element method for the modeling of surface second-harmonic generation from isolated nanoparticles of very general shape. The method is also capable of modeling spatially periodic structures by the use of appropriate Green's function. We further show how to utilize geometrical symmetries to lower the computational time and memory requirements in the boundary element method even in cases where the incident field is not symmetrical.

We validate the boundary element approach by the calculation of second-harmonic scattering from gold spheres of different radii. Comparison to analytical solution reveals that under one percent relative error is easily achieved. The method is then applied to model second-harmonic microscopy of single gold nanodots and second-harmonic generation from arrays of L- and T-shaped gold particles. The agreement between the calculations and measurements is shown to be excellent.

To provide a more intuitive understanding of the optical response of nanostructures, we develop a full-wave spectral approach, which is based on boundary integral operators. We present a theory which proves that the resonances of a smooth scatterer are isolated poles that occur at complex frequencies. Other types of singularities, such as branch-cuts, may occur only via the fundamental Green function or material dispersion. We propose a definition of an eigenvalue problem at fixed real frequencies which gives rise to modes defined over the surface of the scatterer. We illustrate that these modes accurately describe the optical responses that are usually seen for certain particle shapes when using plane-wave excitations. With the spectral approach, the resonance frequencies and the modal responses of a scatterer can be found as intrinsic properties independent of any incident field. We show that the spectral theory is compatible with the Mie theory for spherical particles and with a previously studied quasi-static theory in the limit of zero frequency.

Preface

This research was carried out in the Optics Laboratory of Tampere University of Technology during the years 2011 – 2015. The research was an extension of the work done as research assistant during 2008 – 2011 and the resulting Master's Thesis. I acknowledge the Graduate School of Tampere University of Technology for the funding that made the research work possible. I also acknowledge the Emil Aaltonen foundation and the Finnish Foundation for Technology Promotion for personal grants.

I thank my supervisor, Professor Martti Kauranen for accepting me as part of his research group and for his positive attitude and his ability to give constructive feedback very quickly. I'm especially grateful for his support towards pursuing my own ideas at will. Equally, I thank University Lecturer Saku Suuriniemi for being the co-supervisor of my research work. Your guidance and expertise have been invaluable.

I wish my deepest gratitude to all co-workers that have made this Thesis possible. I thank my co-authors Mikko, Godofredo, Robert, Hannu, Roope, Juha, Janne, Markku and Joonas for your efforts in our joint research work. I especially value the many insightful moments with Mikko, Godofredo, Robert and Hannu. I thank my long-term office mate Matti and our lunch reinforcement Topi for all the delightful discussions on science and beyond. My sincere gratitude goes for all the current and past lab members. Specifically I thank Abdallah and Harri for our ongoing research work. I also thank the present and past department staff, namely Ari, Hanna, Inkeri, Jaana, Katriina and Teemu for taking care of the practicalities. You all have made the atmosphere outright brilliant.

I thank my family for the sincere love and support that have helped me through the years. Most of all, I thank my wife Suvi for being the greatest partner one could hope for. You and our newborn daughter make me see life as the joyful ride it is.

Tampere, May 2015

Jouni Mäkitalo

Contents

Acronyms

ACA	adaptive cross-approximation
BEM	boundary element method
BVP	boundary value problem
CFIE	combined field integral equation
EFIE	electric field integral equation
EMP	electromagnetic pulse
FDTD	finite-difference time-domain
FMM	fast multipole method
GMRES	general minimal residual
LAPACK	linear algebra package
MFIE	magnetic field integral equation
MOM	method of moments
PDE	partial differential equation
PMCHWT	Poggio-Miller-Chang-Harrington-Wu-Tsai
RWG	Rao-Wilton-Glisson
SEM	singularity expansion method
SHG	second-harmonic generation
TE	transverse-electric
THG	third-harmonic generation
TM	transverse-magnetic

Glossary

This glossary lists the most common mathematical symbols appearing in this Thesis. Scalars are in italics (a), vectors are bold roman ($\mathbf{a}$), matrices are capital roman (A) and linear operators are calligraphic $\mathscr{A}$. Time-varying quantities are denoted by $\sim$ on top ($\tilde{a}$).

α	relative solid angle
$\mathscr{A}$	compact operator
$\mathbf{A}$	scattering amplitude
$\mathbf{B}$	magnetic induction
$\chi^{(n)}$	nonlinear electric susceptibility of order n
χ^{s}	second-order nonlinear surface susceptibility
∂	boundary operator
δ	delta distribution
$\mathbf{D}$	electric displacement
$\mathscr{D}$	hypersingular boundary integral operator
$\mathbf{E}$	electric field
$\mathbf{E}_{\mathrm{inc}}$	incident electric field
$\mathbf{E}_{\mathrm{s}}$	scattered electric field
ϵ	electric permittivity
e_r	relative error
η	wave impedance
γ_r	tangential rotating trace operator
γ_t	tangential trace operator
$\mathbf{G}$	dyadic Green's function
G	scalar Green's function
$\mathfrak{G}$	group
$\mathbf{H}$	magnetic field
$\mathbf{H}_{\mathrm{inc}}$	incident magnetic field
$\mathbf{H}_{\mathrm{s}}$	scattered magnetic field
$\mathcal{H}^{-1/2}$	fractional order Sobolev space
i	imaginary unit
$\mathbf{I}$	identity dyad
$\mathscr{I}$	identity operator
$\Im$	imaginary part of complex number
$\langle \cdot, \cdot \rangle$	inner-product
$\mathbf{J}$	electric current density
$\mathbf{J}^{\mathrm{s}}$	electric surface current density
k	wave number
$\mathscr{K}$	compact boundary integral operator

$\mathbb{L}^2$	Hilbert space of square-integrable functions
$\mathbf{L}$	angular momentum operator
$\mathscr{L}$	linear operator
$\mathbf{M}$	magnetic current density
$\mathbf{M}^{\mathrm{s}}$	magnetic surface current density
μ	magnetic permeability
∇	gradient
$\nabla\cdot$	divergence
$\nabla\times$	curl
n_g	order of group element g
$n_{\mathfrak{G}}$	group order
$\lvert\cdot\rvert$	norm
$\mathbf{n}$	normal vector of unit length
ω	angular frequency ($2\pi\times$ frequency)
$\mathbf{P}^{\mathrm{nl}}$	nonlinear polarization
$\mathcal{P}$	nonlinear surface polarization
R	Euclidean distance between two points
$\Re$	real part of complex number
ρ	electric charge density
ρ_m	magnetic charge density
$\boldsymbol{\rho}$	lattice translation vector
$\mathbf{r}$	position
$\hat{\mathbf{r}}$	position vector of unit length
σ	cross-section
σ_{a}	absorption cross-section
σ_{e}	extinction cross-section
σ_{s}	scattering cross-section
$\mathbf{S}$	Poynting vector
$\frac{\partial f}{\partial t}$	time derivative of function f
V	solution domain, subset of $\mathbb{R}^3$
$\mathbf{X}$	vector spherical harmonic
$\mathbf{x}, \mathbf{y}, \mathbf{z}$	Cartesian basis vectors of unit length
Y	scalar spherical harmonic

List of figures

List of publications

I J. Mäkitalo, S. Suuriniemi and M. Kauranen. Boundary element method for surface nonlinear optics of nanoparticles. Optics Express, **19**, 23386 – 23399 (2011). Erratum **21**, 10205 – 10206 (2013).

II J. Mäkitalo, M. Kauranen and S. Suuriniemi. Modes and resonances of plasmonic scatterers. Physical Review B, **89**, 165429 (2014).

III J. Mäkitalo, S. Suuriniemi and M. Kauranen. Enforcing symmetries in boundary element formulation of plasmonic and second-harmonic scattering problems. Journal of the Optical Society of America A, **31**, 2821 – 2832 (2014).

IV G. Bautista, M. J. Huttunen, J. Mäkitalo, J. M. Kontio, J. Simonen and M. Kauranen. Second-harmonic generation imaging of metal nano-objects with cylindrical vector beams. Nano Letters, **12**, 3207 – 3212 (2012).

V R. Czaplicki, J. Mäkitalo, R. Siikanen, H. Husu, J. Lehtolahti, M. Kuittinen and M. Kauranen. Second-harmonic generation from metal nanoparticles: resonance enhancement versus particle geometry. Nano Letters, **15**, 530 – 534 (2015).

1 Introduction

Nano-optics is the science of optical phenomena at and beyond the diffraction limit of light. Its roots can be traced back to 1928 when a sub-wavelength near-field optical microscope was proposed by Synge[1]. Due to technical challenges, the first practical implementations of such microscopes took place in the early 1980's, which led to increasing interest towards optics at the nanoscale[2]. More recent advances in other nanosciences and nanotechnologies have increased the need for optical imaging and characterization techniques for nanoscale objects. On the other hand, nanolithographic fabrication techniques have enabled the study of the interaction of light with tailored nanostructures.

One of the most prominent branches of nano-optics is plasmonics, the study of the optical properties of noble metal surfaces and nanoparticles[3]. Light incident on such structures induces coherent oscillations of the conduction electron gas, i.e., plasmons. These oscillations exhibit resonances that depend on the size, shape and material of the structure as well as the environment[4]. The resonances dictate the optical properties of, e.g., liquid suspensions of plasmonic particles. This was already utilized by the ancient Romans, who were able to mix gold and silver nanoparticles in glass to produce items with vivid colors. This technique was also used to fabricate the stained glass of Notre Dame. The plasmon resonances lead to enhancement of the local electric field, which is then sensitive to changes in the properties of the particle and its environment. Consequently, this has lead to the development of near-field sensors, culminating in the detection of single molecules[5].

Nanolithographic fabrication methods have enabled the tailoring of nanoparticles and arrays of such particles, which can be used to create so-called optical metamaterials[6]. Such materials can have optical properties that do not occur in nature, e.g., negative index of refraction and the properties usually arise from the structure instead of composition[7]. These materials hold promise for many applications, such as the perfect lens[8], optical cloaking[9] and hyperbolic materials[10].

The ability to fabricate increasingly complex nanostructures has introduced the need for accurate modeling of their optical responses. Numerical electromagnetic modeling dates back to the earliest days of computers and has been strongly driven by the desire to improve radars and antennas and to study scattering cross-sections of conducting bodies. The Mie theory of light scattering from a sphere, reported in 1908, has provided the basis for a simplified understanding of light scattering from nanoparticles in general[11,12]. However, its predictive power for distinctly non-spherical particles is limited, which calls for more general-purpose methods. The seminal paper by Yee in 1966 introduced the finite-difference time-domain (FDTD) method[13] for the direct discretization of the Maxwell partial differential equations (PDEs). However, its efficient application to scattering problems became truly appealing only after the development of perfectly matched layers

by Berenger in 1996.[14]

The method of moments (MOM) discretization of integral operator equations that arise from the Maxwell PDEs was first described carefully by Harrington in his classical book[15] in 1968, although the use of MOM must well predate the book. The first practical applications of MOM for open domain problems were limited to thin wire structures (Pocklington's and Halle's equations) and bodies of revolution[16]. However, the rapid development of computers in the past decades has enabled the modeling of complex 3D structures[17,18]. The numerical performance of integral operator methods was significantly improved by Greengard and Rokhlin in 1987 by the development of the fast multipole method (FMM)[19–21].

This work applies boundary integral operators and the MOM to the study of the linear and the nonlinear optical properties of nanoparticles. The nonlinear optical effects were first observed in 1961, almost immediately after the first demonstration of a laser[22]. These effects occur when the intensity of light is extremely high, leading to a myriad of optical responses, such as harmonic generation and intensity-dependent refractive index[23]. However, nonlinear effects are inherently weak and scale as powers of the electric field intensity. Due to the local electric field enhancement by plasmonic nanoparticles, the study of nonlinearity in nanoparticles and nonlinear metamaterials has received growing interest in recent years[24,25].

1.1 Aims and scope of this work

Scattering of light from particles is a broad topic and can be described from many points of view. Interaction of light with macroscopic objects, such as lenses, mirrors and even large water droplets, can often be described satisfactorily by geometrical optics, where the wave nature is neglected, i.e., light propagates without diffraction. From the quantum-mechanical point of view, light can be understood as a stream of photons, each having quantum of energy and momentum. Scattering from material bodies is then described by excitation of virtual electronic states and re-emission of photons. Scattering from nanoparticles is a domain where it may be difficult to identify the most successful model. Surprisingly, an electromagnetic wave-propagation model, where the constitutive relations describe the light-matter interaction averaged over atomic dimensions, is quite successful in modeling the scattering of light from particles with linear dimensions exceeding a few nanometers. The methods for modeling such wave propagation depend on the ratio of geometrical dimensions to wavelength. This Thesis focuses on electromagnetic scattering from particles, whose dimensions are on the order of wavelength. Additionally, field enhancement due to plasmon resonances and sharp geometrical features is considered important.

The Thesis also studies the parametric nonlinear scattering response of nanoparticles. The focus is on surface second-harmonic generation from nanoparticles made of materials with centrosymmetric crystal structure, although bulk effects from multipolar microscopic light-matter interactions are also discussed. The nonlinear effects are considered in the undepleted-pump approximation, because these effects are inherently weak in nanoparticles. The numerical schemes will consequently be substantially less time consuming. Some of the discussed methods are also easily extended for modeling other nonlinear effects, such as bulk second-harmonic generation (SHG) and third-harmonic generation (THG).

When the Author joined the Nonlinear Optics Group in 2008 as a research assistant, the group had already carried out several pioneering experimental and theoretical studies

of the second-order nonlinear response of metal surfaces and nanoparticles. The recent findings regarding surface SHG from arrays of T-shaped gold nanoparticles were strikingly nontrivial and it was clear at the time that modeling of such a response would be essential for gaining further understanding [26]. Even before this study, it had been found that fabrication defects had a notable effect on SHG from L-shaped particles [27]. It also became clear that understanding even the linear optical properties of such nanoparticles required more detailed modeling and theory. Other nanoparticle shapes, such as rods [28], triangles [29], rings [30], shells [31], split-rings [32,33], dimers [34], oligomers [35] and dolmens [36], have also been studied by other groups, but for the study of SHG, the simplest non-centrosymmetric shapes, such as L- and T-shapes, have offered the most straightforward starting point.

Initially, the group relied on an implementation of the Fourier modal method to model the linear scattering from arrays of nanoparticles. While the method appeared to be ideal for periodic structures, it was unsuitable for modeling the near-fields of metal structures with adequate precision. Furthermore, the group had not yet established an in-depth understanding of electromagnetic modeling methods on both theoretical and algorithmic level. To gain more understanding of numerical schemes and to model the near fields more accurately, the Author started implementing an FDTD algorithm. This led to some useful modeling results explaining the linear response of L-shaped nanoparticles [37]. However, it was realized that FDTD would not be suitable for modeling surface SHG due to the coarse representation of geometry. Furthermore, the modeling of material dispersion, spatial periodicity, open domains and focused Gaussian-beam sources was inherently difficult in FDTD. In response to the increasing interest towards the full-wave boundary element method (BEM) in the field of plasmonics [38–44], the Author dedicated his Master's thesis for the study and implementation of BEM. The driving motivation was that BEM would be ideal for modeling surface SHG. This was then set as the first main goal of this Thesis.

General purpose software has long been available for the solution of electromagnetic boundary value problems (BVPs). During the research work presented in this Thesis, software such as Comsol and Lumerical have been equipped with functionality for optical scattering simulations and thus have started to gain popularity in nano-optical research. In the beginning of the Author's work, it was very common for researchers in nano-optics and plasmonics to author their own modeling tools, as the available software was considered too immature. Even though today it is advisable to take advantage of the well-tested established software, the Author's approach to write the code himself has given invaluable understanding of the methods and complete control over the modeling tools. The most striking advantage of this approach was the capability to study the plasmon resonance and mode theory in a novel way via boundary integral operators. This formed the second main goal of this research.

In this Thesis, the Author will demonstrate the effectiveness and robustness of BEM for the modeling of surface SHG from metal/plasmonic nanoparticles in isolation and in arrays. The method is evaluated by comparing its results to analytical solution for a spherical particle and by comparing to experimental data. Consequently, the method developed by the Author has already been evaluated by peers by applying it to model various systems. The topic has also become very timely as several research groups have shown interest in similar modeling approaches. In addition, the Thesis outlines the theory of modes and resonances of scatterers to give a more fundamental and mathematically precise understanding of scattering from nanoparticles in general.

1.2 Structure of the Thesis

This Thesis outlines the work presented in five peer-reviewed articles on the modeling of surface SHG and on the theory of modes and resonances of nanoparticles. Chapter 2 covers the fundamentals of electromagnetic theory and nonlinear optics. SHG in centrosymmetric media is discussed in detail with the introduction of the interface conditions. The chapter is concluded with the theory of plasmons and material dispersion of noble metals.

Chapter 3 is devoted to the theory of scattering and diffraction of electromagnetic waves from isolated particles and particle arrays. The scattering problem is formulated precisely by giving a proper notion of constraints for the geometry and function spaces. The Green functions and Stratton-Chu integral operators are introduced and used for reformulating the scattering problem in terms of integral equations. Finally, the boundary integral formulation of surface SHG is presented.

Chapter 4 introduces the spectral theory of Hilbert spaces combined with the theory of analytic and meromorphic functions to take a novel perspective on the modes and resonances of plasmonic scatterers. A boundary integral operator formulation of the scattering problem is used to obtain a mathematically precise definition for resonances and modes. The resonances and modes are then unambiguously identified as intrinsic properties of a scatterer. The theory is shown to reduce to the Mie theory in the case of spherical particles and to the well-understood quasi-static theory in the limit of zero frequency.

Chapter 5 begins by presenting the multipole solutions to linear and surface second-harmonic scattering from spheres. Then, the discretization of a boundary integral equation formulation via MOM and Rao-Wilton-Glisson (RWG) basis functions is presented and its performance is evaluated by comparison to exact results for a sphere. The method is applied to model second-harmonic microscopy of isolated nanodots and to model the second-harmonic response of L- and T-shaped nanoparticles.

Chapter 6 is devoted to symmetry in electromagnetic BVPs. Symmetry predicates are derived for the quantities of interest in boundary integral formulations and the utilization of geometrical symmetry in BEM is presented.

In Chapter 7, conclusions from the work are drawn and an outlook for future improvements and advances for the methods and theory is given.

1.3 Author's contribution

The research of the Thesis has been published in five papers. **Paper I** presents the first main goal of the Thesis: the boundary element method for surface SHG. In **Paper II**, the theory and numerical modeling of modes and resonances of plasmonic scatterers is presented, completing the second main goal of the Thesis. **Paper III** governs the utilization of geometrical symmetry in linear and surface second-harmonic scattering problems. In **Papers IV and V**, BEM is applied to model experiments on surface SHG from gold nanostructures.

Paper I This paper presents a boundary integral operator formulation of surface SHG from isolated nanoparticles, which is suitable for plasmonic scatterers under resonant conditions. The equations are discretized by MOM with the use of RWG basis functions and Galerkin's testing. A semi-analytical solution is derived for spherical particles by the use of multipoles that result from separation of variables. This solution is used to estimate the accuracy of the integral operator approach. Second-harmonic radiation properties of an isolated gold L-shaped particle are studied as an example.

Paper II This paper presents the theory of resonances and modes of plasmonic scatterers through boundary integral operators. It is shown that the Müller formulation allows the use of the Fredholm operator theory to show that the plasmon resonances correspond to isolated poles of the inverse integral operator. A modal expansion of solutions is presented. The theory is shown to be compatible with the Mie theory for spherical particles and with the well-understood quasistatic theory in the zero-frequency limit. Resonances and modes of a gold disk, a bar and a disk dimer are studied numerically.

Paper III In this paper, it is shown how geometrical symmetry of scatterers can be utilized in BEM to lower the required computation time and memory even if the excitation is not symmetrical. The paper shows that symmetry can also be utilized in BEM for surface SHG. The use of symmetry and modeling of surface SHG is considered for an arbitrary number of scatterers, which may also be in contact. The method is used to model the linear and second-order responses of multiply split gold nanorings.

Paper IV This paper describes the microscopic second-harmonic imaging of gold nanodots and nanocones by linearly, radially and azimuthally polarized tightly focused Gaussian beams. The experimental results show that the use of SHG can reveal minute differences in the microscopy images of the structures, even though the precision of the image itself is diffraction limited. The BEM simulations agree qualitatively with the findings and are used to assess the shape of defects.

Paper V In this paper, SHG from arrays of L- and T-shaped gold nanoparticles is investigated experimentally and computationally. It is shown that the diffracted SHG does not depend trivially on the resonances of the structures: sometimes it may be favourable to avoid resonant excitation in order to induce asymmetry in the local response and consequently amplify the far-field signal. The BEM modeling of both linear and second-order responses display unprecedented agreement with experimental results.

As is common in scientific research, the published work is the result of collaboration. In this case, the Author has had the privilege to work with theoreticians to develop the mathematical tools and with experimentalists to apply the tools to actual existing problems. Table 1.1 shows the Author's contributions to each published article. The contributions listed are divided into three categories relevant to the nature of the Author's work. The **preparation** consists of discovering the scientific problem and planning out the research strategy to address the problem. The **theory and calculations** category consists of working out the required theory, the formulation of the model, a computer implementation of solution methods for the model, and running the required calculations. The **reporting** category includes writing the manuscript, plotting the results and handling the manuscript submission.

Table 1.1: Summary of author's contribution to articles included in this Thesis.

Paper	**Preparation**	**Theory and calculations**	**Reporting**
I	50 %	80 %	80 %
II	80 %	70 %	80 %
III	80 %	60 %	70 %
IV	10 %	100 %	20 %
V	10 %	100 %	30 %

2 Electromagnetic theory and nonlinear optics

This Chapter presents the fundamental electromagnetic theory that provides the starting point for the forthcoming integral operator developments. We introduce the Maxwell equations and constitutive relations with focus on nonlinear optical response and metals at optical frequencies.

2.1 Maxwell's equations and constitutive relations

Since the ground-breaking treatise on electricity and magnetism by James Clerk Maxwell in 1873, the classical electromagnetism has been understood on the basis of Maxwell's equations[45]. In the differential operator form and the SI units, they are

$$\nabla \times \tilde{\mathbf{E}} = -\frac{\partial \tilde{\mathbf{B}}}{\partial t}, \tag{2.1}$$

$$\nabla \times \tilde{\mathbf{H}} = \tilde{\mathbf{J}} + \frac{\partial \tilde{\mathbf{D}}}{\partial t}, \tag{2.2}$$

$$\nabla \cdot \tilde{\mathbf{D}} = \tilde{\rho}, \tag{2.3}$$

$$\nabla \cdot \tilde{\mathbf{B}} = 0. \tag{2.4}$$

Here the electric field $\tilde{\mathbf{E}}$, the electric displacement $\tilde{\mathbf{D}}$, the magnetic field $\tilde{\mathbf{H}}$, the magnetic induction $\tilde{\mathbf{B}}$, the electric current density $\tilde{\mathbf{J}}$ and the electric charge density $\tilde{\rho}$ are time-dependent macroscopic quantities that average the responses over atomic dimensions. It follows directly from Eqs. (2.2) and (2.3) that $\nabla \cdot \tilde{\mathbf{J}} = -\frac{\partial \tilde{\rho}}{\partial t}$ holds, which is a statement of conservation of charge.

Let us assume that the field quantities can be expanded in terms of complex Fourier components with respect to time. Because the time-domain fields are real-valued, their Fourier spectra are conjugate-symmetric. If we denote the Fourier component of $\tilde{\mathbf{E}}$ with frequency ω by $\mathbf{E}(\omega)$, then the time-domain field is obtained by summing over or integrating $\mathbf{E}(\omega)\exp(-i\omega t) + \mathbf{E}^*(\omega)\exp(i\omega t)$ over non-negative real ω.[§]

For each time-harmonic component with implied time-dependence $\exp(-i\omega t)$, which we

[§]The Fourier component $\mathbf{E}$ can actually be seen as a meromorphic function of complex ω. Its singularities in the complex plane determine its time-domain response via the Laplace transform.

adopt for the entirety of the Thesis, the Maxwell equations are

$$\nabla \times \mathbf{E} = i\omega\mathbf{B}, \tag{2.5}$$
$$\nabla \times \mathbf{H} = \mathbf{J} - i\omega\mathbf{D}, \tag{2.6}$$
$$\nabla \cdot \mathbf{D} = \rho, \tag{2.7}$$
$$\nabla \cdot \mathbf{B} = 0, \tag{2.8}$$

where the fields $\mathbf{E}, \mathbf{D}, \mathbf{H}, \mathbf{B}, \mathbf{J}$ are mappings from $\mathbb{R}^3$ to $\mathbb{C}^3$ and the charge density ρ is a mapping from $\mathbb{R}^3$ to $\mathbb{C}$.

The relations between the fields and flux densities and the fields and current densities are called the constitutive relations. If these relations are linear, any time-domain solution expandable in Fourier components can be solved in the frequency-domain for each component separately. Thus in principle, we may concentrate on formulating our electromagnetic problem for a single but arbitrary Fourier component.

In this work, we consider materials, whose constitutive relations can be written in the frequency-domain as[46]

$$\mathbf{D} = \epsilon\mathbf{E} + \mathbf{P}^{\mathrm{nl}}, \tag{2.9}$$
$$\mathbf{B} = \mu\mathbf{H}, \tag{2.10}$$

where $\epsilon, \mu : \mathbb{R}^3 \to \mathbb{C}$ are the spatially-varying electric permittivity and magnetic permeability with $\Im\epsilon, \Im\mu \geq 0$. The nonlinear polarization $\mathbf{P}^{\mathrm{nl}}$ describes the nonlinear optical material response, which is discussed in the next Section.

In principle, the current density may have the form $\mathbf{J} = \sigma\mathbf{E} + \mathbf{J}_0$, where $\sigma \in \mathbb{R}$ is the Ohmic conductivity and $\mathbf{J}_0$ is some *a priori* known driving current density. However, in the frequency domain, Ampère's law takes the form $\nabla \times \mathbf{H} = \mathbf{J}_0 + \sigma\mathbf{E} - i\omega\epsilon\mathbf{E} - i\omega\mathbf{P}^{\mathrm{nl}}$. This can be written as $\nabla \times \mathbf{H} = \mathbf{J}_0 - i\omega(\epsilon + i\sigma/\omega)\mathbf{E} - i\omega\mathbf{P}^{\mathrm{nl}}$, where $(\epsilon + i\sigma/\omega)$ may be considered as just another complex permittivity. Therefore we may, without loss of generality, assume that σ is part of $\Im\epsilon$. In scattering problems, the excitation is usually modeled as an incident field, although a localized current density $\mathbf{J}_0$ can also act as an excitation. In this work, we don't consider such current density excitations. In total, we may then set $\mathbf{J} = \mathbf{0}$ and $\nabla \times \mathbf{H} = -i\omega\epsilon\mathbf{E} - i\omega\mathbf{P}^{\mathrm{nl}}$.

2.2 Nonlinear parametric processes

The laser was first demonstrated in 1960 by Maiman[47]. A year after that, Franken *et al.* discovered that illumination of a sample with high-intensity laser light of certain frequency led to emission of light at doubled frequency[22]. This, so-called second-harmonic generation (SHG), is one example of nonlinear optical effects, which may occur if the incident light has sufficiently high intensity.

Such nonlinearities may often be described as parametric processes, where the nonlinear polarization assumes a series expansion[23]

$$\tilde{\mathbf{P}}^{\mathrm{nl}} = \epsilon_0(\chi^{(2)} : \tilde{\mathbf{E}}\tilde{\mathbf{E}} + \chi^{(3)} \vdots \tilde{\mathbf{E}}\tilde{\mathbf{E}}\tilde{\mathbf{E}} + \ldots), \tag{2.11}$$

where $\chi^{(n)}$ are electric susceptibility tensors of rank $n+1$. Nonlinear optical effects are inherently weak: typical values of $\chi^{(2)}$ are in the order of pm/V. With a nonlinear

constitutive relation, the electromagnetic analysis can no more be considered for the individual Fourier components separately. Assume that our incident electric field consists of two frequency components, i.e., $\tilde{\mathbf{E}} = 2\Re(\mathbf{E}_1 \exp(-i\omega_1 t) + \mathbf{E}_2 \exp(-i\omega_2 t))$. If we consider second-order nonlinearities, with $\chi^{(2)}$ non-zero, then the electric flux density will have components oscillating at frequencies $\omega_1, \omega_2, 2\omega_1, 2\omega_2, \omega_1 + \omega_2, \omega_1 - \omega_2$. This means that our solution for the electric field will contain all these frequency components. The terms corresponding to the last two components are called sum-frequency and difference-frequency generation, respectively.

In this work, we concentrate on SHG, where an incident field of single frequency ω gives rise to a field oscillating at frequency 2ω. In this case, both frequency components are subject to Maxwell's equations and are coupled by their constitutive relations

$$\mathbf{D}(\omega) = \epsilon(\omega)\mathbf{E}(\omega) + 2\epsilon_0\chi^{(2)} : \mathbf{E}(2\omega)\mathbf{E}^*(\omega), \tag{2.12}$$

$$\mathbf{D}(2\omega) = \epsilon(2\omega)\mathbf{E}(2\omega) + \epsilon_0\chi^{(2)} : \mathbf{E}(\omega)\mathbf{E}(\omega). \tag{2.13}$$

In general it may be the case that the second-harmonic field becomes so strong that the back-coupling term $2\epsilon_0\chi^{(2)} : \mathbf{E}(2\omega)\mathbf{E}^*(\omega)$ of Eq. (2.12) modifies the field at frequency ω, the so-called pump field or fundamental field. Then the pump field transfers significant amount of energy to the second-harmonic field and the pump field becomes depleted [23]. However, when considering SHG in nanoparticles, as is the case in the present work, the nonlinear interaction is usually so weak that depletion doesn't occur. Thus we may approximate that the constitutive relation (2.12) is simply $\mathbf{D}(\omega) = \epsilon(\omega)\mathbf{E}(\omega)$. This is the so-called undepleted-pump approximation [23]. In this case, the problem for the fundamental field is linear and can be solved for independently. Then, the term $\epsilon_0\chi^{(2)} : \mathbf{E}(\omega)\mathbf{E}(\omega)$ provides a one-way coupling to the second-harmonic field: it acts as an excitation for second-harmonic fields that satisfy linear constitutive relations.

2.3 SHG in centrosymmetric media

In the electric-dipole approximation of the light-matter interaction, all even-order nonlinear optical responses vanish in the bulk of materials of centrosymmetric crystal structure [48]. However, this symmetry is always broken on the surface, which gives rise to surface response, originating in an atomically thin layer [49].

The second-order surface response is described by a spatially varying susceptibility function $\chi^{(2)}$ that is a delta distribution over the material interface. Let the surface be characterized by the locus function Θ, which is a continuous function that maps a position to a scalar that is zero only over the surface. In the case of SHG in centrosymmetric materials, the second-order polarization is

$$\mathbf{P}^{(2)}(2\omega) = \epsilon_0\chi^{(2)} : \mathbf{E}(\omega)\mathbf{E}(\omega), \tag{2.14}$$

where $\chi^{(2)} = \delta \circ \Theta\chi^{\mathrm{s}}$ holds and χ^{s} is defined as the second-order susceptibility over the surface and $\circ$ denotes function composition, i.e., $(\delta \circ \Theta)(\mathbf{r})\ \forall \mathbf{r}$ is a delta distribution with respect to position $\mathbf{r}$. For brevity, we define the surface polarization as

$$\mathcal{P}(2\omega) = \epsilon_0\chi^{\mathrm{s}}\mathbf{E}(\omega)\mathbf{E}(\omega) \tag{2.15}$$

so that $\mathbf{P}^{(2)} = \delta \circ \Theta\mathcal{P}$ holds.

Because the normal component of the electric field may be discontinuous at material interfaces, the definition of the surface polarization is ambiguous. Clearly it cannot be

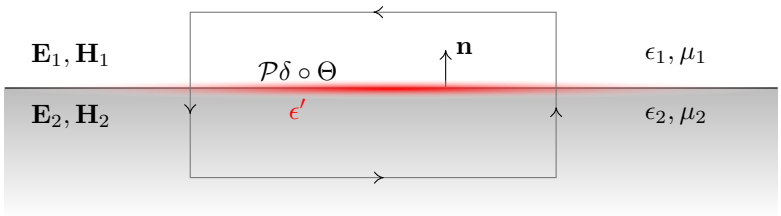

Figure 2.1: Planar interface between two media with surface polarization distribution. The loop path is used to construct interface conditions for **E** and **H**.

defined exactly on the interface. One may define that the polarization is located just inside either of the domains and the electric fields are evaluated either on the same side or the opposite. This choice fixes the value of χ^{s} but is not important otherwise. In this work, we agree to use the standard convention that the fields are evaluated inside the nonlinear material and the polarization is placed on the other side.

Consider two domains $V_1, V_2 \subset \mathbb{R}^3$ sharing a smooth interface S with unit-length normal vector $\mathbf{n}$ pointing into V_1. We may decompose the surface polarization into normal and tangential parts as

$$\mathcal{P} = \mathbf{n}\mathcal{P}_{\mathrm{n}} + \mathcal{P}_{\mathrm{t}}, \tag{2.16}$$

where $\mathcal{P}_{\mathrm{n}} = \mathcal{P} \cdot \mathbf{n}$ and $\mathcal{P}_{\mathrm{t}} = \mathbf{n} \times \mathcal{P} \times \mathbf{n}$ hold. Denote the electric and magnetic fields of frequency 2ω over domain V_1 by $\mathbf{E}_1, \mathbf{H}_1$ and over domain V_2 by $\mathbf{E}_2, \mathbf{H}_2$. By applying the Maxwell line-integral equations to a path illustrated in Fig. 2.1, a set of interface conditions can be derived for the electric and magnetic fields[49]:

$$(\mathbf{E}_1 - \mathbf{E}_2)_t = -\frac{1}{\epsilon'}\nabla_t \mathcal{P}_{\mathrm{n}}, \tag{2.17}$$

$$(\mathbf{H}_1 - \mathbf{H}_2)_t = -i(2\omega)\mathcal{P}_{\mathrm{t}} \times \mathbf{n}, \tag{2.18}$$

where ∇_t is the tangential gradient over S and ϵ' is the so-called "selvedge" region permittivity. The selvedge region is an auxiliary region introduced between the domains V_1 and V_2. In the original derivation of the interface conditions by Heinz in Ref. 49, the fields are evaluated in this domain, and a limit of zero thickness it determined. However, one may question the meaningfulness of a macroscopic quantity ϵ' in a vanishingly thin layer. Thus, in line with the previous discussion, the value of ϵ' may be chosen according to the exact location of the polarization and the choice only affects the value of χ^{s}.

The interface conditions for the flux densities are

$$(\mathbf{D}_1 - \mathbf{D}_2) \cdot \mathbf{n} = -\nabla_t \cdot \mathcal{P}, \tag{2.19}$$

$$(\mathbf{B}_1 - \mathbf{B}_2) \cdot \mathbf{n} = 0. \tag{2.20}$$

However, in a time-harmonic setting, these normal conditions follow from the tangential conditions for fields that satisfy the Maxwell equations in the two domains.

The interface conditions can be used to model surface second-harmonic generation in electromagnetic boundary-value problems. This way, no additional sources exist in any of the domains. We note that due to the surface gradient, a constant normal surface polarization does not yield any SHG. On the other hand, high spatial variations in the

polarization, and thus in the local fields at the fundamental frequency, can generate significant second-harmonic signal. This also makes surface SHG an inherently scale-dependent process: at nanoparticle surfaces, the gradient can yield a factor 0.1/nm, which can compensate for the typical values of χ^{s}, which are on the order of 100 $(\mathrm{nm})^2/\mathrm{V}$.

In general, the surface susceptibility tensor χ^{s} has 27 complex-valued components, but in practice local symmetry in the crystal structure at the surface lowers this number. An important case is local surface isotropy, which occurs for the noble metals gold and silver and is described by the group $C_{\infty\nu}$. In this case, only seven components are non-zero and three of these are independent. The components are[50]

$$\chi^{\mathrm{s}}_{\mathrm{nnn}}, \quad \chi^{\mathrm{s}}_{\mathrm{nss}} = \chi^{\mathrm{s}}_{\mathrm{ntt}}, \quad \chi^{\mathrm{s}}_{\mathrm{sns}} = \chi^{\mathrm{s}}_{\mathrm{tnt}} = \chi^{\mathrm{s}}_{\mathrm{ssn}} = \chi^{\mathrm{s}}_{\mathrm{ttn}}, \tag{2.21}$$

where s and t refer to two orthogonal directions tangential to S. These directions are otherwise arbitrary, thus it's better to write the constitutive relation without direct reference to specific tangent vectors as

$$\mathcal{P}_{\mathrm{n}} = \epsilon_0(\chi^{\mathrm{s}}_{\mathrm{nnn}}(\mathbf{E}(\omega)\cdot\mathbf{n})^2 + \chi^{\mathrm{s}}_{\mathrm{ntt}}\mathbf{E}_{\mathrm{t}}(\omega)\cdot\mathbf{E}_{\mathrm{t}}(\omega)), \tag{2.22}$$

$$\mathcal{P}_{\mathrm{t}} = 2\epsilon_0\chi^{\mathrm{s}}_{\mathrm{ttn}}(\mathbf{E}(\omega)\cdot\mathbf{n})\mathbf{E}_{\mathrm{t}}(\omega). \tag{2.23}$$

Beyond the electric-dipole approximation, SHG may take place in the bulk due to magnetic dipole and electric quadrupole interactions. In this case, the constitutive relations for the second-harmonic fields read[46,51]

$$\mathbf{D} = \epsilon\mathbf{E} - \nabla\cdot\mathbf{Q}, \tag{2.24}$$

$$\mathbf{B} = \mu\mathbf{H} + \mathbf{M}, \tag{2.25}$$

where $\mathbf{Q}$ is the electric quadrupolarization, a rank 2 tensor, and $\mathbf{M}$ is the magnetization. In the undepleted-pump approximation these only act as sources that depend on the known fundamental field. In the case of isotropic homogeneous medium, the bulk response can be described by an effective electric polarization of the form[51]

$$\mathbf{P}(2\omega) = \beta\mathbf{E}(\omega)\nabla\cdot\mathbf{E}(\omega) + \gamma\nabla(\mathbf{E}(\omega)\cdot\mathbf{E}(\omega)) + \delta'(\mathbf{E}(\omega)\cdot\nabla)\mathbf{E}(\omega), \tag{2.26}$$

where β, γ and δ' are scalar constants that depend on the material. The first term vanishes for homogeneous media. It turns out that a bulk source that is a gradient of a scalar function can be equivalently presented by a surface source, which yields the same response outside the nonlinear medium[52]. Thus the γ-term is indistinguishable from the surface response, and we can define an effective surface second-order susceptibility as

$$\chi^{\mathrm{s,eff}}_{\mathrm{nnn}} = \chi^{\mathrm{s}}_{\mathrm{nnn}} + \frac{\gamma\epsilon'}{\epsilon}, \tag{2.27}$$

$$\chi^{\mathrm{s,eff}}_{\mathrm{ntt}} = \chi^{\mathrm{s}}_{\mathrm{ntt}} + \frac{\gamma\epsilon'}{\epsilon}, \tag{2.28}$$

$$\chi^{\mathrm{s,eff}}_{\mathrm{ttn}} = \chi^{\mathrm{s}}_{\mathrm{ttn}}, \tag{2.29}$$

where ϵ is the permittivity of the nonlinear medium. Notice that ϵ' is cancelled in the interface conditions as expected from a bulk source.

In this work, we assume that the γ-term is included in the surface susceptibility tensor χ^{s} without explicit notion of effective quantity. The δ'-term of the bulk response may also be important for some scatterers, but it will not be thoroughly analyzed in this work.

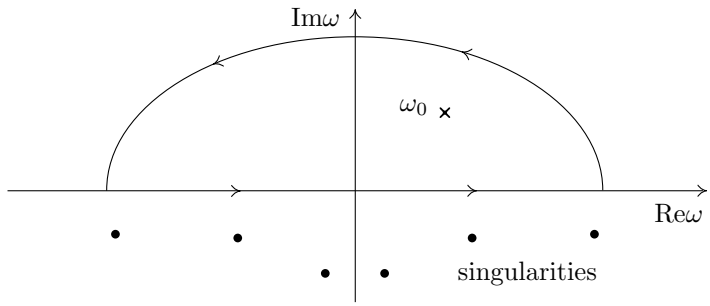

Figure 2.2: Analytic continuation of electric or magnetic susceptibility. Arc tends to infinity.

2.4 Optical response of metals

In the macroscopic electromagnetic formulation, the constitutive relations take into account all aspects of the underlying microscopic light-matter interaction. In the frequency domain, the electric permittivity ϵ and magnetic permeability μ are functions of complex-valued frequency, which are analytic in the upper complex frequency plane. Causality is imposed by requiring that the corresponding susceptibilities $\epsilon/\epsilon_0 - 1$ and $\mu/\mu_0 - 1$ decay at least at the rate $1/|\omega|$ with $|\omega| \to \infty$ in the upper half of $\mathbb{C}$. Thus, they can be analytically continued from the real axis to the upper-half of the complex frequency plane. This is governed by the Cauchy integral formula[53]: for any function $f : U \to \mathbb{C}$ analytic in the open set $U \subset \mathbb{C}$ with boundary ∂U, identity

$$f(z_0) = \frac{1}{2\pi i} \int_{\partial U} \frac{f(z)}{z - z_0} dz, \tag{2.30}$$

holds for $z_0 \in U$. If we set $f = \epsilon/\epsilon_0 - 1$ and U is the upper half-plane, then ∂U reduces to the real axis, where measured data is available. This is illustrated in Fig. 2.2. One may consider the Cauchy integral formula as a boundary integral representation of f over U. From this result, one can also find for ϵ (and μ) a one-to-one correspondence of the real part to imaginary part, results known as the Kramers-Kronig relations. The analytic continuation may appear artificial for such physically intuitive quantities as ϵ and μ, but its importance becomes evident when one seeks the resonance frequencies of a scattering system, as these frequencies are complex valued in general.

In the case of nanoparticles, one may question the validity of interfacing the electromagnetic fields and the microscopic response with the presented type of constitutive relations. For nanoparticles consisting of only a few thousand atoms at most, a full quantum mechanical treatment may be done with, e.g., the density functional theory. In this regime, wave retardation can be neglected and the microscopic response is the essence. However, nanoparticles with linear dimensions on the order of 100 nm consist of millions of atoms, thus radiation and wave retardation become important. Then a continuum electromagnetic model is more practical. However, some nanoparticle systems may have features, whose size is 1 nm or less, yet have a total size of 100 nm. In this case, one may consider macroscopic electromagnetic treatment with nonlocal constititutive relations, that is[54]

$$\mathbf{D}(\mathbf{r}, \omega) = \int_V \epsilon(\mathbf{r} - \mathbf{r}', \omega) \mathbf{E}(\mathbf{r}', \omega) dV', \tag{2.31}$$

where V is the domain with permittivity ϵ, which now depends on two positions: observation and source. This convolution can be performed in the spatial Fourier domain, where the quantities depend on wave-vectors $\mathbf{k}$. A major challenge here is finding a suitable model for the $\mathbf{k}$-dependence of ϵ. For nanoparticles with all linear dimensions above a few nm, the bulk material models seem to work quite well. However, noble metals are an exception in one aspect: the scattering of free electrons from nanoparticle boundaries may increase the damping. For gold, the mean free-path of electrons is roughly 52 nm. Kreibig and Vollmer studied the size dependence of permittivity for small nanoparticles and found that at least for spherical particles, a size correction can be incorporated to a simplified material model[55]. Recently, the incorporation of nonlocal effects in nanoplasmonic models has received increasing interest[56]. It has also been demonstrated that nonlocality can enhance optical nonlinearity in plasmonic metamaterials, which can be used to engineer ultrafast all-optical modulation and switching[57].

The optical response of most materials, especially metals, is practically entirely described by the electric permittivity, while the magnetic permeability is that of vacuum. Physically, one may think that the permittivity is the volume average of a density N of microscopic dipole polarizabilities. To obtain *ab initio* prediction for the permittivity, quantum mechanical treatment may be necessary. In this approach, the Schrödinger equation is solved for the electron wavefunction ψ defined over a crystal unit cell and subject to periodic boundary conditions. The permittivity is then calculated as[23]

$$\epsilon = \epsilon_0(1 + N \langle\psi|\boldsymbol{\mu}|\psi\rangle), \tag{2.32}$$

where $\boldsymbol{\mu}$ is the dipole-moment operator. Of course solving for ψ may prove to be a formidable task and in practice it may be difficult to obtain accurate results. If accurate predictions are required from the macroscopic electromagnetic model and the microscopic response by itself is of no interest, it is practical to consider ϵ as a parameter that can be measured by, for example, ellipsometry.

Sometimes even simplified classical models of the light-matter interaction can yield rather accurate results. Noble metals are a good example of this as the material response at near-infrared frequencies is dominated by the free electrons. The Drude model considers the classical dynamics of non-interacting free electrons, and yields the following result[12]

$$\epsilon(\omega)/\epsilon_0 = \epsilon_\infty - \frac{\omega_p^2}{\omega(\omega + i\gamma)}, \tag{2.33}$$

where ϵ_∞ is the limiting value at infinite frequency, ω_p is the bulk plasmon frequency and γ is the damping constant. This model works surprisingly well for gold and silver around its intended frequency range. For an ideal metal with $\gamma = 0$ and $\epsilon_\infty = 1$, we see that at $\omega = \omega_p$ there is a sharp transition from $\epsilon < 0$ to $\epsilon > 0$ as ω increases. This means that theoretically a bulk metal turns from being a good reflector to a transparent material at the bulk plasmon frequency[§].

Near UV frequencies, the Drude model fails, especially for gold. This is due to the interband transitions from the d band to the conduction band. This response can be qualitatively predicted by the Lorentz model, which considers the dynamics of non-interacting but bound electrons. The binding introduces pole resonances at a set of

[§]For $\epsilon < 0$ the refractive index n is purely imaginary ($n = in_i$ with $n_i \in \mathbb{R}$). The power reflection coefficient for vacuum-metal interface is then $R = |1 - in_i|/|1 + in_i| = 1$.

isolated frequencies ω_n with associated damping factors γ_n and oscillator strengths a_n. The predicted permittivity is [12]

$$\epsilon(\omega)/\epsilon_0 = \epsilon_\infty + \sum_n a_n \frac{\omega_p^2}{\omega_n^2 - \omega^2 - i\gamma_n\omega}. \tag{2.34}$$

A semi-classical treatment yields the same result and links a_n and ω_n to the wavefunction of the quantum model of the material [23].

A benefit of most frequency-domain electromagnetic models is that measured permittivity data can be used directly and there is no need for material models, other than to provide basic understanding of the response. However, the Drude and Lorentz models are important for time-domain electromagnetic models, because calculating the time convolution and evaluating the time-dependent susceptibility based on frequency-domain data is very time consuming. Then it becomes appealing to simultaneously solve the dynamic equations behind the Drude and Lorentz models. More importantly for the present work, these models are also beneficial for solving the complex resonance frequencies of scattering systems in frequency-domain formulations, because the models can be directly evaluated with complex ω without evaluation of the integral (2.30).

In metals, the free electron gas can oscillate coherently and quanta of such oscillations are called plasmons [55]. Plasmons are divided into three cathegories: bulk, surface and particle plasmons. The bulk plasmons are longitudinal oscillations in an infinite bulk medium and the resonance frequency, according to the free-electron model, is $\omega_p = \sqrt{Ne^2/(\epsilon_0 m_e)}$, where N is the electron density, e is the elementary charge and m_e is the electron mass. According to the Drude model, the longitudinal nature of these plasmons prevents their excitation by light. However, including non-local effects arising in the hydrodynamic model predicts that bulk plasmons can be excited by light at frequencies exceeding ω_p. [58]

A plane interface of a noble metal and a dielectric supports solutions to Maxwell's equations that describe charge density oscillations along the material interface. These are called surface plasmons or surface plasmon polaritons [59]. The electric field propagates along the interface and decays exponentially with increasing distance to the interface. Thus the field is highly localized and may lead to significant enhancement of the field amplitude. The dispersion relation for the tangential component of the plasmon wave-vector is [59]

$$k_t^{\mathrm{spp}}(\omega) = \frac{\omega}{c}\sqrt{\frac{\epsilon_1(\omega)\epsilon_2(\omega)}{\epsilon_1(\omega) + \epsilon_2(\omega)}}. \tag{2.35}$$

Light incident from vacuum has a corresponding wave-vector component of magnitude ω/c at most, which is smaller than k_t^{spp}. Thus additional coupling mechanisms, such as a prism or a grating is required to excite a surface plasmon.

For this Thesis, the most relevant class of plasmons are the particle plasmons [3]. These occur in particles, in which the oscillation of electrons is constrained in all directions. These plasmons have isolated resonance frequencies, which depend on the size, shape and material of the particles as well as the surrounding medium. Traditionally, a rigorous definition of particle plasmon modes and the associated resonance frequencies has been done only for simple geometries [3] or in the quasistatic limit [60]. The simplest of all is a sphere, whose diameter is a fraction of the wavelength. The quasistatic solution yields a result that the response is unbounded, when $\epsilon_2(\omega) = -2\epsilon_1$ holds, where ϵ_2 is the permittivity of the particle and ϵ_1 is that of the surrounding medium [12]. Through the

material relation, this defines a resonance frequency. For a small sphere, this frequency is called the Fröhlich frequency. From this result, it is obvious that $\Re(\epsilon_2)$ must be negative, which is characteristic to noble metals. One major goal of this Thesis is to define plasmon modes and associated resonances, without assumption of quasistatics, for particles of smooth but otherwise arbitrary shape.

The values of χ^{s} for noble metals have been measured for gold using thin films and a two-beam setup[50]. A free-electron hydrodynamic model has also been developed to predict the values. In this model, one considers the velocity field $\mathbf{v}$ of an electron fluid acted upon by electric and magnetic fields:

$$m_e N \left(\frac{\partial \mathbf{v}}{\partial t} + (\mathbf{v} \cdot \nabla)\mathbf{v} + \frac{\mathbf{v}}{\tau} \right) = -eN\mathbf{E} - \frac{eN}{c}\mathbf{v} \times \mathbf{B} - \nabla p, \tag{2.36}$$

where N is the electron density, τ the mean damping time and p the pressure due to the Pauli repulsion, which in the Thomas-Fermi theory is related to the number density by $p = \zeta N^{5/3}$ with $\zeta = (3\pi^2)^{2/3}\hbar^2/(5m_e)$. The velocity and number densities are further related to the current and charge densities that appear in the Maxwell equations. The model was originally developed by Rudnick and Stern[61] without damping and later complemented by Sipe with damping included (unpublished work, see Ref. 62). The model predicts relations

$$\chi^{\mathrm{s}}_{\mathrm{nnn}} = \frac{e^3 N_0}{4m_e^2\omega^4} a, \tag{2.37}$$

$$\chi^{\mathrm{s}}_{\mathrm{ttn}} = \frac{e^3 N_0}{2m_e^2\omega^4} b, \tag{2.38}$$

where N_0 is the electron rest density. The factors a and b are

$$a = \frac{4m_e^2\omega^4}{e^3 N_0(\omega_o^2 - \Omega^2)} \left[\left(\frac{\omega^2}{eN_0} + \frac{2\pi e}{m_e} \right) (\chi_F(\omega))^2 - \frac{e}{m_e}\chi_F(\omega)\epsilon_F(\omega) \right], \tag{2.39}$$

$$b = -\frac{2m_e^3\omega^4}{e^5 N_0^2}\chi_F(\Omega) \left[\frac{e}{m_e} - \frac{\omega^2\chi_F(\omega)}{eN_0} \right] \chi_F(\omega), \tag{2.40}$$

where χ_F and ϵ_F are the electric susceptibility and permittivity as predicted by the Drude model, $\Omega = 2\omega$ and ω_o is a potentially frequency dependent parameter that is related to the exact behaviour of the electron density within the selvedge region. The model is not expected to accurately reproduce the frequency dependence of χ^{s}, but may provide qualitative insight.

3 Scattering and diffraction of electromagnetic waves

Scattering of light is a phenomenon that is visible in our everyday life. Lord Rayleigh (John Strutt) discovered already in 1871 that the colors of the clear sky are explained by a theory of scattering of light by small particles and molecules. The awe-inspiring vistas of rainbows and clouds are due to the scattering of light from water droplets, a much more complicated phenomenon. This complication arises largely from the geometry of the scatterers.

This Chapter first introduces a mathematical machinery to precisely define electromagnetic scattering as a BVP. We then derive the quantities to characterize scattering and discuss some of their general properties. The remainder of the Chapter is dedicated to the boundary integral formulation of the scattering problem and concluded by the main result of the Thesis: application of this formulation to model surface SHG.

3.1 Mathematical foundations

In order to formulate an electromagnetic problem, we need to specify a geometrical solution domain. In this work, the domain is divided into subdomains that are selected due to abruptly changing materials. For our purposes, these domains will be subsets of $\mathbb{R}^3$. However, not all subsets are admissible for formulating physical models and thus more constraints are required[§]. We need to be able to integrate and differentiate functions to a certain degree in each subdomain. Next these requirements are made more precise.

A practical starting point for setting constraints to the geometry is the manifold. An n-dimensional manifold is a topological space, which is locally homeomorphic with open subsets of the Euclidean space $\mathbb{R}^n$: it looks locally Euclidean. The homeomorphisms are called charts, and the set of all chosen charts to cover the whole manifold is called an atlas. A manifold is differentiable, if the charts of the atlas are differentiably related (and the topological space is Hausdorff and second-countable). A manifold may have a boundary, in which case the charts map to a half-space of $\mathbb{R}^n$. In this Thesis, the solution domains are differentiable manifolds (or submanifolds) with boundaries as illustrated in Fig. 3.1a. See, e.g., Ref. 63 for detailed definitions.

In this Thesis, the results are mainly presented on manifolds embedded in the Euclidean space $\mathbb{R}^3$ with the Pythagorean metric. Hence submanifolds can be locally described as mappings of the form $f : U \to \mathbb{R}^3$, where $U \subset \mathbb{R}^m$ is an open subset with $m \leq 3$. For

[§]For an example of a subset of $\mathbb{R}^3$ that is clearly not amenable for setting up physically meaningful BVPs see the Banach-Tarski paradox.

electromagnetic problems, mere continuity of these mappings is not sufficient. Consider the domain external to the union of two disks that intersect at a single point as shown in Fig. 3.1b. The mapping f that represents this domain in the neighbourhood of the intersection point is continuous, but it can be shown that the electromagnetic power in a bounded region surrounding this point may be infinite. We need to preclude such situations: Given two sets A and B with metrics d_A and d_B, a function $f : A \to B$ is called Lipschitz continuous, if

$$d_B(f(x), f(y)) \leq K d_A(x, y) \tag{3.1}$$

holds for all $x, y \in A$ and a real constant K.[64] In this work, subdomains locally defined by mappings $f : U \to \mathbb{R}^3$ that satisfy the above criterion with the Pythagorean metrics are called Lipschitz domains. The electromagnetic power in a bounded Lipschitz domain is always finite if the power of the excitation is also finite. However, the fields may exhibit square-integrable singularities, whose degree depends on wedge angles and media[65].

We denote by $\mathbb{L}^2(V)$ a Hilbert space of square-integrable functions $\mathbf{f} : V \to \mathbb{C}^3$ endowed with the inner-product:

$$\langle \mathbf{f}, \mathbf{g} \rangle = \int_V \mathbf{f}^* \cdot \mathbf{g} dV \tag{3.2}$$

for all $\mathbf{f}, \mathbf{g} \in \mathbb{L}^2(V)$. Due to the form of the Maxwell equations, also the curls of the fields are required to be square-integrable over bounded domains. Otherwise, e.g., $\mathbf{E} \in \mathbb{L}^2(V)$ would not imply $\mathbf{B} \in \mathbb{L}^2(V)$. This motivates the definition of the space[66]

$$\mathbb{L}^2(\mathrm{curl}, V) = \{\mathbf{f} \in \mathbb{L}^2(V) | \nabla \times \mathbf{f} \in \mathbb{L}^2(V)\}. \tag{3.3}$$

The norm induced by the $\mathbb{L}^2(\mathrm{curl}, V)$ inner-product applied to the electric and magnetic fields is closely related to the variation of the stored electric and magnetic energies according to the Poynting theorem[46]. However, plane-waves and the resulting scattered waves carry infinite energy and are thus not in $\mathbb{L}^2(\mathrm{curl}, V)$ when V is unbounded. This motivates the definition of a Hilbert space of locally square-integrable functions $\mathbb{L}^2_{\mathrm{loc}}(V)$: A function is in $\mathbb{L}^2_{\mathrm{loc}}(V)$, if it's square-integrable over all bounded subsets of V.[66] A local version of $\mathbb{L}^2(\mathrm{curl}, V)$ is then denoted $\mathbb{L}^2_{\mathrm{loc}}(\mathrm{curl}, V)$.

Consider a Lipschitz domain $V \subset \mathbb{R}^3$ with boundary ∂V oriented so that the unit normal vector $\mathbf{n}$ points into V. For a function $\mathbf{f} : V \to W$ with W an Euclidean vector space, we define the restriction to ∂V by

$$\mathbf{f}|_{\partial V}(\mathbf{r}) = \lim_{\substack{\mathbf{r}' \in V \\ \mathbf{r}' \to \mathbf{r}}} \mathbf{f}(\mathbf{r}'), \ \forall \mathbf{r} \in \partial V. \tag{3.4}$$

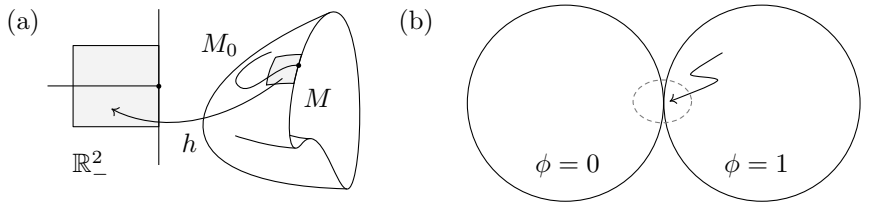

Figure 3.1: (a) Two-dimensional manifold M with boundary and submanifold M_0. A chart $h : M \to \mathbb{R}^2_-$ is illustrated. (b) A continuous domain with non-Lipschitz continuous feature. The two disks are held at different electric potentials ϕ. Electromagnetic power in the dashed domain may be infinite.

The tangential trace and the rotated tangential trace operators are then defined as

$$\gamma_t \mathbf{f} = \mathbf{n} \times \mathbf{f}|_{\partial V} \times \mathbf{n}, \tag{3.5}$$

$$\gamma_r \mathbf{f} = \mathbf{n} \times \mathbf{f}|_{\partial V}. \tag{3.6}$$

The BVPs defined for fields in $\mathbb{L}^2(V)$ and its subspaces impose traces at (subdomains of) ∂V. It is therefore necessary to know the space of the traces of these functions. This turns out to be non-trivial when considering boundary integral representations of electric and magnetic fields: the space $\mathbb{L}^2(\partial V)$ is too large, i.e., not all functions mapped from this space to functions over V are square-integrable[67]. We invoke the standard notion of a fractional order Sobolev space $\mathcal{H}^{-1/2}(\partial V)$ of certain function of the type $\mathbf{f} : \partial V \to \mathbb{C}^3$ (see Refs. 66,67 for the detailed definitions). The spaces of divergence/curl conforming traces are then defined as[67]

$$\mathcal{H}^{-1/2}(\mathrm{div}, \partial V) = \{\mathbf{f} \in \mathcal{H}^{-1/2}(\partial V) | \mathbf{n} \cdot \mathbf{f} = 0, \nabla_t \cdot \mathbf{f} \in \mathcal{H}^{-1/2}(\partial V)\}, \tag{3.7}$$

$$\mathcal{H}^{-1/2}(\mathrm{curl}, \partial V) = \{\mathbf{f} \in \mathcal{H}^{-1/2}(\partial V) | \mathbf{n} \cdot \mathbf{f} = 0, \mathbf{n} \cdot \nabla \times \mathbf{f} \in \mathcal{H}^{-1/2}(\partial V)\}. \tag{3.8}$$

These spaces are $\mathbb{L}^2(\partial V)$ duals to each other, i.e., the elements of $\mathcal{H}^{-1/2}(\mathrm{div}, \partial V)$ are functionals $\langle \mathbf{f}, \cdot \rangle$ with $\mathbf{f} \in \mathcal{H}^{-1/2}(\mathrm{curl}, \partial V)$ and the inner-product is that of $\mathbb{L}^2(\partial V)$.

In the analysis of partial differential equations and in the development of integral operator equivalents of partial differential equations, it is often useful to invoke the concept of distribution. Consider a space $\mathrm{D}(\mathbb{R})$ of test functions $\phi : \mathbb{R} \to \mathbb{R}$, that are infinitely differentiable and have a compact support $[a, b] \subset \mathbb{R}$ with $0 \in [a, b]$. A distribution T is a linear functional over $\mathrm{D}(\mathbb{R})$. It is conventional to write the functional as

$$T(\phi) = \int_a^b t(x)\phi(x)dx, \tag{3.9}$$

and identify t with the distribution, which then appears in expressions as if the distribution was a function, but with the understanding that the equations only hold in the sense that they are multiplied by a test function and integrated.

The delta distribution T_δ is defined as

$$T_\delta(\phi) = \int_a^b \delta(x)\phi(x)dx = \phi(0). \tag{3.10}$$

It is conventional to identify T_δ with δ for brevity.

3.2 Scattering problem and radiation conditions

In the scattering problem, we specify the incident fields $\mathbf{E}_{\mathrm{inc}}, \mathbf{H}_{\mathrm{inc}} \in \mathbb{L}^2_{\mathrm{loc}}(\mathrm{curl}, \mathbb{R}^3)$ that are solutions to Maxwell's equations in a background medium (often vacuum). The task is then to find the electric and magnetic fields that satisfy certain electromagnetic BVP, which is obtained by making a compact perturbation to the medium. In this work, we concentrate on spatially abrupt perturbations. Next we formulate this BVP in detail.

We formulate the time-harmonic electromagnetic scattering problem in the Euclidean space $\mathbb{R}^3$ and decompose the space into Lipschitz continuous domains V_l with $l = 1, 2, \ldots, N_D$ according to the media. We specially identify V_1 as the unbounded "exterior" domain while the other subdomains are compact. The domains are disjoint except for the interfaces

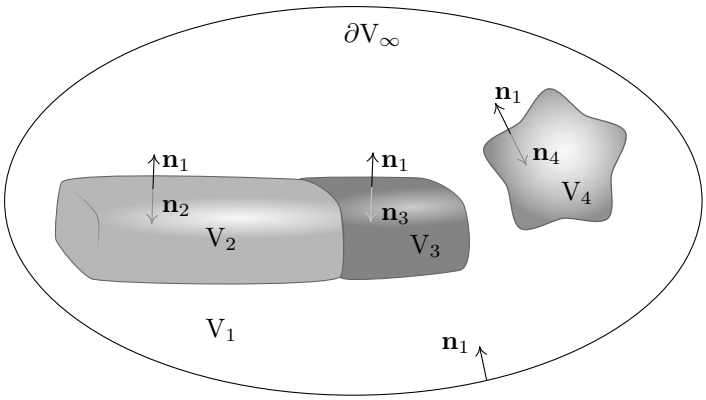

Figure 3.2: Prototype geometry of the scattering problem.

and their union equals $\mathbb{R}^3$. The domain boundaries are denoted ∂V and are oriented so that a normal vector is defined at each point (except in subdomains of zero surface measure). We denote unit-length vectors that point *into* V_l and are normal to ∂V_l by $\mathbf{n}_l$[§]. The boundary of V_1 is the union of a compact part $\partial V_1'$ and a part ∂V_∞ that will be taken to infinity as a limiting process. A prototype geometry is illustrated in Fig. 3.2.

We assume that the material parameters ϵ_l and μ_l are spatially constant within each subdomain. For convenience, we also define the wave numbers $k_l = \omega\sqrt{\epsilon_l \mu_l}$ and wave impedances $\eta_l = \sqrt{\mu_l/\epsilon_l}$. We denote the electric and magnetics fields over the subdomains by $\mathbf{E}_l, \mathbf{H}_l$ and in V_1 we decompose the fields as $\mathbf{E}_1 = \mathbf{E}_\mathrm{s} + \mathbf{E}_\mathrm{inc}$ and $\mathbf{H}_1 = \mathbf{H}_\mathrm{s} + \mathbf{H}_\mathrm{inc}$, where $\mathbf{E}_\mathrm{s}$ and $\mathbf{H}_\mathrm{s}$ are the scattered fields.

From the Maxwell equations and the constitutive relations, we can then derive the following BVP: given the geometry $\{V_i\}$, media $\{(\epsilon_l, \mu_l)\}$, frequency ω and the incident fields $\mathbf{E}_\mathrm{inc}, \mathbf{H}_\mathrm{inc}$, find the scattered fields $\mathbf{E}_\mathrm{s}, \mathbf{H}_\mathrm{s} \in \mathbb{L}^2_\mathrm{loc}(\mathrm{curl}, V_1)$ and the internal fields $\mathbf{E}_l, \mathbf{H}_l \in \mathbb{L}^2(\mathrm{curl}, V_l)$ for $l = 2, 3, \ldots, N_D$ that satisfy

$$\nabla \times \nabla \times \mathbf{E}_l - k_l^2 \mathbf{E}_l = \mathbf{0}, \tag{3.11}$$

$$\nabla \times \nabla \times \mathbf{H}_l - k_l^2 \mathbf{H}_l = \mathbf{0}, \tag{3.12}$$

$$\lim_{|\mathbf{r}|\to\infty} \mathbf{E}_\mathrm{s} \times \mathbf{r} + |\mathbf{r}| \mathbf{H}_\mathrm{s} \eta_1 = \mathbf{0}, \tag{3.13}$$

$$\gamma_{tl'} \mathbf{E}_{l'} = \gamma_{tl''} \mathbf{E}_{l''}, \tag{3.14}$$

$$\gamma_{tl'} \mathbf{H}_{l'} = \gamma_{tl''} \mathbf{H}_{l''}, \tag{3.15}$$

where l' and l'' refer to the two domains sharing the boundary. The definitions of the traces are evidently domain-specific, which is made explicit by the indices. The incident field appears via the interface conditions.

Equation (3.13) is called the Silver-Müller radiation condition, which in 2-D problems is known as the Sommerfeld condition[68]. Physically it can be understood to impose that the

[§]The conventional right-handed orientation of $\mathbb{R}^3$ induces a surface orientation for a subdomain $V \subset \mathbb{R}^3$ so that on ∂V normals point "outwards". However, due to the conventional definition of equivalent surface current densities by "inwards" normal vectors, we choose notation that is more convenient in this aspect.

scattered fields are asymptotically outwards-propagating spherical waves. This condition turns out to be sufficient for the uniqueness of a solution to the scattering problem at real frequencies[66,68].

3.3 Scattering, absorption and extinction cross-sections

The solution to the scattering problem consists of the electric and magnetic fields. The fields themselves are usually impractical for the explanation of various physical phenomena, such as the intensity and directional variation of colors of the Lycurgus cup. Thus we need to define certain figures of merit, which are functionals of the fields.

Consider a surface $S \subset \mathbb{R}^3$ that encloses the scatterer and is oriented so that its normal $\mathbf{n}$ points away from the scatterer. We define a power functional W as

$$W(\mathbf{S}) = \int_S \mathbf{S} \cdot \mathbf{n} dS, \tag{3.16}$$

where $\mathbf{S} = \frac{1}{2}\Re(\mathbf{E}_1 \times \mathbf{H}_1^*)$ is the time-averaged Poynting vector[46]. The functional W quantifies the power into/out of the system enclosed by S. There should appear no confusion regarding the unrelated but similarly denoted Poynting vector $\mathbf{S}$ and surface S. We may decompose $\mathbf{S}$ as $\mathbf{S} = \mathbf{S}_\mathrm{s} + \mathbf{S}_\mathrm{inc} + \mathbf{S}_\mathrm{e}$, where $\mathbf{S}_\mathrm{s} = \frac{1}{2}\Re(\mathbf{E}_\mathrm{s} \times \mathbf{H}_\mathrm{s}^*)$, $\mathbf{S}_\mathrm{inc} = \frac{1}{2}\Re(\mathbf{E}_\mathrm{inc} \times \mathbf{H}_\mathrm{inc}^*)$ and $\mathbf{S}_\mathrm{e} = \frac{1}{2}\Re(\mathbf{E}_\mathrm{inc} \times \mathbf{H}_\mathrm{s}^* + \mathbf{E}_\mathrm{s} \times \mathbf{H}_\mathrm{inc}^*)$. It is also conventional to define a cross-section $\sigma = \pm W / |\mathbf{S}_\mathrm{inc}|$ that has the unit of area. To evaluate $|\mathbf{S}_\mathrm{inc}|$ for plane-waves, the norm $|\cdot|$ can be taken as the $\mathbb{C}^3$ norm as $\mathbf{S}_\mathrm{inc}$ is spatially constant. However, for other incident fields, such as Gaussian beams, the choice of norm is more problematic.

One may then define the absorption cross-section $\sigma_\mathrm{a} = -W(\mathbf{S})/|\mathbf{S}_\mathrm{inc}|$, the scattering cross-section $\sigma_\mathrm{s} = W(\mathbf{S}_\mathrm{s})/|\mathbf{S}_\mathrm{inc}|$ and the extinction cross-section $\sigma_\mathrm{e} = -W(\mathbf{S}_\mathrm{e})/|\mathbf{S}_\mathrm{inc}|$. Physically σ_a and σ_s measure how efficiently a particle absorbs and scatters power, respectively. It turns out that $\sigma_\mathrm{e} = \sigma_\mathrm{s} + \sigma_\mathrm{a}$ holds, i.e., extinction is the sum of absorption and scattering[12].

If the scatterer is lossless, then $\sigma_\mathrm{a} = 0$ holds. For plasmonic nanoparticles, both absoprtion and scattering are usually important, although the former tends to dominate for particles that are small and the latter tends to dominate for particles that are large (with respect to wavelength).

Far away from the scatterer, the scattered fields may be asymptotically written as[12,46]

$$\mathbf{E}_\mathrm{s}(\mathbf{r}) = \mathbf{A}(\hat{\mathbf{r}}) \frac{\exp(ik_1|\mathbf{r}|)}{4\pi|\mathbf{r}|}, \tag{3.17}$$

$$\mathbf{H}_\mathrm{s}(\mathbf{r}) = \hat{\mathbf{r}} \times \mathbf{E}_\mathrm{s}/\eta_1, \tag{3.18}$$

where $\mathbf{A}$ is called the scattering amplitude, also known as the phase function, which only depends on the direction of observation $\hat{\mathbf{r}} = \mathbf{r}/|\mathbf{r}|$, but not on the distance from the scatterer. Note that even if the incident field is linearly polarized, in general $\mathbf{A}$ may be elliptically polarized.

Consider scattering of a plane wave propagating in direction $\mathbf{d}$ with polarization $\mathbf{E}_\mathrm{inc}$. The optical theorem states that the extinction cross-section σ_e is determined by $\Re(\mathbf{A}(\mathbf{d}) \cdot \mathbf{E}_\mathrm{inc})$, i.e., by the forward scattering amplitude[12]. This is peculiar considering that the cross-section was defined as integration of $\mathbf{S}_e$ over all directions. The extinction cross-section has an intuitive interpretation. Consider a detector with "small" aperture A_D far away

from the scatterer. It measures a power $U_D \approx |\mathbf{S}_{\text{inc}}|(A_D - \sigma_{\text{e}})$, where the accuracy of the approximation increases as $A_D \to 0$ for a fixed distance[12]. Thus, loosely speaking, σ_{e} indicates how much power is depleted from the incident wave by the particle that "casts a shadow" over A_D. In practice, σ_{e} may considerably differ from the geometrical shadow of the particle.

The extinction possesses another remarkable property known as the sum-rule. For a spherical particle of radius a, it states that

$$\int_0^\infty \sigma_{\text{e}}(\lambda) d\lambda = 4\pi^3 a^3 \frac{\epsilon_s - 1}{\epsilon_s + 2}, \tag{3.19}$$

holds, where λ is the wavelength and ϵ_s is the permittivity at zero-frequency (static permittivity) of the particle[12]. Thus, even if σ_{e} may vary considerably with λ and a, its integral is always bounded by the volume of the particle and the exact bound depends on the static permittivity. Even though the result is found in closed form for the sphere, there is good reason to believe that the extinction of more complicated particles is similarly limited by the volume and the static permittivity of the particle[12,69].

3.4 Green's function of Helmholtz operator

Green's function of the vectorial Helmholtz operator can be expressed as a dyadic-valued mapping of two arguments: observation point $\mathbf{r}$ and source point $\mathbf{r}'$ and is defined as the response to the delta distribution source:

$$\nabla \times \nabla \times \mathbf{G}(\mathbf{r}, \mathbf{r}') - k^2 \mathbf{G}(\mathbf{r}, \mathbf{r}') = \mathbf{I}\delta(\mathbf{r} - \mathbf{r}'), \ \forall \mathbf{r}, \mathbf{r}' \in \mathbb{R}^3, \tag{3.20}$$

which is required to hold in the distributional sense and where $\mathbf{I}$ is the unit dyadic. In the case of free space, where k is a constant in $\mathbf{r}$, the solution is

$$\mathbf{G}(\mathbf{r}, \mathbf{r}') = \left(\mathbf{I} + \frac{1}{k^2}\nabla\nabla\right) G(\mathbf{r}, \mathbf{r}'), \tag{3.21}$$

where G is the scalar Green's function defined as $G(\mathbf{r}, \mathbf{r}') = \exp(ikR)/(4\pi R)$ with $R = |\mathbf{r} - \mathbf{r}'|$. For a point dipole at position $\mathbf{r}_d$ with dipole moment $\mathbf{p} \in \mathbb{C}^3$, the electric field at $\mathbf{r}$ is simply $\mathbf{E}(\mathbf{r}) = \omega^2 \mu \mathbf{G}(\mathbf{r}, \mathbf{r}_d) \cdot \mathbf{p}$.

In addition to scattering from single particles, scattering from regular arrays of particles is often of interest in nanoplasmonics and other branches of optics. In this case, scattering is

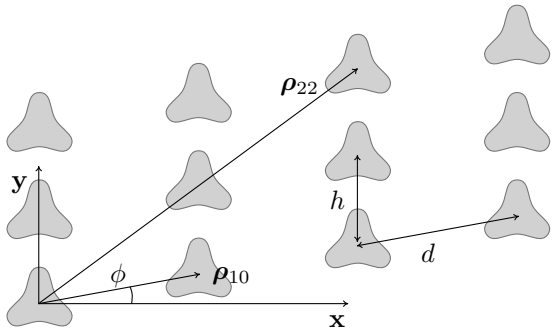

Figure 3.3: Array of scatterers.

often referred to as diffraction, although generally the two terms may be used synonymously. We focus on a geometry that is periodic in a plane with lattice constants d and h and lattice skew angle ϕ as illustrated in Fig. 3.3. We define the lattice translation vectors $\boldsymbol{\rho}_{nm}$ by

$$\boldsymbol{\rho}_{nm} = nd\cos\phi\mathbf{x} + (mh + nd\sin\phi)\mathbf{y} \qquad \text{for } n, m \in \mathbb{Z} \tag{3.22}$$

and the "unit cell" U

$$U = \{(ud\cos\phi, (vh + ud\sin\phi), z) \in \mathbb{R}^3 | u, v \in [0,1], z \in \mathbb{R}\}, \tag{3.23}$$

which is compact in planes z = constant. We denote the unit cell area in such planes by $A = dh\cos\phi$. The periodic solution domain $\mathbb{R}^3$ and its subdomains are regenerated by $\mathbf{r} + \boldsymbol{\rho}_{nm}$, where $\mathbf{r} \in U$. For excitation by an incident plane wave with wave vector $\mathbf{k}_0$, the solution is pseudo-periodic as [70]

$$\mathbf{E}(\mathbf{r} + \boldsymbol{\rho}_{nm}) = \mathbf{E}(\mathbf{r})e^{i\mathbf{k}_0\cdot\boldsymbol{\rho}_{nm}}, \tag{3.24}$$

$$\mathbf{H}(\mathbf{r} + \boldsymbol{\rho}_{nm}) = \mathbf{H}(\mathbf{r})e^{i\mathbf{k}_0\cdot\boldsymbol{\rho}_{nm}}, \tag{3.25}$$

for all $\mathbf{r}$ and $n, m \in \mathbb{Z}$. For points $\mathbf{r}$ on the boundary of the unit cell, this sets constraints to the solution, known as the Bloch boundary conditions. The scattering by point sources is described by the periodic scalar Green's function [70]

$$G_p(\mathbf{r}, \mathbf{r}') = \frac{1}{4\pi}\sum_{n=-\infty}^{\infty}\sum_{m=-\infty}^{\infty}\frac{e^{ikR_{nm}}}{R_{nm}}e^{i\mathbf{k}_0\cdot\boldsymbol{\rho}_{nm}}, \tag{3.26}$$

where $R_{nm} = |\mathbf{r} - \mathbf{r}' - \boldsymbol{\rho}_{nm}|$ holds.

The convergence of this series (3.26) is asymptotically $O(1/\min(n,m))$, which is considered very slow. Several series acceleration techniques have been developed to mitigate the problem, including the spectral series [71], the Kummer transformation [72,73], the lattice sums method [74,75], integral identity based quadrature methods [76] and the Ewald method [77–84]. Combination of several methods was considered in Ref. 85 and a review is presented in Ref. 86.

The Ewald method is the most prominent all-around approach at present. It's based on the integral representation of the spherical wave [77,78,87]

$$\frac{e^{ikR}}{R} = \frac{2}{\sqrt{\pi}}\int_0^\infty e^{-R^2s^2 + \frac{k^2}{4s^2}}\,ds, \tag{3.27}$$

which exists as a Riemann integral only along a carefully chosen path in the complex s-plane. Due to the asymptotic behaviour of the integrand with respect to R, the integration is split into two parts at $E \in (0, \infty)$, the splitting parameter. The integration along $[0, E]$ is further Poisson transformed into a spectral series. Consequently, the Green function can be written as the sum of "spatial" and "spectral" terms as $G_p = G_p^{\text{spat}} + G_p^{\text{spec}}$, where [86]

$$G_p^{\text{spat}}(X,Y,Z) = \frac{1}{8\pi}\sum_{n=-\infty}^{\infty}\sum_{m=-\infty}^{\infty}\frac{e^{i\mathbf{k}_0\cdot\boldsymbol{\rho}_{nm}}}{R_{nm}}\sum_{\pm}e^{\pm ikR_{nm}}\operatorname{erfc}\left(R_{nm}E \pm \frac{ik}{2E}\right), \tag{3.28}$$

$$G_p^{\text{spec}}(X,Y,Z) = \frac{1}{4A}\sum_{n=-\infty}^{\infty}\sum_{m=-\infty}^{\infty}\frac{e^{i\mathbf{k}_t\cdot\mathbf{R}}}{-ik_z}\sum_{\pm}e^{\mp ik_zZ}\operatorname{erfc}\left(\frac{-ik_z}{2E} \pm ZE\right), \tag{3.29}$$

where $X = x - x'$, $Y = y - y'$, $Z = z - z'$ and erfc is the complementary error function. The series in Eqs. (3.28) and (3.29) exhibit Gaussian convergence. The wave vector components can be written as

$$\mathbf{k}_t = \left(k_{0x} + 2\pi \left(\frac{n}{d\cos\phi} - \frac{m\sin\phi}{h\cos\phi} \right) \right) \mathbf{x} + \left(k_{0y} + 2\pi \frac{m}{h} \right) \mathbf{y}, \tag{3.30}$$

$$k_z = \sqrt{k^2 - \mathbf{k}_t \cdot \mathbf{k}_t}. \tag{3.31}$$

Positive branch of the square root is chosen to impose decaying of the erfc. Note that in Ref. 86 the opposite time convention $\exp(i\omega t)$ is utilized, but the results here are adopted to the convention of this Thesis.

Challenges for the Ewald method are the efficient evaluation of erfc [88], the optimal choice of E [89] and the truncation of the series [90]. Especially for $\lambda > \max(d, h)$, the following splitting parameter has been found optimal in the sense that the difference in the number of terms in the two series, required for given error tolerance, is minimal [86]:

$$E_{\text{opt}} = \sqrt{\frac{\pi}{dh\cos\phi}}. \tag{3.32}$$

For most integral operator methods, it is necessary to evaluate the gradient of G_p, which is given in the appendix. In the Ewald method, the gradient retains the Gaussian convergence.

In addition to the free space and periodic media, the case of stratified media is of practical interest and requires its special Green's function [91]. In this case k is a function of a spatial variable, say coordinate z. Because at material interfaces, reflection and refraction are polarization dependent, it is clear that not only the scalar part G needs to be modified from the free-space form. The free-space (wave number k_1) Green dyadic has a plane-wave representation [2]:

$$\mathbf{G}(\mathbf{r}, \mathbf{r}') = \frac{i}{8\pi^2} \int_{-\infty}^{\infty} \int_{-\infty}^{\infty} \mathbf{M} e^{i(k_x(x-x') + k_y(y-y') + k_{z_1}|z-z'|)} dk_x dk_y, \tag{3.33}$$

where the dyadic $\mathbf{M}$ depends on k_1, k_x, k_y. The lateral wave vector components k_x, k_y are continuous across layer interfaces, while $k_{z_n} = (k_n^2 - k_x^2 - k_y^2)^{1/2}$ holds for layer n. This dyadic can be decomposed into form $\mathbf{M} = \mathbf{M}_{\text{s}} + \mathbf{M}_{\text{p}}$ according to s- and p-polarizations. For each plane-wave, one merely applies the Fresnel coefficients to arrive at Green's dyadics for each layer. By transforming to the spectral cylindrical coordinates, the results can be expressed as various integrals of the Sommerfeld type [91,92]:

$$\int_0^{\infty} \xi(k_\rho, k_{zl}) \frac{k_\rho^p}{k_{zl}^q} e^{ik_{zl}(z \pm z')} J_n(k_\rho \rho) dk_\rho, \tag{3.34}$$

where ξ is the generalized reflection coefficient, J_n is the Bessel function of first kind and order n=0,1 and p=0,1,2 and q=0,1. The integrand may have various poles and branch-cuts in the upper-half of the complex k_ρ-plane, related to surface waves and radiative continua. These singularities can be avoided by splitting the integration at some $k_{\rho 0} \in \mathbb{R}$ and deforming the part $0 < k_\rho < k_{\rho 0}$ to the lower-half of the complex plane [92]. The remaining part can be continued along the real axis or along the imaginary axis (the Hankel transform). This latter integration is called the Sommerfeld tail. Many approaches have been developed for efficient computation of this tail, but the $\nabla\nabla$ operator of the spatial form leads to rather high values of p in (3.34), making the integrand slowly decaying for small $|z \pm z'|$ or small ρ. An efficient and practical evaluation of the Green dyadic and the Sommerfeld tails is an ongoing research topic [91–104].

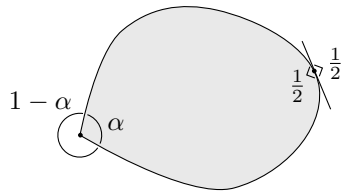

Figure 3.4: Relative solid angle at non-smooth and smooth boundary points.

3.5 Stratton-Chu equations

Consider a Lipschitz continuous domain V with boundary ∂V oriented such that the normal $\mathbf{n}$ points into V. For the time-harmonic electric and magnetic fields in this domain, there exists the following boundary representation [105]:

$$\begin{aligned}\alpha\mathbf{E}(\mathbf{r}) = &\int_V i\omega\mu G(\mathbf{r},\mathbf{r}')\mathbf{J}(\mathbf{r}') + \nabla' G(\mathbf{r},\mathbf{r}')\times\mathbf{M}(\mathbf{r}') + \nabla' G(\mathbf{r},\mathbf{r}')\frac{\rho(\mathbf{r}')}{\epsilon}dV' \\ &+ \int_{\partial V} i\omega\mu G(\mathbf{r},\mathbf{r}')\gamma_r\mathbf{H}(\mathbf{r}') - \nabla' G(\mathbf{r},\mathbf{r}')\times\gamma_r\mathbf{E}(\mathbf{r}') + \nabla' G(\mathbf{r},\mathbf{r}')\mathbf{n}\cdot\mathbf{E}(\mathbf{r}')dS'\end{aligned} \tag{3.35}$$

$$\begin{aligned}\alpha\mathbf{H}(\mathbf{r}) = &\int_V i\omega\epsilon G(\mathbf{r},\mathbf{r}')\mathbf{M}(\mathbf{r}') - \nabla' G(\mathbf{r},\mathbf{r}')\times\mathbf{J}(\mathbf{r}') + \nabla' G(\mathbf{r},\mathbf{r}')\frac{\rho_m(\mathbf{r}')}{\mu}dV' \\ &- \int_{\partial V} i\omega\epsilon G(\mathbf{r},\mathbf{r}')\gamma_r\mathbf{E}(\mathbf{r}') + \nabla' G(\mathbf{r},\mathbf{r}')\times\gamma_r\mathbf{H}(\mathbf{r}') - \nabla' G(\mathbf{r},\mathbf{r}')\mathbf{n}\cdot\mathbf{H}(\mathbf{r}')dS',\end{aligned} \tag{3.36}$$

for all $\mathbf{r}\in V$. In our notation $\nabla' G$ denotes the function that is the gradient of G with respect to the second argument. The quantity α is one if $\mathbf{r}\in V-\partial V$, zero if $\mathbf{r}\notin V\cup\partial V$. If $\mathbf{r}\in\partial V$, then α is the relative solid angle subtended by the boundary at this position. The relative solid angles of smooth and non-smooth boundary points are illustrated in Fig. 3.4. All the integrations are defined in the Cauchy principal value sense. Equations (3.35) and (3.36) are called the Stratton-Chu equations [105,106].

The case $\alpha = 0$ follows from the so-called jump conditions: as $\mathbf{r}$ passes from V to its complement in $\mathbb{R}^3$, the kernel singularities yield factors that exactly cancel the left hand side of Eqs. (3.35) and (3.36). This is called the extinction theorem[§]. Note that this does not mean that the fields are zero in this complement region.

We define the following boundary integral operators

$$(\mathscr{D}\mathbf{f})(\mathbf{r}) = i\omega\mu\int_{\partial V} G(\mathbf{r},\mathbf{r}')\mathbf{f}(\mathbf{r}')dS' - \frac{1}{i\omega\epsilon}\nabla\int_{\partial V} G(\mathbf{r},\mathbf{r}')\nabla'_t\cdot\mathbf{f}(\mathbf{r}')dS', \tag{3.37}$$

$$(\mathscr{K}\mathbf{f})(\mathbf{r}) = \int_{\partial V}\nabla' G(\mathbf{r},\mathbf{r}')\times\mathbf{f}(\mathbf{r}')dS'. \tag{3.38}$$

The following mapping properties have been established [67,107]:

$$\gamma_r\mathscr{D} : \mathcal{H}^{-1/2}(\mathrm{div},\partial V)\to\mathcal{H}^{-1/2}(\mathrm{div},\partial V), \tag{3.39}$$

$$\gamma_t\mathscr{D} : \mathcal{H}^{-1/2}(\mathrm{div},\partial V)\to\mathcal{H}^{-1/2}(\mathrm{curl},\partial V) \tag{3.40}$$

$$\gamma_r(\mathscr{K}+\tfrac{1}{2}\mathscr{I}) : \mathcal{H}^{-1/2}(\mathrm{div},\partial V)\to\mathcal{H}^{-1/2}(\mathrm{div},\partial V), \tag{3.41}$$

$$\gamma_t(\mathscr{K}+\tfrac{1}{2}\mathscr{I}) : \mathcal{H}^{-1/2}(\mathrm{div},\partial V)\to\mathcal{H}^{-1/2}(\mathrm{curl},\partial V), \tag{3.42}$$

[§]The extinction theorem should not be confused with the previously discussed extinction cross-section.

where $\mathscr{I}$ is the identity operator.

It is conventional to define the equivalent surface current densities

$$\mathbf{J}^{\mathrm{s}} = \gamma_r \mathbf{H}, \tag{3.43}$$

$$\mathbf{M}^{\mathrm{s}} = -\gamma_r \mathbf{E}. \tag{3.44}$$

In a current-free domain, the Stratton-Chu equations are then concisely written as

$$\alpha \mathbf{E} = \mathscr{D}\mathbf{J}^{\mathrm{s}} + \mathscr{K}\mathbf{M}^{\mathrm{s}}, \tag{3.45}$$

$$\alpha \mathbf{H} = \mathscr{D}\mathbf{M}^{\mathrm{s}}/\eta^2 - \mathscr{K}\mathbf{J}^{\mathrm{s}}. \tag{3.46}$$

In the far-field, the scattering amplitude, defined in Eq. (3.17), due to $\mathbf{J}^{\mathrm{s}}$ and $\mathbf{M}^{\mathrm{s}}$ follows from the Stratton-Chu equations as

$$\mathbf{A}(\hat{\mathbf{r}}) = -\hat{\mathbf{r}} \times \hat{\mathbf{r}} \times i\omega\mu \int_{\partial V} e^{-ik\hat{\mathbf{r}}\cdot\mathbf{r}'} \mathbf{J}^{\mathrm{s}}(\mathbf{r}')dS' - ik\hat{\mathbf{r}} \times \int_{\partial V} e^{-ik\hat{\mathbf{r}}\cdot\mathbf{r}'} \mathbf{M}^{\mathrm{s}}(\mathbf{r}')dS', \tag{3.47}$$

where the integrals are Fourier transforms of the equivalent surface current density distributions.

For periodic structures, the spectral representation of G_p is exponentially convergent for $\mathbf{r}$ far away from the source plane:

$$G_p(\mathbf{r}, \mathbf{r}') = \frac{1}{2A} \sum_{n=-\infty}^{\infty} \sum_{m=-\infty}^{\infty} \frac{e^{ik_z|z-z'|}}{k_z} e^{i\mathbf{k}_t\cdot(\mathbf{r}-\mathbf{r}')}, \tag{3.48}$$

where $\mathbf{k}_t$ and k_z depend on n and m even though this is not explicitly written. By substituting Eq. (3.48) to Eqs. (3.45) and (3.46), we see that the response is given in terms of plane-waves, whose amplitudes result from integration over the boundary of the scatterer. It can be seen that at $k_z = 0$ the Green function has a simple pole with respect to ω, independent of the scattering object. This is the so-called Wood anomaly, where the response of the periodic array vanishes[108]. It is noteworthy that even though in Eq. (3.48) a summation over propagating waves (those with real k_z) is required for the far-field, in practice the summation is incorrect. This is because in reality a beam of finite cross-section is used to illuminate the array. Thus the terms of the series actually represent beams of finite cross-section, which become spatially separated in the far-field. Each individual term is referred to as diffraction order and in calculations, these orders are separately the quantities of interest.

3.6 Boundary integral operator formulations of scattering problems

By the use of the representations (3.35) and (3.36), the scattering problem can be formulated in terms of $\mathbf{J}^{\mathrm{s}}$ and $\mathbf{M}^{\mathrm{s}}$ over the boundary of the scatterer. However, there are many ways to combine the boundary integral equations and the unknowns to obtain problem definitions, which yield the unique solution to the scattering problem in certain frequency ranges.

The different boundary integral formulations can be categorized at the highest level into direct and indirect methods[109]. The direct methods are based on the Stratton-Chu

representations for the fields and in this case, there appear seemingly more equations than unknowns (the equivalent surface current densities)[§]. The indirect methods are based on the observation that any function $\mathbf{f} \in \mathcal{H}^{-1/2}(\mathrm{div}, \partial V)$ is mapped by $\mathscr{D}$ or $\mathscr{K}$ to a function over V that satisfies the Helmholtz equation and the radiation condition. In this case, there are more unknowns than equations, and the unknowns are combined in a judicious manner to construct a well-defined problem.

The direct methods can be classified according to the way the Stratton-Chu equations in the different domains are combined. These formulations include the electric field integral equation (EFIE)[109], magnetic field integral equation (MFIE)[109], combined field integral equation (CFIE)[109], Poggio-Miller-Chang-Harrington-Wu-Tsai (PMCHWT)[18,110–112] and Müller[113,114] formulations. In each formulation, different traces of the equations can be considered, which gives rise to, e.g., N-EFIE (γ_r trace) and T-EFIE (γ_t trace) formulations[115]. Other formulations also exist and have been studied[116,117]. A somewhat different formulation is the null-field method[118], which is based on the extinction theorem. In this method, the equations are usually enforced in an approximate manner on a spherical shell enclosing the scatterer, whence the vector spherical wavefunctions can be utilized. This approach works well only for smooth particles not very different from the sphere, but the integral kernels are non-singular.

The PMCHWT formulation with proper discretization has been found accurate for the modeling of the optical properties of plasmonic structures[40,119]. Thus we will concentrate on this formulation. In the scattering problem defined in Section 3.2, we associate each domain $l = 1, 2, \ldots, N_D$ with the unknowns $\mathbf{J}^{\mathrm{s}}_l$ and $\mathbf{M}^{\mathrm{s}}_l$ and operators $\mathscr{D}_l$ and $\mathscr{K}_l$, where it is understood that the index refers to the domain boundary ∂V_l, material parameters and Green's function.

The domain V_1 requires some special care. In this case, the boundary of the infinite exterior domain is the union of a compact part $\partial V_1'$ and a boundary at infinity, denoted by ∂V_∞. In Eqs. (3.45) and (3.46), the integration over ∂V_∞ can be divided into two parts: one due to the scattered fields and another due to the incident fields. The former conveniently vanishes due to the radiation condition[¶], i.e., Eq. (3.13) and the latter just produces the incident fields. Thus in domain V_1, we get

$$\alpha \mathbf{E}_1 = \mathbf{E}_{\mathrm{inc}} + \mathscr{D}_1 \mathbf{J}^{\mathrm{s}}_1 + \mathscr{K}_1 \mathbf{M}^{\mathrm{s}}_1, \tag{3.49}$$

$$\alpha \mathbf{H}_1 = \mathbf{H}_{\mathrm{inc}} + \mathscr{D}_1 \mathbf{M}^{\mathrm{s}}_1/\eta_1^2 - \mathscr{K}_1 \mathbf{J}^{\mathrm{s}}_1, \tag{3.50}$$

where it is understood that the integrations are over $\partial V_1'$. At this point we have two boundary integral equations and two unknown equivalent surface current densities in each domain. The fields automatically satisfy the Helmholtz equations and the produced scattered fields satisfy the radiation condition. We still need to impose the interface conditions. This is done by requiring:

$$\mathbf{J}^{\mathrm{s}}_{l'} + \mathbf{J}^{\mathrm{s}}_{l''} = \mathbf{0}, \tag{3.51}$$

$$\mathbf{M}^{\mathrm{s}}_{l'} + \mathbf{M}^{\mathrm{s}}_{l''} = \mathbf{0} \tag{3.52}$$

with the same index convention as in Section 3.2. In the simplest case of a single scatterer, we would only need to solve for, e.g., $\mathbf{J}^{\mathrm{s}}_1$ and $\mathbf{M}^{\mathrm{s}}_1$. Thus we end up with two boundary

[§]As we are dealing with infinite dimensional Hilbert spaces, the expression "more equations than unknowns" is not precise, but it has well-defined implications to the approximate solution via the method of moments.

[¶]This can actually be seen as the reason for the very definition of the Silver-Müller condition.

integral equations but only one unknown per domain. In the T-PMCHWT formulation, the equations sharing the same boundary are added together to reduce the number of equations:

$$\sum_l \delta_{l1}\gamma_t \mathbf{E}_{\text{inc}} + \gamma_{tl}\mathscr{D}_l \mathbf{J}_l^{\text{s}} + \gamma_{tl}\mathscr{K}_1 \mathbf{M}_l^{\text{s}} - \alpha\gamma_{rl}\mathbf{M}_l^{\text{s}} = \mathbf{0}, \tag{3.53}$$

$$\sum_l \delta_{l1}\gamma_t \mathbf{H}_{\text{inc}} + \gamma_{tl}\mathscr{D}_l \mathbf{M}_l^{\text{s}}/\eta_l^2 - \gamma_{tl}\mathscr{K}_l \mathbf{J}_l^{\text{s}} + \alpha\gamma_{rl}\mathbf{J}_l^{\text{s}} = \mathbf{0}, \tag{3.54}$$

where we used $\gamma_t \mathbf{E} = \gamma_r \mathbf{M}^{\text{s}}$ and $\gamma_t \mathbf{H} = -\gamma_r \mathbf{J}^{\text{s}}$. For Lipschitz domains, it is possible that α takes different values on opposite sides of a surface as illustrated in Fig. 3.4. However, this may only happen over zero- or one-dimensional submanifolds of the surface. Then again, the weak forms of the equations are obtained by surface integration, hence integration over such submanifolds vanishes due to zero surface measure. Thus upon summation in Eqs. (3.53) and (3.54), the terms involving α will cancel due to the interface conditions. For a single scatterer, the equations are then

$$\gamma_{t1}\mathbf{E}_{\text{inc}} + \gamma_{t1}\mathscr{D}_1 \mathbf{J}^{\text{s}} + \gamma_{t1}\mathscr{K}_1 \mathbf{M}^{\text{s}} + \gamma_{t2}\mathscr{D}_2 \mathbf{J}^{\text{s}} + \gamma_{t2}\mathscr{K}_2 \mathbf{M}^{\text{s}} = \mathbf{0}, \tag{3.55}$$

$$\gamma_{t1}\mathbf{H}_{\text{inc}} + \gamma_{t1}\mathscr{D}_1 \mathbf{M}^{\text{s}}/\eta_1^2 - \gamma_{t1}\mathscr{K}_1 \mathbf{J}^{\text{s}} + \gamma_{t2}\mathscr{D}_2 \mathbf{M}^{\text{s}}/\eta_2^2 - \gamma_{t2}\mathscr{K}_2 \mathbf{J}^{\text{s}} = \mathbf{0}. \tag{3.56}$$

The PMCHWT formulation has a unique solution for all nonzero frequencies, but has no zero-frequency limit. This has some implications for the method of moments approximate solution scheme to be described in Section 5.2.

3.7 Second-harmonic scattering

We will now formulate the surface second-harmonic scattering problem in the undepleted-pump approximation by the boundary integral operators. We assume that the fundamental fields have been solved by the method outlined in the previous section and from the solution we can conveniently calculate the surface polarization $\mathcal{P}$. In this section, it is understood that all quantities correspond to the second-harmonic frequency. In this case, the α-terms in Eqs. (3.53) and (3.54) do not cancel, because the equivalent surface current densities suffer a discontinuity due to the surface polarization $\mathcal{P}$. Thus the equations become

$$\sum_l \gamma_{tl}\mathscr{D}_l \mathbf{J}_l^{\text{s}} + \gamma_{tl}\mathscr{K}_1 \mathbf{M}_l^{\text{s}} + \alpha\frac{1}{\epsilon'}\nabla_t \mathcal{P}_{\text{n}}^l = \mathbf{0}, \tag{3.57}$$

$$\sum_l \gamma_{tl}\mathscr{D}_l \mathbf{M}_l^{\text{s}}/\eta_l^2 - \gamma_{tl}\mathscr{K}_l \mathbf{J}_l^{\text{s}} - i\omega\alpha\gamma_{rl}\mathcal{P}_{\text{t}}^l = \mathbf{0}, \tag{3.58}$$

and the equivalent surface current densities are connected by

$$\mathbf{M}_{l'}^{\text{s}} + \mathbf{M}_{l''}^{\text{s}} = -\frac{1}{\epsilon'_{l''}}\gamma_{rl'}\nabla_t \mathcal{P}_{\text{n}}^{l'} - \frac{1}{\epsilon'_{l'}}\gamma_{rl''}\nabla_t \mathcal{P}_{\text{n}}^{l''}, \tag{3.59}$$

$$\mathbf{J}_{l'}^{\text{s}} + \mathbf{J}_{l''}^{\text{s}} = -i\omega\gamma_{tl'}\mathcal{P}_t^{l'} - i\omega\gamma_{tl''}\mathcal{P}_t^{l''}. \tag{3.60}$$

There are several strategies to manipulate these equations when preparing to seek approximate solutions. In the first work by the author, two current densities were sought for each domain and Eqs. (3.59) and (3.60) were imposed explicitly. In a later work, a more efficient, but still accurate, approach was to use these equations to substitute half of the unknowns in Eqs. (3.57) and (3.58). Thus the same complexity is achieved as in the linear scattering problem.

4 Eigenmodes and resonances of scatterers

Many physical systems exhibit resonant behaviour, where a weak excitation leads to an enormous response. For example, a string fixed at both ends vibrates resonantly at frequencies that are integer multiples of $\sqrt{T/\mu}/(2L)$, where T is the tension, μ is the linear density and L is the length of the string. These frequencies can be associated with eigenmodes, which are eigenfunctions of the pertinent differential operator. The knowledge of these modes gives a very good idea of the possible outcomes when using a specific excitation.

It is clear from observations that certain scatterers also exhibit resonant behaviour. It has been found that electromagnetic pulse (EMP) excitation of aircraft and missiles produces damped sinusoidal currents over the material bodies. The extinction spectrum of monodisperse water droplets displays a ripple structure with very sharp spectral peaks. The colors of liquid suspensions of gold and silver nanoparticles show a vivid dependence on the nanoparticle shape and size. This Chapter analyses the mathematical properties of a certain boundary integral formulation of the scattering problem to define resonances and modes of scatterers, which are useful in explaining such observations.

4.1 Spectral theory

In Section 3.1 we presented the appropriate Hilbert spaces for the electric and magnetic fields and their boundary traces. Next we invoke a few mandatory definitions and results from Refs. 120,121 for the analysis of scattering resonances.

A *metric space* A is a set equipped with a *metric* $d : A \times A \to \mathbb{R}$ that measures the distance between the elements of A. Let X and Y be subsets of a metric space A such that $X \subset Y$. The set X is called *dense* in Y, if $\forall y \in Y$ and $\forall \epsilon > 0$ there is $x \in X$ such that $d(x, y) < \epsilon$.

A *norm space* is a linear space with the notion of a *norm* $|\cdot|$. A *Banach space* is a complete norm space. An operator $\mathscr{L} : A \to B$ mapping between norm spaces A and B is *bounded*, if there exists a positive real number K such that

$$|\mathscr{L}x|_B < K\,|x|_A \qquad \forall x \in A. \tag{4.1}$$

A bounded operator $\mathscr{L} : A \to B$ is *compact*, if for each bounded sequence $\{x_n\} \subset A$ there is a subsequence $\{x_{n_m}\}$ such that $\{\mathscr{L}x_{n_m}\}$ converges in B.[120] All matrix operators are compact, but, e.g., the identity operator in infinite-dimensional norm spaces is not. For the better understanding of compact operators, the following result is useful: Let $\mathscr{L} : A \to B$

be a compact linear operator. For any positive real ϵ, there exists a finite-dimensional subspace M of the image[§] of $\mathscr{L}$, such that

$$\inf_{y\in M} |\mathscr{L}x - y|_B \leq \epsilon\,|x|_A \tag{4.2}$$

for $x \in A$.[120] Thus the image of $\mathscr{L}$ is approximated by a finite-dimensional space to an arbitrary precision ϵ.

For a bounded linear operator over Hilbert spaces $\mathscr{L} : A \to B$ there exists a unique operator $\mathscr{L}^\dagger : B \to A$, called the *adjoint*, which satisfies

$$\langle \mathscr{L}x, y\rangle_B = \langle x, \mathscr{L}^\dagger y\rangle_A \tag{4.3}$$

for all $x \in A$ and $y \in B$.[121] Operator $\mathscr{L}$ is called self-adjoint, if $\mathscr{L} = \mathscr{L}^\dagger$ holds. Such operators form a particularly well-studied class of operators over Hilbert spaces.

For a square matrix operator A, the eigenvalues λ are defined by the characteristic polynomial $\det(\mathrm{A} - I\lambda) = 0$. For linear operators in infinite-dimensional Hilbert spaces, the determinant is not defined. For this reason, one defines for a linear operator $\mathscr{L} : A \to A$ over Hilbert space A and a complex number λ the *resolvent operator* $\mathscr{R}_\lambda(\mathscr{L}) = (\mathscr{L} - \lambda\mathscr{I})^{-1}$. The values λ are classified according to the properties of the resolvent[120]:

1. $\mathscr{R}_\lambda(\mathscr{L})$ does not exist for λ. These λ constitute the *point spectrum* $\sigma_p(\mathscr{L})$ and are the familiar eigenvalues.
2. $\mathscr{R}_\lambda(\mathscr{L})$ exists for λ:
   a) The image of $\mathscr{L} - \lambda\mathscr{I}$ is dense in A:
      i. $\mathscr{R}_\lambda(\mathscr{L})$ is bounded. Then λ is called a regular value. These values constitute the resolvent set $\rho(\mathscr{L})$.
      ii. $\mathscr{R}_\lambda(\mathscr{L})$ is unbounded (not continuous). These values λ constitute the *continuous spectrum* $\sigma_c(\mathscr{L})$.
   b) Closure of the image of $\mathscr{L} - \lambda\mathscr{I}$ is a proper (the sets are not equal) subset of A. These values constitute the *residual spectrum* $\sigma_r(\mathscr{L})$.

The total spectrum $\sigma(\mathscr{L})$ is the complement of the resolvent set $\sigma(\mathscr{L}) = \mathbb{C} - \rho(\mathscr{L})$ and it can be shown that $\sigma(\mathscr{L}) = \sigma_p(\mathscr{L}) \cup \sigma_c(\mathscr{L}) \cup \sigma_r(\mathscr{L})$.

For an example, consider the differential operator $\mathscr{L} : L^2(0,\infty) \to L^2(0,\infty)$ defined as $(\mathscr{L}x)(t) = x'(t)$ with domain $\{x | x, x' \in L^2(0,\infty)\}$. It turns out that $\sigma_p(\mathscr{L}) = \{\lambda \mid \Re\lambda < 0\}$, $\sigma_c(\mathscr{L}) = \{\lambda \mid \Re\lambda = 0\}$ and $\rho(\mathscr{L}) = \{\lambda \mid \Re\lambda > 0\}$.[120] Hence σ_r is empty. Notice that the values of the point spectrum are not isolated. It may also happen for some operators that the continuous spectrum consists of isolated points so the names may be intuitively misleading.

For matrix operators the spectrum equals the point spectrum and so the values $\lambda \in \sigma_p(\mathscr{L})$ are the familiar eigenvalues. All eigenvalues of a self-adjoint operator are real numbers[121]. For compact operators, all nonzero spectral values are eigenvalues, which constitute a discrete set[121]. If this set is not finite, the elements can be arranged to tend towards zero.

[§]For a function $f : A \to B$, A is called the domain and B the codomain. The set $\{f(x) | x \in A\} \subset B$ is called the image.

For compact operators, the spectral value zero can be either in the point spectrum or in the continuous spectrum.

A linear space A is called *separable*, if a countable set B is everywhere dense in A.[120] In a Banach space A, a *Schauder basis* is a sequence $\{x_n\} \subset A$ such that for any element $x \in A$ there exists a unique sequence of scalars $\{a_n\}$ such that $x = \sum_n a_n x_n$. A separable Hilbert space has a Schauder basis. For example, the $\mathbb{L}^2$ space is separable. When attempting to describe the responses of a physical model in terms of eigenmodes, a burning question is whether the modes constitute a basis.

Let $\mathscr{L} : A \to A$ be a compact self-adjoint linear operator. Then there exists an orthonormal basis $\{x_n\}$ for A, where x_n are the eigenvectors of $\mathscr{L}$ with associated eigenvalues λ_n.[120] Thus any $x \in A$ can be expanded as $x = \sum_n \langle x, x_n \rangle x_n$, where the summation includes all eigenvectors, also those corresponding to the eigenvalue zero. For many physical systems with compact domain, such as the vibrating string and an electromagnetic cavity resonator, the corresponding differential operator is self-adjoint and the corresponding integral operator is compact, whence the spectral theorem is directly applicable. On the other hand, in problems with unbounded domain, such as the scattering problem, this is not so. The Silver-Müller condition renders the Helmholtz operators non-self-adjoint, and the corresponding integral operators are not compact. This may sound odd if one considers that $\nabla \times \nabla \times -k^2$ is the definition of the Helmholtz operator. However, it does not describe any particular physical problem until its domain and codomain are specified, and boundary conditions are inherent properties of the domain.

Let A be a linear space and B its subspace. Let $x, y \in A$ be called equivalent (denoted by $x \sim y$) if $x - y \in B$, i.e., $y = x + b$ with $b \in B$. This means that equivalent elements of A can be obtained from one another by adding an element of B. Then the equivalence class of $x \in A$ is $[x] = \{y | y \sim x\}$. The set of such equivalence classes is denoted A/B and called the *quotient space* (a linear space) of A by subspace B.

The *kernel* of a linear operator $\mathscr{L} : A \to B$ is the linear subspace $\{x \in A | \mathscr{L}(x) = 0\}$. The *co-kernel* of $\mathscr{L} : A \to B$ is the quotient space of B by the image of $\mathscr{L}$. The motivation for these definitions is that the kernel describes the uniqueness of a solution to a problem $\mathscr{L}x = y$ if one exists, whereas the co-kernel describes the constraints set on y for solutions to exist.

An operator $\mathscr{L} : A \to B$ over Banach spaces A and B is called a *Fredholm operator*, if its kernel and co-kernel are finite-dimensional. A compact operator is a Fredholm operator of the first-kind. Operator of the form $\mathscr{I} + \mathscr{L}$, where $\mathscr{L}$ is compact, is a Fredholm operator of the second-kind.

A function of complex variable is called *analytic* (holomorphic) in an open region of the complex plane if it is complex differentiable in this region, i.e., satisfies the Cauchy-Riemann equations. A function of complex variable is called *meromorphic* in an open region of the complex plane if it is analytic in this region except at isolated points, where it has pole singularities.

For operator-valued functions, which map a complex number ω to a second-kind Fredholm operator $\mathscr{I} + \mathscr{L}(\omega)$, we have the following theorem (Analytic Fredholm Theorem[122]): If $\mathscr{L}(\omega) : A \to A$ is analytic and compact for each $\omega \in \Omega$, where $\Omega \subset \mathbb{C}$ is an open and connected set, then either (1) $\mathscr{I} + \mathscr{L}(\omega)$ is nowhere invertible in Ω or (2) $(\mathscr{I} + \mathscr{L}(\omega))^{-1}$ is meromorphic in Ω. In the second case, there exists a discrete set of numbers ω_n, which

are poles of $(\mathscr{I}+\mathscr{L}(\omega))^{-1}$ and the equation $(\mathscr{I}+\mathscr{L}(\omega_n))x=0$ has non-trivial solutions in A. For other ω this inverse exists and is analytic.

4.2 Boundary integral operator approach

The second case in the Analytic Fredholm Theorem defines exactly the resonances that a Fredholm operator of the second-kind can have. Next we show how we can utilize this in the case of electromagnetic scattering.

4.2.1 Resonances

Although the PMCHWT formulation leads to an accurate method for solving plasmonic scattering problems, the associated integral operator is not of first or second kind Fredholm. This happens, because the integral operator $\mathscr{D}_l$ (Eq. (3.37)) is of the form $\mathscr{D}_l=\mathscr{D}_l^{\mathrm{s}}+\mathscr{D}_l^{\mathrm{h}}$, where $\mathscr{D}_l^{\mathrm{s}}$ is compact but

$$\mathscr{D}_l^{\mathrm{h}}\mathbf{f}(\mathbf{r})=-\frac{1}{i\omega\epsilon_l}\nabla\int_{\partial V_l}G_l(\mathbf{r},\mathbf{r}')\nabla_t'\cdot\mathbf{f}(\mathbf{r}')dS' \tag{4.4}$$

is not, due to the gradient operator. The operator $\mathscr{K}$ (Eq. (3.38)) is compact for smooth surfaces [120]. Thus the existing spectral theories known to the author are not directly useful. On the other hand, the Müller formulation for scatterers with smooth boundary can be written in the second-kind Fredholm manner [113,123]

$$(\mathscr{I}+\mathscr{A}(\omega))\mathbf{f}=\mathbf{g}, \tag{4.5}$$

where

$$\mathscr{A}(\omega)=-2\begin{pmatrix}\xi_\mu(-\mu_1\gamma_r\mathscr{K}_1+\mu_2\gamma_r\mathscr{K}_2) & \eta_1\xi_\mu(\epsilon_1\gamma_r\mathscr{D}_1-\epsilon_2\gamma_r\mathscr{D}_2)\\ \xi_\epsilon(-\epsilon_1\gamma_r\mathscr{D}_1+\epsilon_2\gamma_r\mathscr{D}_2)/\eta_1 & \xi_\epsilon(-\epsilon_1\gamma_r\mathscr{K}_1+\epsilon_2\gamma_r\mathscr{K}_2)\end{pmatrix} \tag{4.6}$$

and $\mathbf{f}=(\eta_1\mathbf{J}^{\mathrm{s}},\mathbf{M}^{\mathrm{s}})$, $\mathbf{g}=(2\eta_1\mu_1\xi_\mu\gamma_r\mathbf{H}_{\mathrm{inc}},-2\epsilon_1\xi_\epsilon\gamma_r\mathbf{E}_{\mathrm{inc}})$ and $\xi_\epsilon=1/(\epsilon_1+\epsilon_2)$ and $\xi_\mu=1/(\mu_1+\mu_2)$ as detailed in **Paper II**. The operators $\gamma_r\mathscr{D}_1$ and $\gamma_r\mathscr{D}_2$ appear in combinations $\epsilon_1\gamma_r\mathscr{D}_1-\epsilon_2\gamma_r\mathscr{D}_2$ so that the strong singularity is cancelled [123].

The Analytic Fredholm Theorem then implies that in open and connected subsets Ω of $\mathbb{C}$ where the Müller integral operator is analytic, the resonance frequencies ω_n and associated modes $\mathbf{f}_{0n}$ are defined by

$$(\mathscr{I}+\mathscr{A}(\omega_n))\mathbf{f}_{0n}=\mathbf{0} \tag{4.7}$$

and the resonance frequencies occur at isolated points. In the notation $\mathbf{f}_{0n}$ the zero is used to denote that the functions are in the kernel of $\mathscr{I}+\mathscr{A}(\omega_n)$. The Fredholm property itself assures that the eigenspace $\{\mathbf{f}_{0n}\}$ for each n is finite-dimensional, i.e., there may be only finite degeneracy. For material parameters independent of frequency, the operator $\mathscr{A}$ is analytic in all bounded subsets of the complex plane. However, for metals with Drude type dispersion $\epsilon(\omega)$ as shown in Eq. (2.33), the Green function G takes the form

$$G(\omega)=\frac{e^{i\sqrt{\mu_0\epsilon_0 f(\omega)}R}}{4\pi R} \tag{4.8}$$

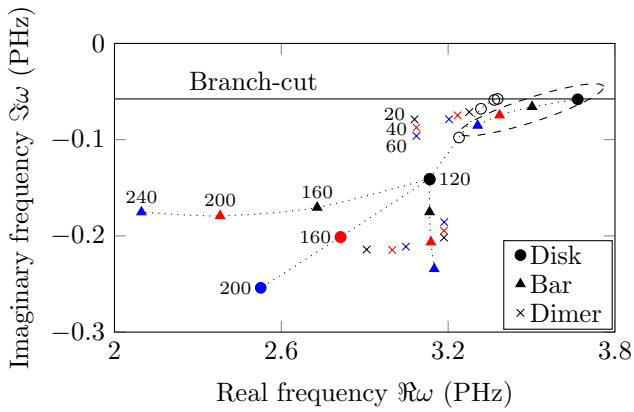

Figure 4.1: Resonance (angular) frequencies of flat gold nanostructures of thickness 20 nm studied in **Paper II**. The numbers and colors refer to disk diameter, bar length and dimer gap that are varied. Open circles correspond to down-scaling the disk. Encircled markers correspond to higher-order resonances of disk and bar. The branch-cut of material refractive index is shown.

where $f(\omega) = \epsilon_\infty \omega^2 - \frac{\omega\omega_p^2}{\omega + i\gamma}$. The branch-points of G are defined by $f(\omega) = 0$ yielding

$$\omega = 0 \quad \text{and} \quad \omega = \frac{1}{2}\left(\pm\sqrt{4\omega_p^2 - \gamma^2} - i\gamma\right), \tag{4.9}$$

which give rise to two branch-cuts for G and thus $\mathscr{A}(\omega)$. These cuts restrict the region of analyticity for $\mathscr{A}(\omega)$. Apart from the material dispersion, the Green function can restrict the region of analyticity. For example, the spectral form of the periodic Green function (3.48) has pole singularities determined by $k_z = \sqrt{\omega^2\epsilon\mu - \mathbf{k}_t \cdot \mathbf{k}_t} = 0$. These correspond to nulls of the inverse operator $(\mathscr{I} + \mathscr{A}(\omega))^{-1}$, whence at such frequencies the response of the structure vanishes for all excitations. In the complex k-plane, the Green function of the stratified medium (Eq. (3.33)) has branch-cuts related to radiative continua and poles related to surface waves, which also restrict the region of analyticity.

We call the discussed approach the spectral Müller method. It allows one to find the resonance frequencies of a scatterer without the specification of an incident field, thus providing a direct way to characterize, e.g., plasmon resonances of metal particles.

In **Paper II**, we used the MOM to discretize the spectral Müller method and sought the lowest order resonance frequencies of flat gold disks, disk dimers and bars. The results are shown in Fig. 4.1. It is seen that the resonances shift according to the size and aspect ratio of the particle. The degenerate resonance of the disk is broken, when it is elongated into a bar shape or another disk is introduced.

4.2.2 Expansions

We next discuss the expansion of solutions in terms of eigenfunctions $\mathbf{f}_{0n}$ following the development by Baum, Marin *et al.* for the MFIE of perfectly conducting objects[124–128]. If Eq. (4.7) holds for some ω_n, then there exists $\mathbf{h}_{0n}$ satisfying

$$(\mathscr{I} + \mathscr{A}^\dagger(\omega_n))\mathbf{h}_{0n}^* = \mathbf{0}. \tag{4.10}$$

We assume that both $\mathbf{f}_{0n}$ and $\mathbf{h}_{0n}$ are normalized in the norm induced by the $\mathbb{L}^2$ inner-product. Assuming that the inverse $(\mathscr{I} + \mathscr{A}(\omega))^{-1}$ has only pole singularities, we can expand $\mathbf{f}$ in the neighbourhood of ω_n as

$$\mathbf{f}(\omega) = \sum_{p=1}^{P} \sum_{m=1}^{M} C_{npm} \frac{\mathbf{f}_{0npm}}{(\omega - \omega_n)^p} + \mathbf{f}'_n \tag{4.11}$$

where C_{npm} are constants and the resonant mode has been assumed to have degeneracy M and pole order P. The function $\mathbf{f}'_n$ is bounded but otherwise unspecified. Because the excitation $\mathbf{g}$ and the operator $\mathscr{A}(\omega)$ are analytic, they are expanded in Taylor series around ω_n:

$$\mathscr{A}(\omega) = \mathscr{A}(\omega_n) + \sum_{q=1}^{\infty} (\omega - \omega_n)^q \mathscr{B}_{nq} \tag{4.12}$$

$$\mathbf{g} = \sum_{q=0}^{\infty} (\omega - \omega_n)^q \mathbf{g}_{nq}, \tag{4.13}$$

where

$$\mathscr{B}_{nq} = \frac{1}{q!} \mathscr{A}^{(q)}(\omega_n), \qquad \mathbf{g}_{nq} = \frac{1}{q!} \mathbf{g}^{(q)}(\omega_n) \tag{4.14}$$

and the superscript (q) denotes the q:th derivative. The original developments by Baum *et al.* were focused on delta distribution temporal excitation, whose Fourier transform can be expanded in Taylor series without problems. For ideally time-harmonic excitations, the expansion (4.13) does not exist, but in reality, one can consider that a sinusoidal excitation has some finite spectral width.

Now consider the following [127]:

$$\langle (\mathscr{I} + \mathscr{A}(\omega))\mathbf{f}, \mathbf{h}_{npm} \rangle = \langle \mathbf{g}, \mathbf{h}_{npm} \rangle \tag{4.15}$$

By the use of $\langle (\mathscr{I} + \mathscr{A}(\omega_n))\mathbf{f}, \mathbf{h}_{npm} \rangle = \left\langle \mathbf{f}, (\mathscr{I} + \mathscr{A}^\dagger(\omega_n))\mathbf{h}_{npm} \right\rangle = 0$ we get

$$\langle (\mathscr{A}(\omega) - \mathscr{A}(\omega_n)))\mathbf{f}, \mathbf{h}_{npm} \rangle = \langle \mathbf{g}, \mathbf{h}_{npm} \rangle . \tag{4.16}$$

By substituting the previous expansions, the coefficients C_{npm} can be identified. To simplify things, only poles of first order are considered, whence the index p is dropped. Then it follows that

$$C_{nm} = \frac{\langle \mathbf{g}_n, \mathbf{h}_{0nm} \rangle}{\langle \mathscr{B}_n \mathbf{f}_{0nm}, \mathbf{h}_{0nm} \rangle}. \tag{4.17}$$

We may then expand the solution as

$$\mathbf{f}(\omega) = \sum_{nm} C_{nm} \frac{\mathbf{f}_{0nm}}{\omega - \omega_n} + \mathscr{E}(\omega)\mathbf{g}, \tag{4.18}$$

where $\mathscr{E}$ is an entire operator valued function [127]. This is the so-called singularity expansion method (SEM). The time-domain response is easily obtained by taking the inverse Laplace transform, where the Bromwich contour encloses all poles. Each pole then gives rise to a temporally decaying sinusoid, with decay rate related to $\Im\omega_n$. Although the entire

function is generally unknown, it has been conjectured to only play a significant role for the early-time response[129]. If the operator $\mathscr{A}$ is not analytic due to the presence of, e.g., branch-cuts from material dispersion, then integration over the cuts may appear as part of Eq. (4.18)[130]. From this perspective, we may state that the modes $\mathbf{f}_{0nm}$ constitute a Schauder basis only if such branch-cuts don't exist and if $\mathscr{E}$ vanishes.

It is noteworthy that the scattered fields obtained via the Stratton-Chu integral operators from the modes $\mathbf{f}_{0nm}$ are spatially exponentially growing away from the scatterer. This follows directly from the fact that $\Im\omega < 0$ and the Silver-Müller condition (3.13), i.e., far away from the scatterer, the electric field is of the form

$$\mathbf{E} = \mathbf{A}\frac{e^{i\omega R/c}}{4\pi R} = \mathbf{A}\frac{e^{i\Re\omega R/c}e^{-\Im\omega R/c}}{4\pi R}, \tag{4.19}$$

where $\Im\omega < 0$. For realistic time-domain analysis, this poses no difficulty due to causality, which forces the scattered field to zero for distances greater than ct, where the origin of time t corresponds to the incident wave first hitting the scatterer.

Another approach, which we presented in **Paper II**, was to define an eigenvalue problem at a fixed real frequency ω as

$$(\mathscr{I} + \mathscr{A}(\omega))\mathbf{f}_n = \lambda_n \mathbf{f}_n. \tag{4.20}$$

These modes constitute a discrete set due to compactness of $\mathscr{A}$. The modes and eigenvalues are now functions of ω. It is clear that $\lambda_n(\omega)$ tends to zero as $\omega \to \omega_n$. If one attempts to expand the solution as

$$\mathbf{f} = \sum_n \alpha_n \mathbf{f}_n \tag{4.21}$$

the expansion coefficients can be found by first considering the adjoint equation

$$(\mathscr{I} + \mathscr{A}^\dagger(\omega))\mathbf{h}_n = \lambda_n^* \mathbf{h}_n, \tag{4.22}$$

and the application of the inner-product results in

$$\sum_n \alpha_n \lambda_n \langle \mathbf{h}_n, \mathbf{f}_n \rangle = \langle \mathbf{h}_n, \mathbf{g} \rangle . \tag{4.23}$$

This is a finite linear system of equations. If there are no degenerate modes, we get simply

$$\alpha_n = \frac{\langle \mathbf{h}_n, \mathbf{g} \rangle}{\lambda_n \langle \mathbf{h}_n, \mathbf{f}_n \rangle}. \tag{4.24}$$

This eigenmode expansion turned out to be a practical approach, but it has certain weak points as compared to SEM. It is very difficult to shed any light into whether these modes constitute a Schauder basis of $\mathbb{L}^2$. Secondly, for $\lambda_n \neq 0$, the modes are not fully source-free solutions to the scattering problem: the fields they produce do satisfy the Helmholtz equations and the radiation condition[§], but they don't satisfy the interface conditions. The jump in the interface conditions can be thought to correspond to an excitation source, which most suitably excites the mode.

[§]These are imposed by the use of the Stratton-Chu integral operators.

Plasmon resonances and modes have been long understood on the basis of the quasistatic theory, where a compact self-adjoint operator describes the response in terms the electrostatic potential ϕ or surface charge density σ.[60,131–135] By using the result that in the Müller formulation the zero frequency limit exists, we were able to deduce that the modes $\mathbf{f}_n$ tend towards electro- and magnetostatic modes in the limit $\omega \to 0$.

As the Mie theory has been extensively used to understand the scattering from spherical particles as a superposition of multipole fields, it is important to see the connection between the general integral operator mode theory and the Mie theory. We showed in **Paper II** that transverse-electric (TE) and transverse-magnetic (TM) modes of the form

$$\mathbf{f}_{lm}^{\mathrm{TE}} = (a_l \mathbf{n} \times \nabla_t Y_{lm}, b_l \nabla_t Y_{lm}), \tag{4.25}$$

$$\mathbf{f}_{lm}^{\mathrm{TM}} = (a_l \nabla_t Y_{lm}, b_l \mathbf{n} \times \nabla_t Y_{lm}) \tag{4.26}$$

are eigenfunctions of Eq. (4.20). These are the tangential traces of the multipole fields defined over $\mathbb{R}^3$ that appear in the Mie theory.

5 Solution methods

This Chapter considers methods for obtaining approximate solutions to the previously discussed linear and nonlinear scattering problems. We first consider the important special case of a spherical particle and the multipole solution. Then we the apply the method of moments for other Lipschitz geometries in the boundary integral formalism. We discuss the development of suitable basis functions to construct a finite-dimensional approximate solution spaces and the linear algebraic properties of the resulting system of equations. We also consider some aspects of the efficient evaluation of the periodic Green function and the evaluation of boundary element near-interactions.

5.1 Multipole series: Mie theory

Consider the spherical coordinates $\theta \in [0, \pi]$ and $\phi \in [0, 2\pi]$ as illustrated in Fig. 5.1. We denote the spherical harmonics by $Y_{lm}(\theta, \phi)$ with $l = 0, 1, \ldots, \infty$ and $m = -l, -l + 1, \ldots, l-1, l$.[46] The angular momentum operator is defined as $\mathbf{L} = -i\mathbf{r} \times \nabla$, which induces the vector spherical harmonics $\mathbf{X}_{lm} = [l(l+1)]^{-1/2}\mathbf{L}Y_{lm}$.[46] Consider $\mathbb{L}^2(S)$ as the Hilbert space of $S \to \mathbb{C}^3$ functions over a spherical surface S endowed with the inner-product

$$\langle \mathbf{f}, \mathbf{g} \rangle = \int_0^{2\pi} \int_0^{\pi} \mathbf{f}^*(\theta, \phi) \cdot \mathbf{g}(\theta, \phi) \sin\theta d\theta d\phi. \tag{5.1}$$

The functions $\mathbf{X}_{lm}$ constitute an orthonormal basis of $\mathbb{L}^2(S)$ with the following orthogonality properties:

$$\langle \mathbf{X}_{l'm'}, \mathbf{X}_{lm} \rangle = \delta_{ll'}\delta_{mm'}, \tag{5.2}$$

$$\langle \mathbf{X}_{l'm'}, \mathbf{r} \times \mathbf{X}_{lm} \rangle = 0. \tag{5.3}$$

The internal and scattered fields for a spherical scatterer can then be written in the form[46]

$$\mathbf{E} = \eta \sum_{l=0}^{\infty} \sum_{m=-l}^{l} \frac{i}{k} B_{lm} \nabla \times f_l(kr)\mathbf{X}_{lm} + A_{lm} g_l(kr)\mathbf{X}_{lm} \tag{5.4}$$

$$\mathbf{H} = \sum_{l=0}^{\infty} \sum_{m=-l}^{l} -\frac{i}{k} A_{lm} \nabla \times g_l(kr)\mathbf{X}_{lm} + B_{lm} f_l(kr)\mathbf{X}_{lm}, \tag{5.5}$$

where the terms associated with scalars B_{lm} are the transverse magnetic multipoles and the terms associated with scalars A_{lm} are the transverse electric multipoles[§]. In general

[§]The multipole fields come in many disguises depending on the author. In Refs. 12,106 TE and TM multipoles are denoted by $\mathbf{N}_{lm}$ and $\mathbf{M}_{lm}$. Some authors use a set of three multipoles $\mathbf{Y}_{lm} = \mathbf{r}/|\mathbf{r}|Y_{lm}, \mathbf{\Psi}_{lm} = r\nabla_t Y_{lm}, \mathbf{\Phi}_{lm} = \mathbf{r} \times \nabla_t Y_{lm}$.[136]

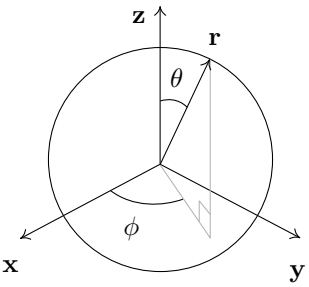

Figure 5.1: The spherical coordinates.

f_l and g_l are each combinations of the form $C_l^{(1)} h_l^{(1)} + C_l^{(2)} h_l^{(2)}$, where $h_l^{(1)}$ and $h_l^{(2)}$ are the spherical Hankel functions of the first and second kind, respectively. For the internal fields of the scattering problem, $f_l = g_l = j_l$, where j_l is the spherical Bessel function of the first kind and is bounded at zero. For the scattered fields $f_l = g_l = h_l^{(1)}$, which is an asymptotically outwards propagating spherical wave for the Fourier components $\exp(-i\omega t)$. This choice ensures that the Silver-Müller condition is satisfied.

We'll briefly state a few of the remarkable properties of the multipole fields. The associated moments are uniquely determined by the normal components of the electric and magnetic fields over a spherical shell[46]:

$$A_{lm} g_l(kr) = \frac{k}{\sqrt{l(l+1)}} \langle Y_{lm}\mathbf{r}, \mathbf{H} \rangle , \tag{5.6}$$

$$\eta B_{lm} f_l(kr) = -\frac{k}{\sqrt{l(l+1)}} \langle Y_{lm}\mathbf{r}, \mathbf{E} \rangle . \tag{5.7}$$

In general two different shells are required to determine the relative factors $C^{(1)}$ and $C^{(2)}$ in f_l and g_l, but for the scattering problem these are already fixed[46]. A field $\mathbf{f}$ has parity ± 1, if $\mathbf{f}(-\mathbf{r}) = \pm\mathbf{f}(\mathbf{r})$ for all $\mathbf{r} \in \mathbb{R}^3$. The multipole fields have a well-defined parity. Specifically, $\nabla \times f_l(kr)\mathbf{X}_{lm}$ has parity $(-1)^{l+1}$ and $g_l(kr)\mathbf{X}_{lm}$ has parity $(-1)^l$. This has implications on how different multipoles interfere in forward and backward directions. For example, the electric dipole and the magnetic dipole have opposite parities and thus may interfere so as to suppress back-scattering and enhance forward-scattering[137–140]. The application of multipole fields to study the response of non-spherical nanostructures is also very common[141–143].

To solve the problem of electromagnetic plane-wave scattering by a sphere, the strategy is to express the incident, scattered and internal fields by Eqs. (5.4) and (5.5). Consider a non-magnetic ($\mu = \mu_0$) sphere of radius a with refractive index n_2 and that of the surrounding medium n_1. The coefficients of a plane-wave incident field of the form $(\mathbf{x} \pm i\mathbf{y})\exp(ikz)$ are known in closed form[46]: $A_{lm} = C_l/\eta$ and $B_{lm} = \pm C_l/(i\eta)$, where $C_l = i^l\sqrt{4\pi(2l+1)}$ and $m = \pm 1$. Finally the tangential continuity of the fields across the particle surface is enforced. Here the orthogonality properties of the multipoles are used

to obtain the expansion coefficients for the internal and scattered fields. The latter read

$$A^{\mathrm{s}}_{lm} = \left(\frac{C_l}{\eta_1}\right) \frac{\psi_l(Nx)\psi_l'(x) - N\psi_l(x)\psi_l'(Nx)}{N\xi_l(x)\psi_l'(Nx) - \psi_l(Nx)\xi_l'(x)}, \tag{5.8}$$

$$B^{\mathrm{s}}_{lm} = \pm\left(\frac{C_l}{i\eta_1}\right) \frac{\psi_l'(Nx)\psi_l(x) - N\psi_l'(x)\psi_l(Nx)}{N\xi_l'(x)\psi_l(Nx) - \psi_l'(Nx)\xi_l(x)}, \tag{5.9}$$

where we used the Riccati-Bessel functions $\psi_l(x) = xj_l(x)$ and $\xi_l(x) = xh_l^{(1)}(x)$, the relative index of refraction $N = n_2/n_1$ and the size parameter $x = n_1 k_0 a$.

Now consider surface second-harmonic generation due to polarization with only the second-order surface susceptibility component $\chi^{\mathrm{s}}_{\mathrm{nnn}}$ non-zero. The interface conditions (2.17) and (2.18) become

$$(\mathbf{E}_1 - \mathbf{E}_2)_t = -\frac{1}{\epsilon'}\nabla_t \mathcal{P}_{\mathrm{n}}, \tag{5.10}$$

$$(\mathbf{H}_1 - \mathbf{H}_2)_t = \mathbf{0}. \tag{5.11}$$

The solution proceeds the same way as for linear scattering, but when enforcing the interface conditions, the orthogonality of the multipoles is not trivially exploited. Lets first consider the TE fields, whose electric fields are linear combinations of $\mathbf{X}_{lm}$. Enforcing Eq. (5.10) leads to

$$A_{lm} \propto \langle \mathbf{X}_{lm}, \nabla_t \mathcal{P}_{\mathrm{n}} \rangle . \tag{5.12}$$

By partial integration we get $\langle \mathbf{X}_{lm}, \nabla_t \mathcal{P}_{\mathrm{n}} \rangle = -\langle \nabla_t \cdot \mathbf{X}_{lm}, \mathcal{P}_{\mathrm{n}} \rangle$, which is zero, because $\nabla_t \cdot \mathbf{X}_{lm} = 0$ identically. Thus the component $\chi^{\mathrm{s}}_{\mathrm{nnn}}$ gives rise to purely transverse magnetic response and[§]

$$B_{lm} \propto \left\langle \mathbf{n} \times \mathbf{X}_{lm}, \nabla_t (e_n^2) \right\rangle = -\frac{i\sqrt{l(l+1)}}{a} \left\langle Y_{lm}, e_n^2 \right\rangle , \tag{5.13}$$

where we used $\mathcal{P}_{\mathrm{n}} = \epsilon_0 \chi^{\mathrm{s}}_{\mathrm{nnn}} e_n^2$, where e_n is the normal component of the fundamental field. Because e_n is a linear combination of Y_{lm}, we get

$$B_{lm} \propto \sum_{l_1,l_2,m_1,m_2} m_1 m_2 E_{l1} E_{l2} \left\langle Y_{lm}, Y_{l_1 m_1} Y_{l_2 m_2} \right\rangle . \tag{5.14}$$

Now

$$\begin{aligned} \langle Y_{lm}, Y_{l_1 m_1} Y_{l_2 m_2} \rangle = (-1)^m \sqrt{\frac{(2l+1)(2l_1+1)(2l_2+1)}{4\pi}} \\ \cdot \begin{pmatrix} l & l_1 & l_2 \\ -m & m_1 & m_2 \end{pmatrix} \begin{pmatrix} l & l_1 & l_2 \\ 0 & 0 & 0 \end{pmatrix}, \end{aligned} \tag{5.15}$$

where the parenthesis factors are the Wigner 3-j symbols. They are non-zero only provided that $m = m_1 + m_2$ and $|l_1 - l_2| \leq l \leq (l_1 + l_2)$ and $l + l_1 + l_2$ is even. These work as selection rules for surface SHG. For example, the last condition implies that purely

[§]Here it is useful to know that $\sqrt{l(l+1)}\nabla_t \cdot (\mathbf{n} \times \mathbf{X}^*_{lm}) = -ia\nabla_t^2 Y^*_{lm}$ and that $r^2\nabla_t^2 Y_{lm} = -l(l+1)Y_{lm}$.

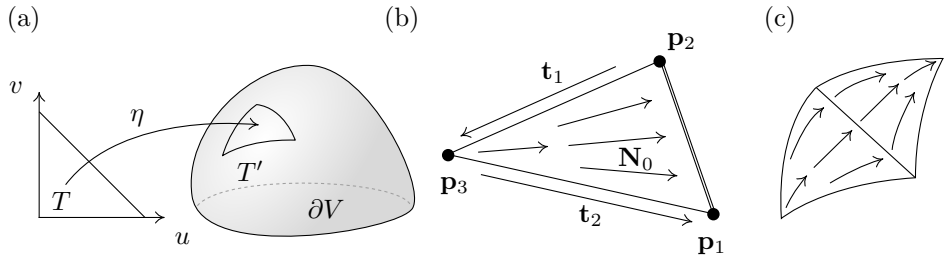

Figure 5.2: Geometrical subsectioning and triangular basis functions for numerical computations.

dipolar fundamental field cannot produce dipolar second-harmonic field. Furthermore, in general only $m = 0, \pm 2$ values appear for the second-harmonic fields. Prior to Author's work, surface SHG from spheres has been studied in the small particle limit [144,145] and via reciprocity for arbitrary spheres [146]. Recently the full-wave single sphere case was revisited [147] and more advanced work has been done for shell structures [148], focused beam excitations [149,150], systems of spheres [151] and different types of surface sources [152,153].

5.2 Boundary element method

We now consider the approximate solution to the linear and second-harmonic scattering problems in the PMCHWT boundary integral formulation by the method of moments. The task is to find a finite-dimensional space that can be made arbitrarily close to $\mathcal{H}^{-1/2}(\mathrm{div}, \partial V)$ for each domain V in the scattering problem. The equivalent surface current densities are expanded in a basis of such a space and the expansion coefficients are solved from a linear system of equations, which results by requiring that the residual error is orthogonal to a so-called test space. The choice of the test space turns out to be non-trivial. At first the most logical approach would appear to be to approximate $\mathcal{H}^{-1/2}(\mathrm{curl}, \partial V)$, which is the co-domain of the pertinent integral operators. However, it has been shown that by choosing the test space also as a subspace of $\mathcal{H}^{-1/2}(\mathrm{div}, \partial V)$, the dual of the range, more accurate results are obtained [117]. The choice of equal sets of basis and test functions is called the Galerkin method.

The construction of the finite-dimensional space starts by finding a suitable representation of the boundary surface ∂V. For subsectional basis functions, the surface is usually split according to the supports of the desired basis functions. We consider triangular supports. Consider the canonical triangle $T = \{(u, v) | u, v \in [0, 1], u + v \leq 1\}$. From this domain, we may construct a parametrization $\eta : T \to T'$ for a triangle $T' \subset \partial V$, which may be curved. This is illustrated in Fig. 5.2(a). One computationally convenient way to construct such parametrizations is by

$$\eta(u, v) = \sum_{n=1}^{N_s} S_n(u, v)\mathbf{r}_n, \ (u, v) \in T, \tag{5.16}$$

where S_n are the shape functions and $\mathbf{r}_n \in \partial V$ are constant nodes [154]. For a flat triangle with vertices $\mathbf{r}_1, \mathbf{r}_2, \mathbf{r}_3$, the shape functions are $S_1 = u, S_2 = v, S_3 = 1 - u - v$. Surface

integral of some function f over T' is then

$$\int_{T'} f(\mathbf{r})dS = \int_0^1 \int_0^{1-u} f(\eta(u,v))\sqrt{g(u,v)}dvdu, \tag{5.17}$$

where $g(u,v) = \left|\frac{\partial\eta}{\partial u} \times \frac{\partial\eta}{\partial v}\right|^2$ is the determinant of the metric tensor of η.

For the construction of basis functions over the triangular domains, the tangent space over T' should be judiciously presented. Consider the triangle in Fig. 5.2(b) and the highlighted edge between nodes $\mathbf{p}_1$ and $\mathbf{p}_2$. Define the following tangent vectors:

$$\mathbf{t}_1 = -\frac{1}{\sqrt{g}}\frac{\partial\eta}{\partial v}, \qquad \mathbf{t}_2 = \frac{1}{\sqrt{g}}\frac{\partial\eta}{\partial u}, \tag{5.18}$$

which are tangential to the two other edges. One may then define triangle edge basis functions of zeroth and first degree assigned to the highlighted edge[155]:

$$\mathbf{N}_0 = u\mathbf{t}_2 - v\mathbf{t}_1, \tag{5.19}$$

$$\mathbf{N}_1 = u\mathbf{t}_2 + v\mathbf{t}_1. \tag{5.20}$$

These triangle basis functions do not by themselves yield a divergence-conforming space, i.e., a space where the divergence is globally defined. For this reason, it is necessary to define the basis functions as two-triangle patches that share a common edge. The definition of $\mathbf{N}_n$ allows one to easily construct basis functions over such patches as linear combinations with simple ± 1 coefficients so that the edge normal component is continuous as illustrated in Fig. 5.2(c). The space spanned by the patch functions is divergence-conforming. The basis functions for the other edges can be defined by permuting the node indices. For a triangle patch with shared edge length l, the function $l\mathbf{N}_0$ is the original RWG basis function over a triangle of a patch[17]. It is straightforward to define higher-order edge elements in the form $f_1(u,v)\mathbf{t}_1 + f_2(u,v)\mathbf{t}_2$, but full polynomial orders higher than 1 also require interior basis functions, which vanish over the edges[155]. Note also that the parametrization η does not have to be constructed via the shape functions. The basis functions can be constructed for any diffeomorphic chart so that, in principle, the geometry of the scatterer can be exactly described. The aforementioned functions are hierarchical, meaning that polynomial order refinement (p-refinement) is possible[155]. Similar divergence-conforming bases were developed in Refs. 156,157. Interpolatory bases have also been developed for BEM[158] and other supports, such as quadrangles[159,160], have been utilized. BEM has also been developed in the language of differential forms with a generalized method for constructing basis functions by the cohomology theory[161].

We associate a finite-dimensional subspace $\mathbb{T}_l \subset \mathcal{H}^{-1/2}(\mathrm{div}, \partial V)$ of dimension N_l spanned by the RWG triangle patch basis functions for each domain V_l with $l = 1, 2, \ldots, N_D$. The support of the basis function $\mathbf{f}_n^l$ associated with domain V_l and local edge n is denoted by S_n^l. The equivalent surface current densities are then expanded as

$$\mathbf{J}_l^{\mathrm{s}} = \sum_{n=1}^{N_l} \alpha_n^l \mathbf{f}_n^l, \qquad \mathbf{M}_l^{\mathrm{s}} = \sum_{n=1}^{N_l} \beta_n^l \mathbf{f}_n^l \tag{5.21}$$

with $\alpha_n^l, \beta_n^l \in \mathbb{C}$. We define the coefficient vectors $\mathbf{x}_l = \{\alpha_1^l, \ldots, \alpha_{N_l}^l, \beta_1^l, \ldots, \beta_{N_l}^l\}^T$.

When dealing with multi-domain problems, it is convenient to consider the discretization of the boundary integral equations for each domain V_l with closed boundary ∂V_l separately

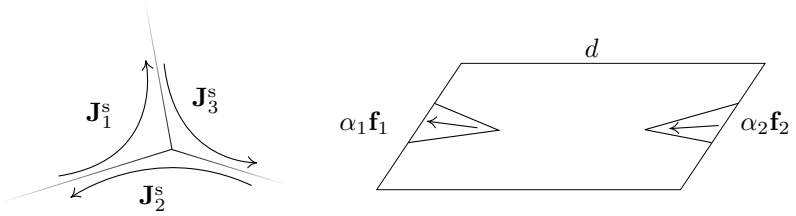

Figure 5.3: Constraints on equivalent surface current densities. (a) For adjacent domains $\mathbf{J}^{\mathrm{s}}_n = -\mathbf{J}^{\mathrm{s}}_m$ and $\mathbf{M}^{\mathrm{s}}_n = -\mathbf{M}^{\mathrm{s}}_m$ for $n, m = 1, 2, 3$ and $n \neq m$.(b) In periodic domains, the Bloch condition imposes $\alpha_1\mathbf{f}_1 = \alpha_2\mathbf{f}_2 \exp(i\mathbf{k}_0 \cdot \boldsymbol{\rho}_{10})$ and similarly for β_n and the other periodic dimension.

and then combine the results. Upon combination, one has to enforce the continuity of the tangential electric and magnetic fields. We adopt the scheme of Ref. 162, where the basis functions for each domain are "oriented" with respect to one another as illustrated in Fig. 5.3(a). Thus we next assume that the basis functions in the sets $\{\mathbf{f}^1_n\}, \ldots, \{\mathbf{f}^{N_D}_n\}$ are oriented in such a way. We then apply the Galerkin method by testing the PMCHWT equations (3.53) and (3.54) with the RWG functions via the $\mathbb{L}^2(\partial V_l)$ inner-product to obtain the weak form

$$\mathrm{Z}_l \mathbf{x}_l = \mathbf{b}_l, \tag{5.22}$$

where (see Section 3.6)

$$\mathrm{Z}_l = \begin{pmatrix} \mathrm{D}_l & -\mathrm{K}_l \\ \mathrm{K}_l & \mathrm{D}_l/\eta_l^2 \end{pmatrix} \tag{5.23}$$

with matrix elements

$$(\mathrm{D}_l)_{mn} = -i\omega\mu_l \int_{S^l_m} \mathbf{f}^l_m(\mathbf{r}) \cdot \int_{S^l_n} G_l(\mathbf{r}, \mathbf{r}') \mathbf{f}^l_n(\mathbf{r}') dS' dS \tag{5.24}$$

$$- \frac{1}{i\omega\epsilon_l} \int_{S^l_m} \nabla_t \cdot \mathbf{f}^l_m(\mathbf{r}) \int_{S^l_n} G_l(\mathbf{r}, \mathbf{r}') \nabla'_t \cdot \mathbf{f}^l_n(\mathbf{r}') dS' dS, \tag{5.25}$$

$$(\mathrm{K}_l)_{mn} = \int_{S^l_m} \mathbf{f}^l_m(\mathbf{r}) \cdot \int_{S^l_n} \nabla' G_l(\mathbf{r}, \mathbf{r}') \times \mathbf{f}^l_n(\mathbf{r}') dS' dS, \tag{5.26}$$

where partial integration was used to lower the degree of singularity in $\mathscr{D}_l$ as is possible when the basis functions belong to $\mathcal{H}^{-1/2}(\mathrm{div}, \partial V)$.[18] The source vector elements are

$$(\mathbf{b}_l)_m = \delta_{l1} \left\langle \mathbf{f}^l_m, \mathbf{E}_{\mathrm{inc}} \right\rangle, \tag{5.27}$$

$$(\mathbf{b}_l)_{N_l+m} = \delta_{l1} \left\langle \mathbf{f}^l_m, \mathbf{H}_{\mathrm{inc}} \right\rangle. \tag{5.28}$$

The matrices D_l and K_l can be calculated separately. To obtain the final solvable problem in the form

$$\mathrm{Z}\mathbf{x} = \mathbf{b} \tag{5.29}$$

the matrix elements of D_l and K_l are added to Z according to the edge child-parent relations of the full mesh and the subdomain meshes as discussed in Ref. 162 and

Paper III. The dimension N of the matrix Z is then $2N_e$, where N_e is the total number of unique edges in the mesh that contains all the domain boundaries.

For periodic problems, where the fields are constrained by the Bloch conditions (3.24) and (3.25), the equivalent surface current densities must also satisfy such constraints [163]. This is only relevant if some of the boundary surfaces ∂V_l touch the boundaries of the unit cell of the periodic structure. This happens in practice for, e.g., nanoparticles on a substrate. The coefficients related to the half-RWG functions that appear at the opposite sides of the unit cell (see Fig. 5.3(b)) are linearly dependent and thus to obtain a non-singular system matrix, one of them must be substituted out. Thus the dimension of the matrix Z is reduced by half the number of edges on the unit cell boundary. For the RWG basis it's also important that the mesh has translational symmetry, so that edges map to edges over the unit cell boundary.

The evaluation of G_p along with its gradient for periodic problems via Eqs. (3.28) and (3.29) is still quite time-consuming due to the multiple evaluations of the erfc function. Its pre-computation by direct ordered grid-based linear interpolation [164–166] and approximation by orthogonal polygonal families, such as Chebyshev [167], have been proposed. The precomputation of G_p and $\nabla' G_p$ means precomputing four complex-valued scalar functions of three variables, which easily requires a lot of memory and causes cache issues. The Author's approach was to instead use linear interpolation for the sum-term functions in the form

$$G_{ps}^{\text{spat}} = \sum_{n=-\infty}^{\infty} \sum_{m=-\infty}^{\infty} e^{i\mathbf{k}_0 \cdot \boldsymbol{\rho}_{nm}} g_1(R_{nm}), \tag{5.30}$$

$$G_{ps}^{\text{spec}} = \sum_{n=-\infty}^{\infty} \sum_{m=-\infty}^{\infty} e^{i\mathbf{k}_t \cdot \mathbf{R}} g_2(z - z'), \tag{5.31}$$

where the subscript s means that the smooth part of the Green function after singularity subtraction is considered. The truncation of the sums is first chosen and then appropriate ranges for the domains of g_1 and g_2 are chosen. These functions are of the form $\mathbb{R} \to \mathbb{C}$, which are easily pre-computed, stored and evaluated. A similar scheme is applied to $\nabla' G_p$, but the spectral part requires one scalar function for the xy-components and another for the z-component. The drawback of this approach is that, for high truncation numbers, the evaluation becomes increasingly time-consuming, although in practice n, m range from -2 to 2 at most.

In **Paper V**, the linear and second-order response of L- and T-shaped gold nanoparticle arrays were studied experimentally and numerically. The arrays had spatial periodicities of length 500 nm along two orthogonal directions. Figure 5.4 shows the scanning electron microscope images of the unit cells along with the measured optical density spectra and their BEM simulations. The particle shapes used in the simulations were deduced carefully from the images and the substrate was taken into account. This resulted in almost quantitative agreement between the measurements and the simulations.

The evaluation of the matrix elements can be done by applying Gaussian quadrature for the well separated source and test elements. The Author's experience is that a 4-point Gauss-Legendre quadrature is often sufficiently accurate, but this depends on the problem type and the size of the triangles with respect to wavelength. In the evaluation of the matrix elements that are nearby, care must be taken due to the singularities of the Green function. In the PMCHWT method the situation is not too bad, because the D_l matrices

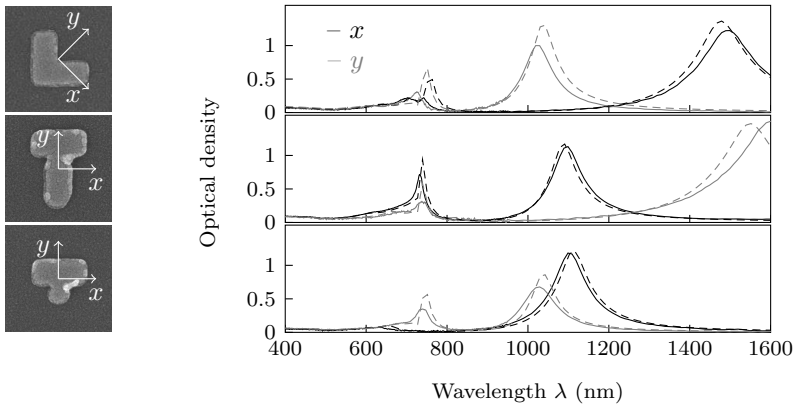

Figure 5.4: Scanning electron microscope images and optical densities of L- and T-shaped gold nanoparticle arrays. Solid lines (–) are measured data and dashed lines (– –) are BEM results. Both x- and y-polarized incident plane-waves are considered and denoted by black and gray colors respectively.

contain only weak singularities. For smooth surfaces, the K_l matrices also contain weak singularities, but for sharp corners the singularities are strong and problematic. These singularities pose grave difficulties for designing a general purpose boundary integral solver, because the most efficient methods for evaluating the matrix elements require specific knowledge of the basis functions and the geometrical elements. The singularity subtraction method[168], which is employed by the author, works only for flat geometrical elements. The first derivations were for RWG and rooftop functions[168–172], but the method has been generalized to higher-order basis functions, while still assuming flat geometry[173,174]. Note than when using the periodic Green function, it may be necessary to also subtract more than one singularity. In the Author's implementation, all the nine singularities, that may be problematic, were subtracted.

The weakly singular integral kernels can be regularized by purely numerical means by utilizing certain coordinate transformations, whose Jacobian cancels a weak singularity. Such methods are, e.g., the Duffy[175] and the Lachat-Watson[176] transformations. They work naturally for the self-elements (the diagonals of Z), but become cumbersome for other nearby elements. Other numerical methods have been developed to handle these nearby cases and higher singularities[177–184], but they are inherently complicated and contrived. Thus it is not clear, whether the use of curved elements or high-order basis functions is in general beneficial for BEM.

The Author's implementation is written in Fortran 90 and utilizes shared memory parallelization via OpenMP. Even though the matrix elements are independent and the element calculation thus amenable for direct parallelization, this is not the most efficient method. It was recognized very early that it is more efficient to build the loops with respect to triangles instead of matrix elements[18]. This is because each triangle supports three RWG functions. Thus it is possible to minimize the amount of the Green function evaluations, which usually dominates the matrix fill time. Parallelization can still be utilized, but in a more delicate manner.

Once the system matrix Z (dimension N) and the source vector $\mathbf{b}$ are obtained, the vector $\mathbf{x}$ is solved by the use of linear algebraic methods. From this point of view, it

is essential to note that the matrix Z is full and non-Hermitian. In the PMCHWT formulation, it also has a high condition number. Thus the memory requirements for the storage scale as $O(N^2)$ and the solution time scales as $O(N^3)$ for direct methods, such as the LU decomposition. It is the Author's experience that the LU decomposition with partial pivoting is a good choice when the highly optimized routines of the linear algebra package (LAPACK) Fortran library are utilized. Due to the lack of Hermiticity and other symmetry properties, the general minimal residual (GMRES) method [185] with restart is the only attractive iterative method, but due to the high condition number resulting in the PMCHWT formulation, it may fail to reach a reasonable error level in less than N steps. There are numerous preconditioner schemes that can be used to lower the condition number [185]. The Calderón projector based preconditioners are one of the most effective but also most arduous to implement [186–188].

Due to the previously discussed scaling properties, the basic BEM implementation is only practical if the dimension N is less than 10^4. However, for many scattering problems, the full matrix Z has some type of redundancy. The FMM is based on the observation, that for scatterers much larger than wavelength, the field due to a localized group of elements sufficiently far away can be described accurately as a truncated sum of multipoles [19–21]. This leads to a formulation, where only a fraction of the system matrix is stored in memory and the solution time for iterative methods is $O(N^{3/2})$ or even $O(N \log N)$ for the so-called multilevel FMM. The FMM does not perform well in cases where the structure is at most on the order of the wavelength, but geometrical features require a large number of elements. The plane-wave FMM solves this problem, but is more complex [189]. The FMM is based on a representation of the Green function and thus not very versatile. Another method, called the adaptive cross-approximation (ACA) [190], is based purely on the linear algebraic properties of the system matrix, which are produced by method of moments approximations of integral equations with asymptotically smooth kernel. The matrix Z is ordered so that spatially nearby elements correspond to matrix elements, which have indices of similar magnitude (a so-called cluster tree is constructed). Then it can be shown that the matrix consists of blocks that can be approximated by very low rank matrices and the rank does not significantly increase when the dimension of Z increases. The singular value decomposition would yield the best low-rank approximants, but it is more time consuming to construct than the use of direct solution methods. The ACA essentially deals with finding such low-rank approximants with small computational cost and low memory requirements. The method can yield $O(N)$ solution time complexity. Scattering problems have kernels which are not asymptotically smooth, but similar low-rank structure exists and ACA has been successfully applied to wave scattering with complexity $O(N^{4/3} \log N)$. [191] The drawback as compared to FMM is that rigorous error estimates for the low-rank approximations are difficult to obtain.

In this work the problems were small enough that full matrix storage and LU-decomposition based solver were practical. Implementing FMM and ACA effectively requires careful software engineering, so that the use of existing solutions is highly recommended. For FMM, it is difficult to write widely usable implementations due to the kernel-dependency. For ACA there is, e.g., the AHMED C++ library, written by M. Bebendorf, that could be used in various BEM codes.

The MOM solution for the second-harmonic fields uses the same finite-dimensional approximations of the integral operators, but at the second-harmonic frequency. The major difference with respect to the linear problem is that there are no incident fields, but the surface polarization acts as the excitation and now the equivalent surface current

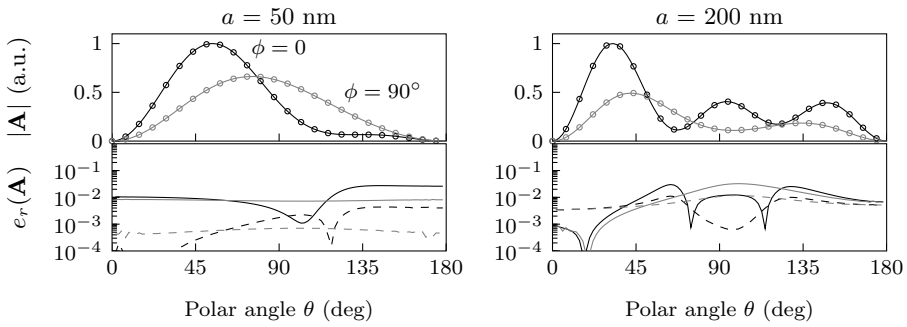

Figure 5.5: Second-harmonic scattering amplitudes from gold spheres of radii 50 nm and 200 nm. Upper plots show normalized scattering amplitudes $\mathbf{A}$ (solid line is multipole solution, markers are BEM solutions). Lower plots show relative errors $e_r(\mathbf{A})$ of BEM calculations using different meshes (solid lines: 1280 triangles, dashed lines: 5120 triangles). Two azimuthal directions are plotted for each case (black: $\phi = 0$, gray: $\phi = 90°$).

densities are discontinuous over the material interfaces according to Eqs. (3.59) and (3.60). In the first approach presented in **Paper I**, one solves for $\mathbf{J}_l^{\mathrm{s}}$ and $\mathbf{M}_l^{\mathrm{s}}$ in each domain and Eqs. (3.59) and (3.60) are tested. The dimension of Z is then $4N_e$ and thus the matrix storage is 4 times the linear problem storage.

The second method, utilized in **Paper III**, is to first expand the jumps in $\gamma_t\mathbf{E}$ and $\gamma_t\mathbf{H}$ in the RWG basis:

$$-i\omega\mathcal{P}_{\mathrm{t}}^l = \sum_{n=1}^{N_l} \gamma_n^l \mathbf{f}_n^l, \qquad \frac{1}{\epsilon'}\gamma_{rl}\nabla_t\mathcal{P}_{\mathrm{n}}^l = \sum_{n=1}^{N_l} \delta_n^l \mathbf{f}_n^l, \tag{5.32}$$

where the expansion coefficients are arranged into vectors $\boldsymbol{\gamma}_l = \{\gamma_1^l, \ldots, \gamma_{N_l}^l\}$ and $\boldsymbol{\delta}_l = \{\delta_1^l, \ldots, \delta_{N_l}^l\}$ and are solved from

$$(\mathrm{F}_l\boldsymbol{\gamma}_l)_m = i\omega \left\langle \mathbf{f}_m^l, \mathcal{P}_{\mathrm{t}}^l \right\rangle, \tag{5.33}$$

$$(\mathrm{F}_l\boldsymbol{\delta}_l)_m = \frac{1}{\epsilon'} \left\langle \mathbf{f}_m^l, \gamma_{rl}\nabla_t\mathcal{P}_{\mathrm{n}}^l \right\rangle, \tag{5.34}$$

where $(\mathrm{F}_l)_{mn} = \left\langle \mathbf{f}_m^l, \mathbf{f}_n^l \right\rangle$. Now one can choose to solve only one electric and one magnetic equivalent surface current density per interface the same way as in the linear scattering problem, only now the source vector elements become

$$(b_l)_m = -\alpha\frac{1}{\epsilon'} \left\langle \nabla_t' \cdot \mathbf{f}_m^l, \mathcal{P}_n^l \right\rangle - (\mathrm{D}_l\boldsymbol{\gamma}_l - \mathrm{K}_l\boldsymbol{\delta}_l)_m, \tag{5.35}$$

$$(b_l)_{N_l+m} = -i\omega\alpha \left\langle \mathbf{f}_m^l, \gamma_{rl}\mathcal{P}_{\mathrm{t}}^l \right\rangle - (\mathrm{K}_l\boldsymbol{\gamma}_l + \mathrm{D}_l\boldsymbol{\delta}_l/\eta_l^2)_m. \tag{5.36}$$

The expansion (5.33) is not expected to be exact, because the RWG functions are first order in one dimension and zeroth order in the second, whereas $\mathcal{P}_{\mathrm{t}}^l$ can be second order. Tests have shown that this can nevertheless be a good approximation in practice. Care must be taken in the evaluation of Eq. (5.34), because $\nabla_t\mathcal{P}_{\mathrm{n}}^l$ is only defined in the sense of distributions and partial integration is not directly applicable due to the trace γ_{rl}. One technique to overcome this problem is to first project $\nabla_t\mathcal{P}_{\mathrm{n}}^l$ to RWG basis, which is well-defined. Then the evaluation of (5.34) is also well-defined and results in good accuracy.

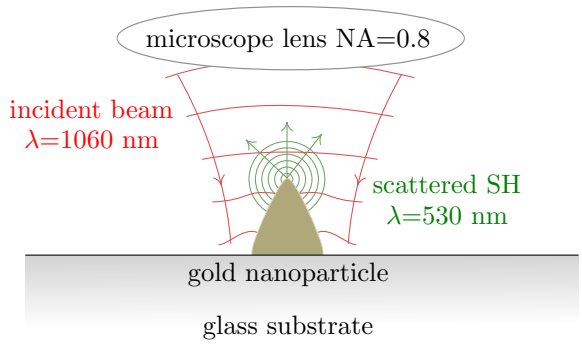

Figure 5.6: Schematic of beam scanning experiment.

Figure 5.5 illustrates the accuracy of the BEM. Second-harmonic scattering amplitudes $\mathbf{A}$ and their relative errors $e_r(\mathbf{A})$ are plotted for gold spheres of radii 50 nm and 200 nm, which are illuminated at fundamental wavelength 1060 nm by a plane-wave that propagates along the z-axis and is linearly polarized along the x-axis. Two different triangular patch meshes are considered. When calculating the matrix elements, two-term singularity subtraction was used and 4-point Gauss-Legendre quadrature used for the remaining integral. Sub one percent relative error is achieved for most scattering directions even with the sparser mesh.

A very specialized procedure was developed in **Paper IV** for the modeling of a microscopy experiment illustrated in Fig. 5.6. Here a tightly focused Gaussian beam is scanned over a nanoparticle and SHG is measured in reflection and collected over the whole aperture of the focusing lens. It may appear problematic to model this experiment, as one has to solve the second-harmonic scattering problem for all positions of the beam. However, the following procedure was used: (1) Construct the system matrix Z_1 for the fundamental fields. (2) Factorize $\mathrm{Z}_1 = \mathrm{P}_1\mathrm{L}_1\mathrm{U}_1$ by the partially pivoted LU-decomposition. (3) Compute the source vectors $\mathbf{b}_1^i$ for all beam positions i. (4) Find the solution vectors $\mathbf{x}_1^i$ by direct substitution. (5) Construct the system matrix $\mathbf{Z}_2$ for the second-harmonic problem and store the blocks D_l and K_l. (6) Factorize $\mathrm{Z}_2 = \mathrm{P}_2\mathrm{L}_2\mathrm{U}_2$. (7) Calculate source vectors $\mathbf{b}_2^i$ for each $\mathbf{x}_1^i$ and make use of the stored block matrices in Eqs. (5.35) and (5.36).

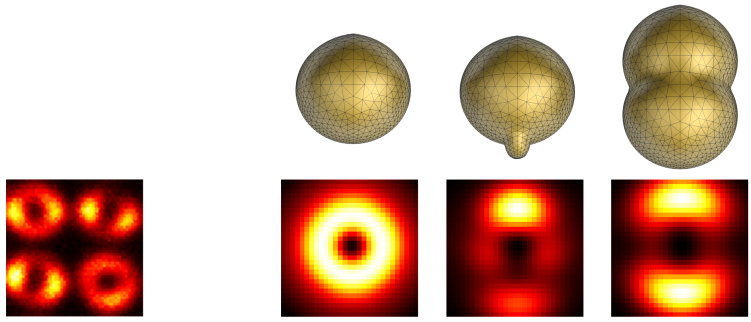

Figure 5.7: Second-harmonic microscope images of gold nanobumps using radially polarized focused beams. Leftmost: measured result over four particles. Right: simulated results using ideal shape and two defected shapes.

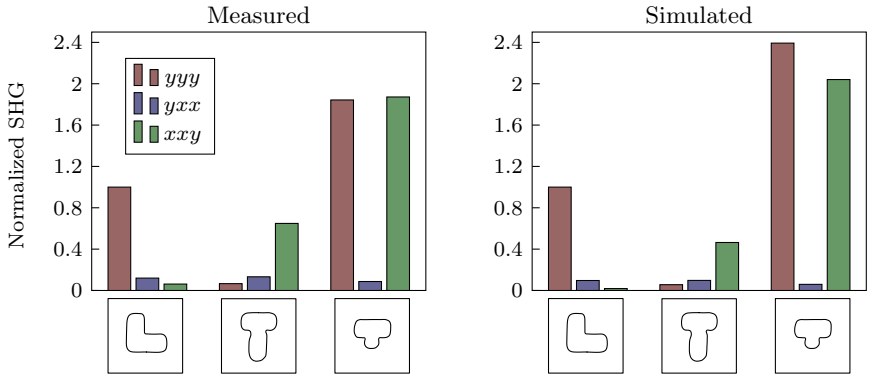

Figure 5.8: SHG from arrays of gold nanoparticles in different polarization configurations. The results are normalized to *yyy* component of L.

(8) Solve for $\mathbf{x}_2^i$ by direct substitution. The most time consuming tasks are (1), (2), (5) and (6), but they are independent of the beam position and thus only computed once. All other steps have at most $O(N^2)$ complexity and consist of fairly simple operations. The procedure was also implemented to utilize isometric symmetries via the irreducible group representations. It is then necessary to store and factorize the system matrices for each representation and to project each beam into the symmetric constituents.

Some of the results of **Paper IV** are shown in Fig. 5.7. It turned out that radially polarized focused beams combined with SHG are very effective in determining if a particle has defects. Modeling the SHG response from different type of defected particles can be used to estimate the type of defects in the real sample.

In **Paper V**, BEM was also utilized to model SHG from arrays of L- and T-shaped gold nanoparticles. At normal incidence, the detected second-harmonic field components $E_i(2\omega)$ can be related to the incident field components $E_i^{\text{inc}}(\omega)$ via the nonlinear response tensor A by

$$E_i(2\omega) = \sum_{j,k\in\{x,y,z\}} \mathrm{A}_{ijk} E_j^{\text{inc}}(\omega) E_k^{\text{inc}}(\omega), \;\; i = x, y, z. \tag{5.37}$$

Three absolute squares of three tensor components of A were measured at fundamental wavelength 1060 nm. We denote these quantities simply by yyy, yxx and xxy. Simulations were done with BEM using the same structures as was shown in Fig. 5.4. Both measured and simulated results are shown in Fig. 5.8. The agreement is very good, considering that the quantities are squares of results obtained from a nonlinear model.

6 Symmetry

Many objects and phenomena that occur in nature display symmetry of some kind. In mathematics, symmetry is very concisely defined in terms of the group structure and group action. This Chapter considers the symmetry under a finite group of isometric diffeomorphisms and reviews its implications for electric and magnetic fields. We then apply these concepts to derive symmetry predicates for the equivalent surface current densities. We show that these results can be utilized in BEM to decrease the computational cost of solving linear and second-order nonlinear scattering problems in the undepleted-pump approximation. It is often the case that the media are symmetrical, but the excitation and consequently the solution are not. By the use of group representation theory, only the media, not excitations, need to be symmetrical in order to exploit the symmetry. Finally, we show that the modes discussed in Chapter 4 have symmetry that matches the geometric symmetry.

6.1 Group theory and representations

A *group* $\mathfrak{G}$ is a set equipped with a binary operation $\cdot : \mathfrak{G} \times \mathfrak{G} \to \mathfrak{G}$ that satisfies the group axioms[192]: 1) For all $a, b \in \mathfrak{G}$, $a \cdot b \in \mathfrak{G}$. 2) For all $a, b, c \in \mathfrak{G}$, $(a \cdot b) \cdot c = a \cdot (b \cdot c)$. 3) There exists an element $e \in \mathfrak{G}$ (*identity*) such that $e \cdot a = a \cdot e = a$ holds for all $a \in \mathfrak{G}$. 4) For each $a \in \mathfrak{G}$ there exists $b \in \mathfrak{G}$ such that $a \cdot b = b \cdot a = e$. Then b is called the *inverse* of a and denoted by a^{-1}. If $a \cdot b = b \cdot a$ for all $a, b \in \mathfrak{G}$, the group is *commutative* (or *Abelian*). The number of elements $n_{\mathfrak{G}}$ in a finite group $\mathfrak{G}$ is called the *order of the group*. For element $a \in \mathfrak{G}$, if there exists $n_a \in \mathbb{N}$ so that $a^{n_a} = e$, then n_a is the *order of the element*. A cyclic group is one whose elements are generated by powers of a single element (called the generating element). A simple geometrical symmetry is mirror with respect to a plane, which is represented by a group $\{e, \sigma\}$, where σ is the mirror operation. This group is clearly Abelian. The rotations of the Rubik's cube of three rows constitute a non-Abelian group of order exceeding 43 quintillion (10^{18}).

Abstract groups are often difficult to work with. That's why it may be useful to identify the group as something that we know how to work with. This is achieved with so-called *linear representation* of a group. In this work, such representations are used to systematically synthesize non-symmetrical solutions from their symmetrical projections. A linear representation of a group $\mathfrak{G}$ on a finite-dimensional vector space V is a group homomorphism $f : \mathfrak{G} \to GL(V)$, where $GL(V)$ is the group of all automorphisms of V.[192] In this work, we assume that the scalar field of V is $\mathbb{C}$. With such a representation, we can work with invertible matrices that represent the elements of $\mathfrak{G}$ and the binary operation is the matrix multiplication. A *subrepresentation* is the restriction of f on a subspace $W \subset V$, i.e. a mapping $\mathfrak{G} \to GL(W)$, such that $gw \in W$ for all g in the image of f and all $w \in W$. A representation is *irreducible*, if it only has the subrepresentations over V and $\{0\}$ (trivial).

Two representations $f_1 : \mathfrak{G} \to GL(V)$ and $f_2 : \mathfrak{G} \to GL(W)$ are *equivalent*, if there exists a vector space isomorphism $\iota : V \to W$ so that $\iota \circ f_1(g) \circ \iota^{-1} = f_2(g)$ holds for all $g \in \mathfrak{G}$. Finding the nonequivalent irreducible representations of an abstract group is a central problem in group theory. An Abelian group of order $n_{\mathfrak{G}}$ has exactly $n_{\mathfrak{G}}$ nonequivalent irreducible representations, which are complex scalars. For the rotation group C_N, the image of the mth irreducible representation is $\{\exp(i2\pi nm/N)|n = 1, 2, \ldots, N\}$.

6.2 Symmetry predicates in electromagnetic theory

We associate an abstract group to describe the symmetry of both geometry and fields. The mappings of points must be such that they preserve the analytical properties of the fields and constitute a finite group. For this purpose, we invoke the group action, which associates a diffeomorphic mapping $p_g : V \to V$ of points in $V \subset \mathbb{R}^3$ for each $g \in \mathfrak{G}$. The mappings p_g constitute a group under composition. An action is *effective*, if for all $g \in \mathfrak{G}, g \neq e$ there exists $\mathbf{r} \in V$ such that $p_g(\mathbf{r}) \neq \mathbf{r}$. We require the actions to be effective, implying that $\mathfrak{G}$ and $\{p_g|g \in \mathfrak{G}\}$ are isomorphic. Furthermore, the mappings p_g are required to be isometric for simplicity.

We say that a domain $V \subset \mathbb{R}^3$ is $\mathfrak{G}$-symmetrical, if $p_g(V) = V$ for all $g \in \mathfrak{G}$. For our boundary integral formulation, it is essential to note that the boundary ∂V of a $\mathfrak{G}$-symmetrical V is also $\mathfrak{G}$-symmetrical. To take advantage of such symmetry, the task is to recognize the symmetry cell $\Gamma \subset \partial V$ of smallest area and the group $\mathfrak{G}$ of highest order such that $\partial V = \cup_{g\in\mathfrak{G}} p_g(\Gamma)$.

The overwhelmingly popular notion of electromagnetic quantities is based on the Ricci calculus, where physical laws are expressed in coordinates, but are required to hold in any set of coordinates. The notion of the electric field $\mathbf{E}$ as a mapping $\mathbb{R}^3 \to \mathbb{C}^3$ does not by itself contain sufficient information of how the field transforms under such change of coordinates. A notion of "polar vector" must be implicitly associated with the definition of $\mathbf{E}$, meaning that it covaries with change of coordinates. On the other hand, the magnetic field $\mathbf{H}$ covaries, except under improper change of coordinates, where a sign difference occurs, thus the magnetic field is labelled "an axial vector".

These notions can be understood by recognizing that $\mathbf{E}$ appears in the integral form of Faraday's law in a contour integration $\int_C \mathbf{E} \cdot \mathbf{t} dC$, where $\mathbf{t}$ is tangent to a curve C. The product $\mathbf{E} \cdot \mathbf{t}$ is a measure of virtual work that $\mathbf{E}$ does on a test charge. Let $\mathbf{c} : \mathbb{R} \to \mathbb{R}^3$ be some differentiable parametrized curve. The group action induces an image curve $p_g \circ \mathbf{c}$ for each $g \in \mathfrak{G}$. Tangent vectors then map as $\mathrm{J}_g\mathbf{c}'$, where J_g is the Jacobian matrix of p_g. The Jacobians are group actions for the tangent vectors and are orthogonal matrices due to p_g being required isometric. The $\mathbf{E}$-field is $\mathfrak{G}$-symmetrical, if $\mathbf{E}(\mathbf{c}(t)) \cdot \mathbf{c}'(t) = \mathbf{E}(p_g(\mathbf{c}(t))) \cdot \mathrm{J}_g\mathbf{c}'(t)$ for all $g \in \mathfrak{G}$ and all $\mathbf{c} : \mathbb{R} \to \mathbb{R}^3$. The transformation of $\mathbf{E}$ thus follows directly from the group action. However, the time-harmonic Maxwell equations also allow a phase-shift to occur under such group actions. Thus we introduce another action that is a multiplication by a constant $h_g \in \mathbb{C}$ for $g \in \mathfrak{G}$ so that $|h_g| = 1$. This action is not required to be effective. The $\mathbf{E}$-field is then called $(\mathfrak{G}, h)$-symmetrical, if it satisfies the predicate

$$\mathrm{J}_g^T O_g \mathbf{E} = h_g \mathbf{E}, \qquad \forall g \in \mathfrak{G}, \tag{6.1}$$

where $O_g\mathbf{E}(\mathbf{r}) = \mathbf{E}(p_g(\mathbf{r}))\ \forall g \in \mathfrak{G}, \forall \mathbf{r} \in \mathbb{R}^3$. The Maxwell equations with Eq. (6.1) imply that the magnetic field must satisfy $\mathrm{J}_g^T O_g \mathbf{H} = h_g |\mathrm{J}_g| \mathbf{H},\ \forall g \in \mathfrak{G}$, where $|\mathrm{J}_g|$ is the determinant of the Jacobian that can only be ± 1. The case $|\mathrm{J}_g| = -1$ corresponds

to change of orientation of the tangent space, which is often referred to as "improper" symmetry.

In the analysis of the symmetry of the Stratton-Chu boundary integral operators, it is necessary to know how the equivalent surface current densities $\mathbf{J}^{\mathrm{s}}$ and $\mathbf{M}^{\mathrm{s}}$ and their surface divergences transform. It follows from the Maxwell equations that $\nabla_t \cdot \mathbf{J}^{\mathrm{s}} = i\omega\epsilon \mathbf{n} \cdot \mathbf{E}$ and $\nabla_t \cdot \mathbf{M}^{\mathrm{s}} = i\omega\mu \mathbf{n} \cdot \mathbf{H}$. Then[§]

$$\begin{aligned}(\nabla_t \cdot \mathbf{J}^{\mathrm{s}})(p_g(\mathbf{r})) &= i\omega\epsilon \mathbf{n}(p_g(\mathbf{r})) \cdot \mathbf{E}(p_g(\mathbf{r})) = i\omega\epsilon(\mathrm{J}_g \mathbf{n}(\mathbf{r})) \cdot (h_g \mathrm{J}_g \mathbf{E}(\mathbf{r})) \\ &= i\omega\epsilon h_g \mathbf{n}(\mathbf{r}) \cdot \mathbf{E}(\mathbf{r}) = h_g(\nabla_t \cdot \mathbf{J}^{\mathrm{s}})(\mathbf{r}).\end{aligned} \tag{6.2}$$

Similar analysis can be carried out for $\nabla_t \cdot \mathbf{M}^{\mathrm{s}}$, thus we obtain

$$O_g \nabla_t \cdot \mathbf{J}^{\mathrm{s}} = h_g \mathbf{J}^{\mathrm{s}}, \tag{6.3}$$

$$O_g \nabla_t \cdot \mathbf{M}^{\mathrm{s}} = h_g |\mathrm{J}_g| \mathbf{M}^{\mathrm{s}}. \tag{6.4}$$

From the definition of the equivalent surface current densities

$$\mathbf{J}^{\mathrm{s}}(p_g(\mathbf{r})) = \mathbf{n}(p_g(\mathbf{r})) \times \mathbf{H}(p_g(\mathbf{r})) = (\mathrm{J}_g \mathbf{n}(\mathbf{r})) \times (h_g |\mathrm{J}_g| \mathrm{J}_g \mathbf{H}(\mathbf{r})) \tag{6.5}$$

$$= h_g \mathrm{J}_g \mathbf{J}^{\mathrm{s}}(\mathbf{r}). \tag{6.6}$$

Similar analysis applies to $\mathbf{M}^{\mathrm{s}}$ yielding

$$O_g \mathbf{J}^{\mathrm{s}} = h_g \mathrm{J}_g \mathbf{J}^{\mathrm{s}}, \tag{6.7}$$

$$O_g \mathbf{M}^{\mathrm{s}} = h_g |\mathrm{J}_g| \mathrm{J}_g \mathbf{M}^{\mathrm{s}}. \tag{6.8}$$

Here we obtained the symmetry predicates for the various electromagnetic quantities by utilizing the various results for orthogonal matrices in dot and cross products. We note in passing that the formulation of electromagnetic theory via differential forms over differentiable manifolds with boundary has some unique commutation properties that are especially convenient for the study of symmetries[193]. In this formalism, the electric and magnetic fields are 1-forms while the corresponding flux-densities are 2-forms. These can be defined in an abstract notion of a differentiable Manifold as a topological space, hence no notion of metric nor coordinates is required. The symmetry predicates can then be analyzed via the commutation properties of pull-backs (induced by the group action), exterior derivative and trace[63]. The determinant of the Jacobian, that arises in the classical vector analysis, is embedded in the Hodge star operator, which depends on metric and arises in the constitutive relation between the 1-forms and 2-forms.

In practice, the excitation of the scattering problem may not have a well-defined symmetry even if the geometry does. However, in the case of linear media (or in the undepleted-pump approximation of SHG) we may utilize the non-equivalent irreducible group representations to project the excitation and the corresponding solution into symmetrical constituents that reside in orthogonal sub-spaces of $\mathbb{L}^2(S)$. This is achieved with a projection operator

$$\mathscr{P}_n = \frac{1}{n_{\mathfrak{G}}} \sum_{g \in \mathfrak{G}} (\rho_g^n)^* \mathrm{J}_g O_g^{-1}, \ n = 1, 2, \ldots, n_{\mathfrak{G}}, \tag{6.9}$$

which is idempotent and its range and null-space are orthogonal subspaces with respect to the $\mathbb{L}^2$ inner-product[194]. The complex numbers ρ_g^n constitute the irreducible representations. A symmetric constituent of the linear scattering problem is then calculated

[§]Useful identities: $(\mathrm{A}\mathbf{x}) \cdot (\mathrm{A}\mathbf{y}) = \mathbf{x} \cdot \mathbf{y}$ and $(\mathrm{A}\mathbf{x}) \times (\mathrm{A}\mathbf{y}) = \mathrm{A}|\mathrm{A}|(\mathbf{x} \times \mathbf{y})$ for orthogonal matrix A and vectors $\mathbf{x}, \mathbf{y}$.

as $\mathbf{E}^{(n)}_{\text{inc}} = \mathscr{P}_n \mathbf{E}_{\text{inc}}$, which then yields symmetrical solution $\mathbf{E}^{(n)}$. The solution to the problem with incident field $\mathbf{E}_{\text{inc}}$ is then obtained via summation $\mathbf{E} = \sum_n \mathbf{E}^{(n)}$. Similar approach can be used for the surface SHG problem, where the operator $\mathscr{P}_n$ is applied to the surface source.

6.3 Application to boundary integral operators

Consider the scattering problem as defined in Section 3.6. In case the boundary ∂V of a scatterer is generated by the actions p_g from symmetry cell $\Gamma \subset \partial V$ and we know the symmetry predicates of $\mathbf{J}^{\text{s}}$ and $\mathbf{M}^{\text{s}}$, we may write an integral operator as

$$\int_{\partial V} G(\mathbf{r}, \mathbf{r}') \mathbf{J}^{\text{s}}(\mathbf{r}) dS' = \sum_{g \in \mathfrak{G}} h_g \int_{\Gamma} G(\mathbf{r}, p_g(\mathbf{r}')) \mathrm{J}_g \mathbf{J}^{\text{s}}|_{\Gamma}(\mathbf{r}) dS', \tag{6.10}$$

where only the restriction of $\mathbf{J}^{\text{s}}$ over Γ is required. Similar construction is possible for the other type of integral operators. In the MOM scheme the system matrix corresponding to a particular domain is then expressed in the form

$$\mathrm{Z} = \sum_{g \in \mathfrak{G}} h_g \mathrm{Z}_g, \tag{6.11}$$

where matrices Z_g consist of the weak forms of operators of the form (6.10) and the testing is performed over Γ only. The above procedure was utilized in **Paper III**, where linear and surface second-harmonic scattering problems were described with the PMCHWT formulation of BEM that utilizes $\mathfrak{G}$-symmetry.

Because the matrices Z_g are independent of the group representation, significant savings in memory, matrix assembly time and linear system solution time can be achieved: If the moment matrix of Eq. (6.10) has N^2 elements, then the utilization of symmetry leads to a moment matrix with $(N/n_{\mathfrak{G}})^2$ elements. Because we need to sum over all $g \in \mathfrak{G}$ in Eq. (6.10), the matrix assembly time is only divided by $n_{\mathfrak{G}}$. The solution time complexity of direct solvers is $O(N^3)$. Thus solution time can at best be lowered by a factor $n^3_{\mathfrak{G}}$. In **Paper III**, the memory and time scalings are discussed in more detail for the PMCHWT formulation.

In case the contour boundary $\partial\Gamma$ is not empty, boundary conditions arise for the equivalent surface current densities. These follow directly from the symmetry predicates applied to the *fixed points* of the group actions, i.e., for points $\mathbf{r} \in \partial\Gamma$ for which $p_g(\mathbf{r}) = \mathbf{r}$ holds for some non-identity $g \in \mathfrak{G}$. For rotationally symmetrical geometry, boundary conditions also arise via points $\mathbf{r} \in \partial\Gamma$ for which $p_g(\mathbf{r}) \in \partial\Gamma$ for some non-identity $g \in \mathfrak{G}$. These boundary conditions are imposed by removing and/or combining the rows and columns of the system matrix according to the properties of the basis functions. The RWG functions are specially convenient in this respect, because their normal-to-edge vector components are constant over edges and the boundary conditions can be enforced via such components.

6.4 Symmetry of eigenmodes

The calculations in **Paper II** revealed that the modes defined by Eq. (4.20) appear to be in some sense symmetrical, which leads to a search of general symmetry constraints for the modes.

Let us have two operators $\mathscr{A}, \mathscr{B} : A \to A$ over a separable Hilbert space A. Let's further assume that they commute, i.e., $\mathscr{A}\mathscr{B} = \mathscr{B}\mathscr{A}$. If $x \in A$ is an eigenfunction of $\mathscr{A}$ with the eigenvalue a, that is, $\mathscr{A}x = ax$, then

$$\mathscr{B}\mathscr{A}x = a\mathscr{B}x \Rightarrow \mathscr{A}\mathscr{B}x = a\mathscr{B}x, \tag{6.12}$$

which means that $\mathscr{B}x$ is an eigenfunction of $\mathscr{A}$ with eigenvalue a. If a is non-degenerate, then $\mathscr{B}x = bx$ for some scalar b. Then x is also an eigenfunction of $\mathscr{B}$. We only consider the case of non-degenerate eigenvalues here.

Consider now that operator $\mathscr{A}$ is the Müller integral operator and $\mathbf{f}_n$ is its eigenfunction with eigenvalue λ_n as in Eq. (4.20). Define $\mathscr{B}$ as the symmetry operator

$$\mathscr{B} = \begin{pmatrix} \mathrm{J}_g^T O_g & 0 \\ 0 & |\mathrm{J}_g| \mathrm{J}_g^T O_g \end{pmatrix} \tag{6.13}$$

related to some group element $g \in \mathfrak{G}$. If a solution $\mathbf{f}$ is symmetrical as defined in the preceding sections, it is an eigenfunction of $\mathscr{B}$ with eigenvalue h_g with $|h_g| = 1$. To show that the eigenmodes $\mathbf{f}_n$ are symmetrical in this sense, we must show that $\mathscr{A}$ and $\mathscr{B}$ commute. Commutation of $\mathscr{B}$ with the identity operator, which appears in the Müller formulation, is trivial.

Denote the operator matrix elements of $\mathscr{A}$ by $\mathscr{A}_{ij}$ where $i, j = 1, 2$ and let $\mathscr{B}_{11} = \mathrm{J}_g^T O_g$ and $\beta = |\mathrm{J}_g| = |\mathrm{J}_g^T|$. We assume that positions $\mathbf{r} \in \mathbb{R}^3$ are position vectors with respect to such origin that $p_g = \mathrm{J}_g$ holds. For brevity, we consider explicitly only one of the operators in $\mathscr{A}_{ij}$:

$$\begin{aligned}
(\mathscr{B}_{11}\mathbf{n} \times \mathscr{K}\mathbf{f})(\mathbf{r}) &= \mathrm{J}_g^T \left[\mathbf{n}(p_g(\mathbf{r})) \times \int_S (\nabla' G)(p_g(\mathbf{r}), \mathbf{r}') \times \mathbf{f}(\mathbf{r}') dS' \right] \\
&= \beta \mathbf{n}(\mathbf{r}) \times \int_S \mathrm{J}_g^T [(\nabla' G)(p_g(\mathbf{r}), \mathbf{r}') \times \mathbf{f}(\mathbf{r}')] dS' \\
&= \beta^2 \mathbf{n}(\mathbf{r}) \times \int_S (\mathrm{J}_g^T \nabla' G)(p_g(\mathbf{r}), \mathbf{r}') \times [\mathrm{J}_g^T \mathbf{f}(\mathbf{r}')] dS' \\
&= \mathbf{n}(\mathbf{r}) \times \int_S (\nabla'' G)(\mathbf{r}, \mathbf{r}'') \times [\mathrm{J}_g^T \mathbf{f}(p_g(\mathbf{r}''))] dS'' \\
&= (\mathbf{n} \times \mathscr{K}\mathscr{B}_{11}\mathbf{f})(\mathbf{r})
\end{aligned} \tag{6.14}$$

where we used $\beta^2 = 1$, $(\mathrm{J}_g^T \nabla' G)(p_g(\mathbf{r}), \mathbf{r}') = (\nabla' G)(\mathbf{r}, p_g^{-1}(\mathbf{r}'))$ and defined $\mathbf{r}'' = p_g^{-1}(\mathbf{r}')$. Similar procedure yields $\mathscr{B}_{11}\mathbf{n} \times \mathscr{D} = \beta \mathbf{n} \times \mathscr{D}\mathscr{B}_{11}$. Thus we obtain the following commutation relations:

$$\mathscr{A}_{11}\mathscr{B}_{11} = \mathscr{B}_{11}\mathscr{A}_{11}, \qquad \mathscr{A}_{12}\mathscr{B}_{11} = \beta\mathscr{B}_{11}\mathscr{A}_{12}, \tag{6.15}$$

$$\mathscr{A}_{21}\mathscr{B}_{11} = \beta\mathscr{B}_{11}\mathscr{A}_{21}, \qquad \mathscr{A}_{22}\mathscr{B}_{11} = \mathscr{B}_{11}\mathscr{A}_{22}. \tag{6.16}$$

It then follows by direct calculation that $\mathscr{A}$ and $\mathscr{B}$ do commute, completing the proof that the non-degenerate modes have a well-defined symmetry that matches the geometric symmetry.

7 Discussion and outlook

In this work, boundary integral approaches were developed for the modeling of linear and nonlinear optical properties of single nanoparticles and particle arrays. The work aimed at two closely interrelated goals: (1) The boundary element method for modeling of surface SHG, which was shown to be accurate and versatile by comparison to known reference solutions and measured results. (2) The use of boundary integral operators to define plasmon resonances and modes as intrinsic properties of scatterers. We demonstrated that these quantities can be discovered without the specification of probe excitations in contrast to the prevailing *modus operandi* of the nano-optics community.

The reliable modeling of the optical response of plasmonic nanoparticles has become increasingly important in nano-optics. The boundary element method has been found suitable for modeling the linear response of resonant scattering, which motivated the effort of extending BEM to model nonlinear optical responses. We developed BEM for the modeling of surface SHG from isolated nanoparticles of arbitrary shape and a corresponding full-wave semi-analytical multipole solution for spherical particles. The comparison showed that the BEM approach can yield sub one percent relative errors for second-harmonic far-fields. After publication of the work, the method gained immediate popularity in the modeling of several nano-optical systems: the detection of trapping of metal particles[195], nonlinear plasmonic nanorulers[196], ultrasensitive optical shape characterization of nanoantennas[197], augmentation of SHG by the use of Fano resonances[198] and SHG from coupled nanosphere systems[199]. The method was revisited and extended for the modeling of bulk SHG from higher multipolar responses in Ref. 200 and it was extended for periodic structures in Ref. 201 by other research groups.

Because nanoparticles often posses some geometrical symmetry and the memory requirement of BEM scales quadratically with respect to the number of unknowns, it was realized that the symmetry should be utilized in the method. We used the group representation theory to exploit isometric symmetries, described by finite Abelian groups, in both linear and surface second-harmonic boundary integral formulations. The method was shown to yield significant computational benefits and enable the study of large but highly symmetrical particles. The method was applied to the study of multiply-split gold ring-resonators, which had been priorly studied experimentally.

The developed method was utilized to model the nonlinear microscopy of gold nanodots and nanocones, while the microscopy experiments were carried out by the Author's colleagues. The model of the experiment was rather complex, because linearly, azimuthally and radially polarized Gaussian beams were used as excitations and a nonlinear scattering problem had to be solved for each point of the scanning beam. A specialized solution method was developed to solve the problem efficiently. The results showed that the experiments and modeling agreed qualitatively and that small defects in the nanoparticles

can be detected by the combination of SHG and unconventionally polarized beams.

Another experimental work studied SHG from arrays of L- and T-shaped gold nanoparticles. It was shown that exciting a plasmon resonance may not always lead to significant second-harmonic far-field signal. Surprisingly, tuning the polarization of the incident wave off the direction most preferable for the plasmon resonance may lead to increased second-harmonic response. This was explained via BEM calculations by decreased symmetry of the second-harmonic near-fields. The comparison of the linear extinction spectra and second-harmonic signals to experimental results displayed unprecedented agreement, thus also validating the method in practice.

In nano-optics, the Mie theory of spherical scatterers, the quasistatic mode theory and the so-called mode hybridization model have provided intuitive but limited understanding of the optical response of nanoparticles. Often they have been applied beyond their domain of operation in an attempt to understand more complicated systems. We recognized this issue and found a potential remedy in the theory of boundary integral operators of the Fredholm kind. It was shown that the plasmon resonances are isolated poles of the inverse Müller boundary integral operator and any other singularities must arise from the material dispersion or Green's function. A modal expansion was proposed and applied to the study of common nanoparticle shapes. It was also proved that the mode theory is compatible with the Mie theory and the quasistatic theory in the appropriate limits.

This research work has given rise to new theoretical and numerical tools to gain more accurate understanding of the linear and nonlinear optical responses of nanoparticles and metamaterials. However, many issues still remain for future work. Even though it appears that the proposed BEM yields highly accurate far-field response, it was found that the second-harmonic near-field tends to exhibit highly oscillatory behaviour. The reason is not entirely clear, but it could be due to the basis functions lacking the ability to represent the surface gradient of the normal electric field component. A more detailed analysis of the function spaces is therefore needed. Another reason may be that the interface condition model of surface SHG may be energetically plausible only for smooth surfaces.

To model more complicated systems with over 10^4 degrees of freedom, the solver should be coupled with the fast multipole method or the adaptive cross-approximation method. To model the response of multiple but isolated particles, such as in Refs. 24,202,203, a T-matrix approach could be built on top of the BEM solver. Moreover, it's well-known that a silica substrate can red shift plasmon resonances significantly. Unfortunately, the evaluation of the Green function for stratified media is arduous and was not utilized in this work. In the future, it would be essential to be able to utilize this function in order to achieve quantitative predictions.

The mode theory, although demonstrated with practical examples, still presents many challenges. The proposed modal expansion at real frequencies has not been rigorously shown to constitute a Schauder basis of the solution space. Furthermore, the only intuitive property found for the eigenvalues is that $\lambda \approx 0$ signifies a resonance. In contrast, for perfectly conducting scatterers, the corresponding eigenvalues have energetic interpretations[204]. In this Thesis, the SEM was briefly outlined as another possibility for modal expansions, but more work is required to evaluate the importance of the entire function and that of the possible branch cuts due to material dispersion. There are also certain computational challenges to overcome. It is very time consuming to seek for the poles of the system, so more efficient pole search algorithms should be developed. It is also well-known that many MOM implementations of the Müller formulation are not

robust for high permittivity materials, although many improvements have been suggested. This property shows in the highly oscillatory near-fields.

To summarize, the work has led to new advancements in the computational modeling and theoretical understanding of optical response of nanoparticles. The modeling results compared well against reference solutions and measurements, but there is still much room for improvement. Many new ideas have also arisen to be explored. It is expected that the presented developments will expedite the deployment of optical metamaterials and other nanoscopic systems in future technologies and everyday applications.

Bibliography

[1] E. Synge. A suggested model for extending microscopic resolution into the ultra-microscopic region. Philosophical Magazine, **6**, 356 (1928).

[2] L. Novotny and B. Hecht. *Principles of nano-optics* (Cambridge University Press, 2006).

[3] S. A. Maier. *Plasmonics: Fundamentals and applications* (Springer, 2007).

[4] K. L. Kelly, E. Coronado, L. L. Zhao, and G. C. Schatz. The optical properties of metal nanoparticles: the influence of size, shape, and dielectric environment. The Journal of Physical Chemistry B, **107**, 668 (2003).

[5] K. Kneipp, Y. Wang, H. Kneipp, and L. Perelman. Single molecule detection using surface-enhanced Raman scattering (SERS). Physical Review Letters, **78**, 1667 (1997).

[6] V. Shalaev. Optical negative-index metamaterials. Nature Photonics, **1**, 41 (2007).

[7] A. Sihvola. Metamaterials: a personal view. Radioengineering, **18**, 90 (2009).

[8] J. Pendry. Negative refraction makes a perfect lens. Physical Review Letters, **85**, 3966 (2000).

[9] W. Cai, U. K. Chettiar, A. V. Kildishev, and V. M. Shalaev. Optical cloaking with metamaterials. Nature Photonics, **1**, 224 (2007).

[10] V. P. Drachev, V. A. Podolskiy, and A. V. Kildishev. Hyperbolic metamaterials: new physics behind a classical problem. Optics Express, **21**, 15048 (2013).

[11] G. Mie. Beiträge zur optik trüber medien, speziell kolloidaler metallösungen. Annalen der Physik, **25**, 377 (1908).

[12] C. F. Bohren and D. R. Huffman. *Absorption and scattering of light by small particles* (John Wiley & Sons, Inc., New York, 1983).

[13] K. Yee. Numerical solution of initial boundary value problems involving Maxwell's equations in isotropic media. IEEE Transactions on Antennas and Propagation, **14**, 302 (1966).

[14] J.-P. Berenger. Three-dimensional perfectly matched layer for the absorption of electromagnetic waves. Journal of Computational Physics, **127**, 363 (1996).

[15] R. F. Harrington. *Field computation by moment methods* (IEEE Press, 1993).

[16] W. Gibson. *The method of moments in electromagnetics* (Chapman & Hall/CRC, 2007).

[17] S. M. Rao, D. R. Wilton, and A. W. Glisson. Electromagnetic scattering by surfaces of arbitrary shape. IEEE Transactions on Antennas and Propagation, **30**, 409 (1982).

[18] K. Umashankar and A. Taflove. Electromagnetic scattering by arbitrary shaped three-dimensional homogeneous lossy dielectric objects. IEEE Transactions on Antennas and Propagation, **34**, 758 (1986).

[19] L. Greengard and V. Rokhlin. A fast algorithm for particle simulations. Journal of Computational Physics, **73**, 325 (1987).

[20] V. Rokhlin. Rapid solution of integral equations of scattering theory in two dimensions. Journal of Computational Physics, **86**, 414 (1990).

[21] R. Coifman and V. Rokhlin. The fast multipole method for the wave equation: A pedestrian prescription. IEEE Antennas and Propagation Magazine, **35**, 7 (1993).

[22] P. Franken, A. Hill, C. Peters, and G. Weinreich. Generation of optical harmonics. Physical Review Letters, **7**, 118 (1961).

[23] R. W. Boyd. *Nonlinear optics* (Elsevier Academic Press, New York, 2008).

[24] H. Husu, R. Siikanen, J. Mäkitalo, J. Lehtolahti, J. Laukkanen, M. Kuittinen, and M. Kauranen. Metamaterials with tailored nonlinear optical response. Nano Letters, **12**, 673 (2012).

[25] M. Lapine, I. V. Shadrivov, and Y. S. Kivshar. Colloquium: Nonlinear metamaterials. Reviews of Modern Physics, **86**, 1093 (2014).

[26] B. K. Canfield, H. Husu, J. Laukkanen, B. Bai, M. Kuittinen, J. Turunen, and M. Kauranen. Local field asymmetry drives second-harmonic generation in non-centrosymmetric nanodimers. Nano Letters, **7**, 1251 (2007).

[27] B. Canfield, S. Kujala, and K. Jefimovs. Linear and nonlinear optical responses influenced by broken symmetry in an array of gold nanoparticles. Optics Express, **12**, 419 (2004).

[28] S. Link, M. B. Mohamed, and M. A. El-Sayed. Simulation of the optical absorption spectra of gold nanorods as a function of their aspect ratio and the effect of the medium dielectric constant. The Journal of Physical Chemistry B, **103**, 3073 (1999).

[29] J. Kottmann, O. Martin, D. Smith, and S. Schultz. Spectral response of plasmon resonant nanoparticles with a non-regular shape. Optics Express, **6**, 213 (2000).

[30] J. Aizpurua, P. Hanarp, D. Sutherland, M. Käll, G. Bryant, and F. García de Abajo. Optical properties of gold nanorings. Physical Review Letters, **90**, 5 (2003).

[31] S. J. Oldenburg, R. D. Averitt, S. L. Westcott, and N. J. Halas. Nanoengineering of optical resonances. Chemical Physics Letters, **288**, 243 (1998).

[32] C. Rockstuhl, T. Zentgraf, H. Guo, N. Liu, C. Etrich, I. Loa, K. Syassen, J. Kuhl, F. Lederer, and H. Giessen. Resonances of split-ring resonator metamaterials in the near infrared. Applied Physics B, **84**, 219 (2006).

[33] C. Rockstuhl, F. Lederer, C. Etrich, T. Zentgraf, J. Kuhl, and H. Giessen. On the reinterpretation of resonances in split-ring-resonators at normal incidence. Optics Express, **14**, 8827 (2006).

[34] I. Romero, J. Aizpurua, G. W. Bryant, and F. J. García de Abajo. Plasmons in nearly touching metallic nanoparticles: Singular response in the limit of touching dimers. Optics Express, **14**, 9988 (2006).

[35] J. Ye, F. Wen, H. Sobhani, J. B. Lassiter, P. V. Dorpe, P. Nordlander, and N. J. Halas. Plasmonic nanoclusters: Near field properties of the Fano resonance interrogated with SERS. Nano Letters, **12**, 1660 (2012).

[36] S. Zhang, D. a. Genov, Y. Wang, M. Liu, and X. Zhang. Plasmon-induced transparency in metamaterials. Physical Review Letters, **101**, 047401 (2008).

[37] H. Husu, J. Mäkitalo, J. Laukkanen, M. Kuittinen, and M. Kauranen. Particle plasmon resonances in L-shaped gold nanoparticles. Optics Express, **18**, 16601 (2010).

[38] F. J. García de Abajo and A. Howie. Retarded field calculation of electron energy loss in inhomogeneous dielectrics. Physical Review B, **65**, 1 (2002).

[39] U. Hohenester and J. Krenn. Surface plasmon resonances of single and coupled metallic nanoparticles: A boundary integral method approach. Physical Review B, **72**, 195429 (2005).

[40] A. M. Kern and O. J. F. Martin. Surface integral formulation for 3D simulations of plasmonic and high permittivity nanostructures. Journal of the Optical Society of America A, **26**, 732 (2009).

[41] C. Rockstuhl, M. Salt, and H. Herzig. Application of the boundary-element method to the interaction of light with single and coupled metallic nanoparticles. Journal of the Optical Society of America A, **20**, 1969 (2003).

[42] K. Sendur. An integral equation based numerical solution for nanoparticles illuminated with collimated and focused light. Optics Express, **17**, 7419 (2009).

[43] T. Sondergaard. Modeling of plasmonic nanostructures: Green's function integral equation methods. Physica Status Solidi (B), **244**, 3448 (2007).

[44] J. M. Taboada, J. Rivero, F. Obelleiro, M. G. Araújo, and L. Landesa. Method-of-moments formulation for the analysis of plasmonic nano-optical antennas. Journal of the Optical Society of America A, **28**, 1341 (2011).

[45] J. Maxwell. *A treatise on electricity and magnetism* (Macmillan and co., London, 1873).

[46] J. D. Jackson. *Classical electrodynamics* (John Wiley & Sons, Inc., Berkeley, 1999).

[47] T. Maiman. Stimulated optical radiation in ruby. Nature, **187**, 493 (1960).

[48] P. Guyot-Sionnest, W. Chen, and Y. Shen. General considerations on optical second-harmonic generation from surfaces and interfaces. Physical Review B, **33**, 8254 (1986).

[49] T. F. Heinz. Second-order nonlinear optical effects at surfaces and interfaces. In *Nonlinear surface electromagnetic phenomena* (Elsevier, Amsterdam, 1991).

[50] F. X. Wang, F. J. Rodríguez, W. M. Albers, R. Ahorinta, J. E. Sipe, and M. Kauranen. Surface and bulk contributions to the second-order nonlinear optical response of a gold film. Physical Review B, **80**, 4 (2009).

[51] N. Bloembergen, R. Chang, S. Jha, and C. Lee. Optical second-harmonic generation in reflection from media with inversion symmetry. Physical Review, **174**, 813 (1968).

[52] J. Sipe, V. Mizrahi, and G. Stegeman. Fundamental difficulty in the use of second-harmonic generation as a strictly surface probe. Physical Review B, **35**, 9091 (1987).

[53] J. Marsden and M. Hoffman. *Basic complex analysis* (W. H. Freeman, New York, 1999).

[54] V. M. Agranovich and V. L. Ginzburg. *Crystal optics with spatial dispersion and excitons* (Springer, Berlin, 1984).

[55] U. Kreibig and M. Vollmer. *Optical properties of metal clusters* (Springer-Verlag, Berlin, 1995).

[56] R. Esteban, A. G. Borisov, P. Nordlander, and J. Aizpurua. Bridging quantum and classical plasmonics with a quantum-corrected model. Nature Communications, **3**, 825 (2012).

[57] G. A. Wurtz, R. Pollard, W. Hendren, G. P. Wiederrecht, D. J. Gosztola, V. A. Podolskiy, and A. V. Zayats. Designed ultrafast optical nonlinearity in a plasmonic nanorod metamaterial enhanced by nonlocality. Nature Nanotechnology, **6**, 107 (2011).

[58] K. R. Hiremath, L. Zschiedrich, and F. Schmidt. Numerical solution of nonlocal hydrodynamic Drude model for arbitrary shaped nano-plasmonic structures using Nédélec finite elements. Journal of Computational Physics, **231**, 5890 (2012).

[59] H. Raether. *Surface plasmons on smooth and rough surfaces and on gratings* (Springer-Verlag, Berlin, 1988).

[60] I. Mayergoyz, D. Fredkin, and Z. Zhang. Electrostatic (plasmon) resonances in nanoparticles. Physical Review B, **72**, 155412 (2005).

[61] J. Rudnick and E. Stern. Second-harmonic radiation from metal surfaces. Physical Review B, **4**, 4274 (1971).

[62] F. Wang. *Multipolar nonlinear optics of surfaces and bulk materials.* Ph.D. thesis, Tampere University of Technology (2010).

[63] K. Jänich. *Vector analysis* (Springer-Verlag, New York, 2001).

[64] M. O'Searcoid. *Metric spaces* (Springer, 2006).

[65] J. Meixner. The behavior of electromagnetic fields at edges. IEEE Transactions on Antennas and Propagation, **20**, 442 (1972).

[66] A. Buffa, R. Hiptmair, and T. Petersdorff. Boundary element methods for Maxwell transmission problems in Lipschitz domains. Numerische Mathematik, **95**, 459 (2003).

[67] G. Hsiao and R. Kleinman. Mathematical foundations for error estimation in numerical solutions of integral equations in electromagnetics. IEEE Transactions on Antennas and Propagation, **45**, 316 (1997).

[68] D. Colton and R. Kress. *Inverse acoustic and electromagnetic scattering theory* (Springer-Verlag, 1998).

[69] C. Sohl, M. Gustafsson, and G. Kristensson. Physical limitations on broadband scattering by heterogeneous obstacles. Journal of Physics A, **40**, 11165 (2007).

[70] P. M. Morse and H. Feshbach. *Methods of theoretical physics, part I* (Mcgraw-Hill, New York, 1953).

[71] R. Jorgenson and R. Mittra. Efficient calculation of the free-space periodic Green's function. IEEE Transactions on Antennas and Propagation, **38**, 633 (1990).

[72] S. Singh and W. Richards. Accelerating the convergence of series representing the free space periodic Green's function. IEEE Transactions on Antennas and Propagation, **38**, 1958 (1990).

[73] N. Guérin, S. Enoch, and G. Tayeb. Combined method for the computation of the doubly periodic Green's function. Journal of Electromagnetic Waves and Applications, **15**, 205 (2001).

[74] N. Nicorovici, R. McPhedran, and R. Petit. Efficient calculation of the Green's function for electromagnetic scattering by gratings. Physical Review E, **49**, 4563 (1994).

[75] A. Moroz. Exponentially convergent lattice sums. Optics Letters, **26**, 1119 (2001).

[76] A. Mathis and A. Peterson. A comparison of acceleration procedures for the two-dimensional periodic Green's function. IEEE Transactions on Antennas and Propagation, **44**, 567 (1996).

[77] P. P. Ewald. Die berechnung optischer und elektrostatischer gitterpotentiale. Annalen der Physik, **369**, 253 (1921).

[78] K. E. Jordan, G. R. Richter, and P. Sheng. An efficient numerical evaluation of the Green's function for the Helmholtz operator on periodic structures. Journal of Computational Physics, **63**, 222 (1986).

[79] M.-J. Park and S. Nam. Efficient calculation of the Green's function for multilayered planar periodic structures. IEEE Transactions on Antennas and Propagation, **46**, 1582 (1998).

[80] Y. Yu and C. Chan. On the extension of Ewald's method to periodic structures in layered media. Microwave and Optical Technology Letters, **19**, 125 (1998).

[81] D. Wang, E. K. N. Yung, R. S. Chen, D. Z. Ding, and W. C. Tang. On evaluation of the Green function for periodic structures in layered media. IEEE Antennas and Wireless Propagation Letters, **3**, 133 (2004).

[82] C. Linton. The Green's function for the two-dimensional Helmholtz equation in periodic domains. Journal of Engineering Mathematics, **33**, 377 (1998).

[83] V. Papanicolaou. Ewald's method revisited: Rapidly convergent series representations of certain Green's functions. Journal of Computational Analysis and Applications, **1**, 105 (1999).

[84] E. Cohen. Critical distance for grating lobe series. IEEE Transactions on Antennas and Propagation, **39**, 677 (1991).

[85] H. Kurkcu and R. Fernando. Stable and efficient evaluation of periodized Green's functions for the Helmholtz equation at high frequencies. Journal of Computational Physics, **228**, 75 (2009).

[86] G. Valerio, P. Baccarelli, P. Burghignoli, and A. Galli. Comparative analysis of acceleration techniques for 2-D and 3-D Green's functions in periodic structures along one and two directions. IEEE Transactions on Antennas and Propagation, **55**, 1630 (2007).

[87] F. Capolino, D. Wilton, and W. Johnson. Efficient computation of the 3D Green's function for the Helmholtz operator for a linear array of point sources using the Ewald method. Journal of Computational Physics, **223**, 250 (2007).

[88] J. Weideman. Computation of the complex error function. SIAM Journal on Numerical Analysis, **31**, 1497 (1994).

[89] A. Kustepeli and A. Q. Martin. On the splitting parameter in the Ewald method. IEEE Transactions on Microwave and Guided Wave Letters, **10**, 168 (2000).

[90] S. Oroskar, D. R. Jackson, and D. R. Wilton. Efficient computation of the 2D periodic Green's function using the Ewald method. Journal of Computational Physics, **219**, 899 (2006).

[91] K. Michalski and D. Zheng. Electromagnetic scattering and radiation by surfaces of arbitrary shape in layered media, part I: Theory. IEEE Transactions on Antennas and Propagation, **38**, 335 (1990).

[92] M. Paulus, P. Gay-Balmaz, and O. J. F. Martin. Accurate and efficient computation of the Green's tensor for stratified media. Physical Review E, **62**, 5797 (2000).

[93] M. Ayatollahi and S. Safavi-Naeini. A new representation for the Green's function of multilayer media based on plane wave expansion. IEEE Transactions on Antennas and Propagation, **52**, 1548 (2004).

[94] J. C. Chao, F. J. Rizzo, I. Elshafiey, Y. J. Liu, L. Upda, and P. A. Martin. General formulation for light scattering by a dielectric body near a perfectly conducting surface. Journal of the Optical Society of America A, **13**, 338 (1996).

[95] Y. P. Chen, W. E. I. Sha, W. C. H. Choy, L. Jiang, and W. C. Chew. Study on spontaneous emission in complex multilayered plasmonic system via surface integral equation approach with layered medium Green's function. Optics Express, **20**, 20210 (2012).

[96] Y. Chen, W. Chew, and L. Jiang. A new Green's function formulation for modeling homogeneous objects in layered medium. IEEE Transactions on Antennas and Propagation, **60**, 4766 (2012).

[97] W. Chew, J. Xiong, and M. Saville. A matrix-friendly formulation of layered medium Green's function. Antennas and Wireless Propagation Letters, **5**, 490 (2006).

[98] I. Lindell, A. Sihvola, K. Muinonen, and P. Barber. Scattering by a small object close to an interface. I. Exact-image theory formulation. Journal of the Optical Society of America A, **8**, 472 (1991).

[99] K. Michalski and D. Zheng. Electromagnetic scattering and radiation by surfaces of arbitrary shape in layered media, part II: Implementation and results for contiguous half-spaces. IEEE Transactions on Antennas and Propagation, **38**, 345 (1990).

[100] M. Paulus and O. J. F. Martin. Light propagation and scattering in stratified media: a Green's tensor approach. Journal of the Optical Society of America A, **18**, 854 (2001).

[101] E. Simsek, Q. Liu, and B. Wei. Singularity subtraction for evaluation of Green's functions for multilayer media. IEEE Transactions on Microwave Theory and Techniques, **54**, 216 (2006).

[102] Y. Wang, Y. Zhang, M. He, and L. Guo. Calculation of electromagnetic scattering from a two-dimensional target in the vicinity of a plane surface by a hybrid method. Journal of the Optical Society of America. A, **25**, 1232 (2008).

[103] P. Ylä-Oijala and M. Taskinen. Efficient formulation of closed-form Green's functions for general electric and magnetic sources in multilayered media. IEEE Transactions on Antennas and Propagation, **51**, 2106 (2003).

[104] P. Ylä-Oijala, M. Taskinen, and J. Sarvas. Multilayered media Green's functions for MPIE with general electric and magnetic sources by the Hertz potential approach. Progress In Electromagnetics Research, **33**, 141 (2001).

[105] J. Stratton and L. Chu. Diffraction theory of electromagnetic waves. Physical Review, **56**, 99 (1939).

[106] J. Stratton. *Electromagnetic theory* (Mcgraw-Hill College, New York, 1941).

[107] A. Buffa and S. Christiansen. A dual finite element complex on the barycentric refinement. Mathematics of Computation, **76**, 1743 (2007).

[108] R. Wood. Anomalous diffraction gratings. Physical Review, **48**, 928 (1935).

[109] R. Harrington. Boundary integral formulations for homogeneous material bodies. Journal of Electromagnetic Waves and Applications, **3**, 1 (1989).

[110] A. J. Poggio and E. K. Miller. Integral equation solutions of three-dimensional scattering problems. In *Computer techniques for electromagnetics* (Pergamon Press, Oxford, 1973).

[111] Y. Chang and R. Harrington. A surface formulation for characteristic modes of material bodies. IEEE Transactions on Antennas and Propagation, **25**, 789 (1977).

[112] T.-K. Wu and L. L. Tsai. Scattering from arbitrarily-shaped lossy dielectric bodies of revolution. Radio Science, **12**, 709 (1977).

[113] C. Müller. *Foundations of the mathematical theory of electromagnetic waves* (Springer-Verlag, Berlin, 1969).

[114] J. Mautz and R. Harrington. Electromagnetic scattering from a homogeneous body of revolution. Technical report, Syracuse University, New York (1977).

[115] P. Ylä-Oijala, M. Taskinen, and S. Järvenpää. Surface integral equation formulations for solving electromagnetic scattering problems with iterative methods. Radio Science, **40**, 1 (2005).

[116] P. Ylä-Oijala and M. Taskinen. Application of combined field integral equation for electromagnetic scattering by dielectric and composite objects. IEEE Transactions on Antennas and Propagation, **53**, 1168 (2005).

[117] P. Ylä-Oijala, S. Kiminki, K. Cools, F. Andriulli, and S. Järvenpää. Mixed discretization schemes for electromagnetic surface integral equations. International Journal of Numerical Modelling, **25**, 525 (2012).

[118] A. Doicu, T. Wriedt, and Y. Eremin. *Light scattering by systems of particles* (Springer-Verlag, 2006).

[119] C. Forestiere, G. Iadarola, G. Rubinacci, A. Tamburrino, L. Dal Negro, and G. Miano. Surface integral formulations for the design of plasmonic nanostructures. Journal of the Optical Society of America A, **29**, 2314 (2012).

[120] G. W. Hanson and A. B. Yakovlev. *Operator theory for electromagnetics* (Springer-Verlag, New York, 2002).

[121] M. Reed and B. Simon. *Methods of modern mathematical physics I: Functional analysis* (Academic Press, San Diego, 1980).

[122] S. Steinberg. Meromorphic families of compact operators. Archive for Rational Mechanics and Analysis, **31**, 372 (1968).

[123] P. Ylä-Oijala and M. Taskinen. Well-conditioned Müller formulation for electromagnetic scattering by dielectric objects. IEEE Transactions on Antennas and Propagation, **53**, 3316 (2005).

[124] C. E. Baum. On the singularity expansion method for the solution of electromagnetic interaction problems. Interaction Note 88 (1971).

[125] C. E. Baum. On the singularity expansion method for the case of first order poles. Interaction Note 129 (1972).

[126] C. E. Baum. The singularity expansion method. In *Transient electromagnetic fields*, 129 – 179 (Springer, Berlin, 1976).

[127] L. Marin and R. Latham. Analytical properties of the field scattered by a perfectly conducting, finite body. Interaction Note 92 (1972).

[128] L. Marin. Natural-mode representation of transient scattering from rotationally symmetric, perfectly conducting bodies and numerical results for a prolate sphereoid. Interaction Note 119 (1972).

[129] C. E. Baum. Emerging technology for transient and broad-band analysis and synthesis of antennas and scatterers. Proceedings of the IEEE, **64**, 1598 (1976).

[130] D. Giri and F. Tesche. On the use of singularity expansion method for analysis of antennas in conducting media. Electromagnetics, **1**, 455 (1981).

[131] M. Stockman, S. Faleev, and D. Bergman. Localization versus delocalization of surface plasmons in nanosystems: Can one state have both characteristics? Physical Review Letters, **87**, 1 (2001).

[132] D. Fredkin and I. Mayergoyz. Resonant behavior of dielectric objects (electrostatic resonances). Physical Review Letters, **91**, 253902 (2003).

[133] D. E. Gómez, K. C. Vernon, and T. J. Davis. Symmetry effects on the optical coupling between plasmonic nanoparticles with applications to hierarchical structures. Physical Review B, **81**, 1 (2010).

[134] I. Mayergoyz. Plasmon resonances in nanoparticles, their applications to magnetics and relation to the Riemann hypothesis. Physica B, **407**, 1307 (2012).

[135] I. Mayergoyz. *Plasmon resonances in nanoparticles* (World scientific publishing Co. Pte. Ltd., Singapore, 2013).

[136] P. M. Morse and H. Feshbach. *Methods of theoretical physics, part II* (Mcgraw-Hill, New York, 1953).

[137] C. P. Burrows and W. L. Barnes. Large spectral extinction due to overlap of dipolar and quadrupolar plasmonic modes of metallic nanoparticles in arrays. Optics Express, **18**, 3187 (2010).

[138] J. Butet, G. Bachelier, I. Russier-Antoine, C. Jonin, E. Benichou, and P.-F. Brevet. Interference between selected dipoles and octupoles in the optical second-harmonic generation from spherical gold nanoparticles. Physical Review Letters, **105**, 1 (2010).

[139] I. M. Hancu, A. G. Curto, M. Castro-López, M. Kuttge, and N. F. van Hulst. Multipolar interference for directed light emission. Nano Letters, **14**, 166 (2014).

[140] W. Liu, J. Zhang, B. Lei, W. Xie, H. Ma, and H. Hu. Ultra-directional forward scattering by individual core-shell nanoparticles. Optics Express, **22**, 16178 (2014).

[141] F. Zhou, Z. Li, Y. Liu, and Y. Xia. Quantitative analysis of dipole and quadrupole excitation in the surface plasmon resonance of metal nanoparticles. The Journal of Physical Chemistry C, **112**, 20233 (2008).

[142] J. Petschulat, J. Yang, C. Menzel, C. Rockstuhl, A. Chipouline, P. Lalanne, A. Tünnermann, F. Lederer, and T. Pertsch. Understanding the electric and magnetic response of isolated metaatoms by means of a multipolar field decomposition. Optics Express, **18**, 14454 (2010).

[143] M. J. Huttunen, J. Mäkitalo, G. Bautista, and M. Kauranen. Multipolar second-harmonic emission with focused Gaussian beams. New Journal of Physics, **14**, 113005 (2012).

[144] J. I. Dadap, J. Shan, K. B. Eisenthal, and T. F. Heinz. Second-harmonic Rayleigh scattering from a sphere of centrosymmetric material. Physical Review Letters, **83**, 4045 (1999).

[145] J. I. Dadap, J. Shan, and T. F. Heinz. Theory of optical second-harmonic generation from a sphere of centrosymmetric material: Small-particle limit. Journal of the Optical Society of America B, **21**, 1328 (2004).

[146] A. de Beer and S. Roke. Nonlinear Mie theory for second-harmonic and sum-frequency scattering. Physical Review B, **79**, 1 (2009).

[147] A. Capretti, C. Forestiere, L. Dal Negro, and G. Miano. Full-wave analytical solution of second-harmonic generation in metal nanospheres. Plasmonics, **9**, 151 (2014).

[148] J. Butet, I. Russier-Antoine, C. Jonin, N. Lascoux, E. Benichou, and P.-F. Brevet. Nonlinear Mie theory for the second harmonic generation in metallic nanoshells. Journal of the Optical Society of America B, **29**, 2213 (2012).

[149] B. Huo, X. Wang, S. Chang, M. Zeng, and G. Zhao. Second harmonic generation of individual centrosymmetric sphere excited by a tightly focused beam. Journal of the Optical Society of America B, **28**, 2702 (2011).

[150] B. Huo, X. Wang, S. Chang, and M. Zeng. Second harmonic generation of a single centrosymmetric nanosphere illuminated by tightly focused cylindrical vector beams. Journal of the Optical Society of America B, **29**, 1631 (2012).

[151] J. Xu and X. Zhang. Second harmonic generation in three-dimensional structures based on homogeneous centrosymmetric metallic spheres. Optics Express, **20**, 1668 (2012).

[152] Y. Pavlyukh and W. Hübner. Nonlinear Mie scattering from spherical particles. Physical Review B, **70**, 245434 (2004).

[153] J. Dewitz, W. Hübner, and K. Bennemann. Theory for nonlinear Mie-scattering from spherical metal clusters. Zeitschrift für Physik D, **37**, 75 (1996).

[154] P. P. Silvester and R. L. Ferrari. *Finite elements for electrical engineers* (Cambridge University Press, Cambridge, 1990).

[155] J. Wang and J. Webb. Hierarchal vector boundary elements and p-adaption for 3-D electromagnetic scattering. IEEE Transactions on Antennas and Propagation, **45**, 1869 (1997).

[156] W. Cai, T. Yu, H. Wang, and Y. Yu. High-order mixed RWG basis functions for electromagnetic applications. IEEE Transactions on Microwave Theory and Techniques, **49**, 1295 (2001).

[157] W. Cai, Y. Yu, and X. C. Yuan. Singularity treatment and high-order RWG basis functions for integral equations of electromagnetic scattering. International Journal for Numerical Methods in Engineering, **53**, 31 (2002).

[158] R. Graglia, D. Wilton, and A. Peterson. Higher order interpolatory vector bases for computational electromagnetics. IEEE Transactions on Antennas and Propagation, **45**, 329 (1997).

[159] M. Djordjevic and B. Notaros. Double higher order method of moments for surface integral equation modeling of metallic and dielectric antennas and scatterers. IEEE Transactions on Antennas and Propagation, **52**, 2118 (2004).

[160] E. Jorgensen, J. Volakis, P. Meincke, and O. Breinbjerg. Higher order hierarchical Legendre basis functions for electromagnetic modeling. IEEE Transactions on Antennas and Propagation, **52**, 2985 (2004).

[161] M. Bluck, A. Hatzipetrox, and S. Walker. Applications of differential forms to boundary integral equations. IEEE Transactions on Antennas and Propagation, **54**, 1781 (2006).

[162] P. Ylä-Oijala, M. Taskinen, and J. Sarvas. Surface integral equation method for general composite metallic and dielectric structures with junctions. Progress In Electromagnetics Research, **52**, 81 (2005).

[163] N. Marly, D. D. Zutter, and H. Pues. A surface integral equation approach to the scattering and absorption of doubly periodic lossy structures. IEEE Transactions on Electromagnetic Compatibility, **36**, 14 (1994).

[164] I. Stevanoviae and J. R. Mosig. Periodic Green's function for skewed 3-D lattices using the Ewald transformation. Microwave and Optical Technology Letters, **49**, 1353 (2007).

[165] X. Dardenne and C. Craeye. Method of moments simulation of infinitely periodic structures combining metal with connected dielectric objects. IEEE Transactions on Antennas and Propagation, **56**, 2372 (2008).

[166] I. Stevanovic, P. Crespo-Valero, K. Blagovic, F. Bongard, and J. R. Mosig. Integral-equation analysis of 3-D metallic objects arranged in 2-D lattices using the Ewald transformation. IEEE Transactions on Microwave Theory and Techniques, **54**, 3688 (2006).

[167] R. Araneo and G. Lovat. Fast MoM analysis of the shielding effectiveness of rectangular enclosures with apertures, metal plates, and conducting objects. IEEE Transactions on Electromagnetic Compatibility, **51**, 274 (2009).

[168] D. Wilton, S. Rao, A. Glisson, D. H. Schaubert, O. Al-Bundak, and C. Butler. Potential integrals for uniform and linear source distributions on polygonal and polyhedral domains. IEEE Transactions on Antennas and Propagation, **AP-32**, 276 (1984).

[169] P. Caorsi, D. Moreno, and F. Sidoti. Theoretical and numerical treatment of surface integrals involving the free-space Green's function. IEEE Transactions on Antennas and Propagation, **41**, 1296 (1993).

[170] R. Hodges and Y. Rahmat-Samii. The evaluation of MFIE integrals with the use of vector triangle basis functions. Microwave and Optical Technology Letters, **14**, 9 (1997).

[171] P. Ylä-Oijala and M. Taskinen. Calculation of CFIE impedance matrix elements with RWG and nxRWG functions. IEEE Transactions on Antennas and Propagation, **51**, 1837 (2003).

[172] I. Hänninen, M. Taskinen, and J. Sarvas. Singularity subtraction integral formulae for surface integral equations with RWG, rooftop and hybrid basis functions. Progress In Electromagnetics Research, **63**, 243 (2006).

[173] S. Järvenpää, M. Taskinen, and P. Ylä-Oijala. Singularity extraction technique for integral equation methods with higher order basis functions on plane triangles and tetrahedra. International Journal for Numerical Methods in Engineering, **58**, 1149 (2003).

[174] S. Järvenpää, M. Taskinen, and P. Ylä-Oijala. Singularity subtraction technique for high-order polynomial vector basis functions on planar triangles. IEEE Transactions on Antennas and Propagation, **54**, 42 (2006).

[175] M. Duffy. Quadrature over a pyramid or cube of integrands with a singularity at a vertex. SIAM Journal on Numerical Analysis, **19**, 1260 (1982).

[176] J. Lachat and J. Watson. Effective numerical treatment of boundary integral equations: A formulation for three dimensional elastostatics. International Journal for Numerical Methods in Engineering, **10**, 991 (1976).

[177] P. W. Fink, D. R. Wilton, and M. a. Khayat. New method for handling near-hypersingular integrals in BEM formulations. In *International Conference on Electromagnetics in Advanced Applications*, 978–981 (IEEE, 2007).

[178] R. D. Graglia and G. Lombardi. Machine precision evaluation of singular and nearly singular potential integrals by use of Gauss quadrature formulas for rational functions. IEEE Transactions on Antennas and Propagation, **56**, 981 (2008).

[179] M. Khayat and D. Wilton. Numerical evaluation of singular and near-singular potential integrals. IEEE Transactions on Antennas and Propagation, **53**, 3180 (2005).

[180] A. Polimeridis, F. Vipiana, J. R. Mosig, and D. R. Wilton. DIRECTFN: Fully numerical algorithms for high precision computation of singular integrals in Galerkin SIE methods. IEEE Transactions on Antennas and Propagation, **61**, 3112 (2013).

[181] W. T. Sheng, Z. Y. Zhu, K. Yang, and M. S. Tong. Efficient evaluation of weakly singular integrals arising from electromagnetic surface integral equations. IEEE Transactions on Antennas and Propagation, **61**, 3377 (2013).

[182] M. Tong and W. Chew. A novel approach for evaluating hypersingular and strongly singular surface integrals in electromagnetics. IEEE Transactions on Antennas and Propagation, **58**, 3593 (2010).

[183] D. Weile and X. Wang. Strong singularity reduction for curved patches for the integral equations of electromagnetics. Antennas and Wireless Propagation Letters, **8**, 1370 (2009).

[184] A. Klöckner, A. Barnett, L. Greengard, and M. O'Neil. Quadrature by expansion: A new method for the evaluation of layer potentials. Journal of Computational Physics, **252**, 332 (2013).

[185] Y. Saad. *Iterative methods for sparse linear systems* (Society for Industrial and Applied Mathematics, 2003).

[186] F. Andriulli, K. Cools, H. Ba, F. Olyslager, A. Buffa, S. Christiansen, and E. Michielssen. A multiplicative Calderón preconditioner for the electric field integral equation. IEEE Transactions on Antennas and Propagation, **56**, 2398 (2008).

[187] S. Yan, J.-M. Jin, and Z. Nie. A comparative study of Calderón preconditioners for PMCHWT equations. IEEE Transactions on Antennas and Propagation, **58**, 2375 (2010).

[188] K. Cools, F. Andriulli, and E. Michielssen. A Calderón multiplicative preconditioner for the PMCHWT integral equation. IEEE Transactions on Antennas and Propagation, **59**, 4579 (2011).

[189] M. Ayatollahi and S. Safavi-Naeini. An efficient plane wave expansion algorithm for analyzing low frequency scattering problems. In *IEEE Antennas and Propagation Society Symposium*, 635 – 638 (2004).

[190] M. Bebendorf. Approximation of boundary element matrices. Numerische Mathematik, **86**, 565 (2000).

[191] K. Zhao, M. N. Vouvakis, and J.-F. Lee. The adaptive cross approximation algorithm for accelerated method of moments computations of EMC problems. IEEE Transactions on Electromagnetic Compatibility, **47**, 763 (2005).

[192] M. Hamermesh. *Group theory* (Addison-Wesley Publishing Company Inc., 1962).

[193] P. Raumonen. *Mathematical structures for dimensional reduction and equivalence classification of electromagnetic boundary value problems*. Ph.D. thesis, Tampere University of Technology (2009).

[194] M. Bonnet. Exploiting partial or complete geometrical symmetry in 3D symmetric Galerkin indirect BEM formulations. International Journal for Numerical Methods in Engineering, **57**, 1053 (2003).

[195] J. Butet, A. Lovera, and O. J. F. Martin. Detecting the trapping of small metal nanoparticles in the gap of nanoantennas with optical second harmonic generation. Optics Express, **21**, 256 (2013).

[196] J. Butet and O. J. F. Martin. Nonlinear plasmonic nanorulers. ACS Nano, **8**, 4931 (2014).

[197] J. Butet, K. Thyagarajan, and O. J. F. Martin. Ultrasensitive optical shape characterization of gold nanoantennas using second harmonic generation. Nano Letters, **13**, 1787 (2013).

[198] K. Thyagarajan, J. Butet, and O. J. F. Martin. Augmenting second harmonic generation using Fano resonances in plasmonic systems. Nano Letters, **13**, 1847 (2013).

[199] J. Butet, S. Dutta-Gupta, and O. J. F. Martin. Surface second-harmonic generation from coupled spherical plasmonic nanoparticles: Eigenmode analysis and symmetry properties. Physical Review B, **89**, 245449 (2014).

[200] C. Forestiere, A. Capretti, and G. Miano. Surface integral method for second harmonic generation in metal nanoparticles including both local-surface and nonlocal-bulk sources. Journal of the Optical Society of America B, **30**, 2355 (2013).

[201] J. Butet, B. Gallinet, K. Thyagarajan, and O. J. F. Martin. Second-harmonic generation from periodic arrays of arbitrary shape plasmonic nanostructures: A surface integral approach. Journal of the Optical Society of America B, **30**, 2970 (2013).

[202] H. Husu, J. Mäkitalo, R. Siikanen, G. Genty, H. Pietarinen, J. Lehtolahti, J. Laukkanen, M. Kuittinen, and M. Kauranen. Spectral control in anisotropic resonance-domain metamaterials. Optics Letters, **36**, 2375 (2011).

[203] R. Czaplicki, H. Husu, R. Siikanen, J. Mäkitalo, M. Kauranen, J. Laukkanen, J. Lehtolahti, and M. Kuittinen. Enhancement of second-harmonic generation from metal nanoparticles by passive elements. Physical Review Letters, **110**, 093902 (2013).

[204] R. Harrington and J. Mautz. Theory of characteristic modes for conducting bodies. IEEE Transactions on Antennas and Propagation, **19**, 622 (1971).

Appendix: Gradient of periodic Green's function

In Section 3.4, periodic Green's function G_p was introduced. In BEM calculations, its gradient is also required. The spatial series form of the gradient of G_p is

$$\nabla' G_p(\mathbf{R}) = \frac{1}{4\pi} \sum_{n=-\infty}^{\infty} \sum_{m=-\infty}^{\infty} (\mathbf{R} - \boldsymbol{\rho}_{nm}) e^{ikR_{nm}} \left(\frac{1}{R_{nm}^3} - \frac{ik}{R_{nm}^2} \right) e^{i\mathbf{k}_0 \cdot \boldsymbol{\rho}_{nm}},$$

where $\mathbf{R} = \mathbf{r} - \mathbf{r}'$. The complementary error function can be written as

$$\operatorname{erfc}(z) = 1 - \frac{2}{\sqrt{\pi}} \int_0^z e^{-\xi^2} d\xi$$

and its derivative is

$$\operatorname{erfc}'(z) = -\frac{2}{\sqrt{\pi}} e^{-z^2}.$$

The gradient of the spatial part is then

$$\begin{aligned} \nabla' G_p^{\text{spat}} = & \frac{1}{8\pi} \sum_{n=-\infty}^{\infty} \sum_{m=-\infty}^{\infty} (\mathbf{R} - \boldsymbol{\rho}_{nm}) e^{i\mathbf{k}_0 \cdot \boldsymbol{\rho}_{nm}} \\ & \times \sum_{\pm} e^{\pm ikR_{nm}} \left[\frac{1 \mp ikR_{nm}}{R_{nm}^3} \operatorname{erfc}\left(R_{nm}E \pm \frac{ik}{2E} \right) + \frac{2E}{R_{nm}^2 \sqrt{\pi}} e^{-(R_{nm}E \pm ik/(2E))^2} \right]. \end{aligned}$$

The derivative of the spectral part with respect to x' is

$$\frac{d}{dx'} G_p^{\text{spec}} = \frac{1}{4A} \sum_{n=-\infty}^{\infty} \sum_{m=-\infty}^{\infty} k_{tx} \frac{e^{i\mathbf{k}_t \cdot \mathbf{R}}}{k_z} \sum_{\pm} e^{\mp ik_z(z-z')} \operatorname{erfc}\left(\frac{-ik_z}{2E} \pm (z - z')E \right).$$

The derivative with respect to y' is obtained by substituting k_{tx} by k_{ty}. The derivative with respect to z' is somewhat more complicated:

$$\begin{aligned} \frac{d}{dz'} G_p^{\text{spec}} = & \frac{1}{4A} \sum_{n=-\infty}^{\infty} \sum_{m=-\infty}^{\infty} \frac{e^{i\mathbf{k}_t \cdot \mathbf{R}}}{-ik_z} \sum_{\pm} \pm e^{\mp ik_z(z-z')} \\ & \times \left[ik_z \operatorname{erfc}\left(\frac{-ik_z}{2E} \pm (z - z')E \right) + \frac{2E}{\sqrt{\pi}} e^{-\left(\frac{-ik_z}{2E} \pm (z-z')E \right)^2} \right]. \end{aligned}$$

Publications

Publication I

Reprinted with permission from

J. Mäkitalo, S. Suuriniemi and M. Kauranen. Boundary element method for surface nonlinear optics of nanoparticles. Optics Express, **19**, 23386 – 23399 (2011). Erratum **21**, 10205 – 10206 (2013).

Publication II

Reprinted with permission from

J. Mäkitalo, M. Kauranen and S. Suuriniemi. Modes and resonances of plasmonic scatterers. Physical Review B, **89**, 165429 (2014).

PHYSICAL REVIEW B **89**, 165429 (2014)

Modes and resonances of plasmonic scatterers

Jouni Mäkitalo* and Martti Kauranen
Department of Physics, Tampere University of Technology, P.O. Box 692, FI-33101 Tampere, Finland

Saku Suuriniemi
Department of Electrical Engineering, Tampere University of Technology, P.O. Box 692, FI-33101 Tampere, Finland
(Received 7 November 2013; revised manuscript received 14 April 2014; published 29 April 2014)

We present a rigorous full-wave electromagnetic approach to analyze the modes and resonances of dielectric and plasmonic nanoparticles of practically any geometry. Using boundary integral operators, we identify the resonances as inherent properties of the particles and propose a modal expansion for their optical response. We show that the resonance frequencies are isolated points on the complex plane. The approach allows the particles to be analyzed without specifying an incident field, which can be separately tailored for the desired interaction with the modes. We also connect the general theory to the Mie theory in spherical geometry and provide a connection to the quasistatic theory. In comparison to earlier work on modes and resonances of scatterers, our approach has the benefit that modes are defined entirely over a compact boundary surface of the scatterer. Furthermore, the boundary integral operator is of second-kind Fredholm type, enabling the rigorous characterization of the resonances.

DOI: 10.1103/PhysRevB.89.165429 PACS number(s): 42.25.Fx, 02.30.Rz, 02.30.Sa, 73.20.Mf

I. INTRODUCTION

The optical responses of metal nanoparticles arise from the collective oscillations of their conduction electrons [1]. The responses are often discussed in terms of plasmon resonances and modes, which give rise to enhanced local fields near the particle surface, thereby amplifying optical processes, such as Raman scattering [2] and second-harmonic generation [3]. The resonances can be broadly tuned for a given application by the size, shape, and dielectric environment of the particles [4]. The concepts of mode and resonance are routinely used to describe conventional optical systems, such as cavities and waveguides, where the electromagnetic fields are defined within bounded domains. Mathematically, such problems are described by a self-adjoint Helmholtz operator, whose corresponding integral operator is compact, leading to a discrete modal eigenbasis, directly related to the resonances of the system. Such characterization of the operator spectrum is a central problem in the study of resonances.

In contrast, the electromagnetic interaction with nanoparticles is essentially a scattering problem, defined over an unbounded spatial domain. This makes it, mathematically speaking, difficult to characterize the spectrum of the pertinent operator and thus to define the resonances of the particle. Furthermore, it is not clear whether the resonances can be associated with any well-defined electromagnetic eigenmodes. For plasmonic metal nanoparticles, the casual use of the concept of resonance thus only implies that the plasmonic responses become strong at certain frequencies. This is commonly analyzed by relying on an incident probe field, usually a plane wave. The resulting near-field patterns are then qualitatively classified as modes. This approach depends on the chosen incident field and may not find all resonances, e.g., ones related to dark modes [5]. Neither does the approach reveal whether the field patterns are due to a single discrete mode, a combination of modes, or possibly a continuum of modes. Especially in the plasmonic community, previous approaches to resonances and modes have been by and large restricted to microscopic electron oscillation formalism [6,7] or perturbation of macroscopic electric fields based on quasistatics [8–12], only valid for scatterers much smaller than wavelength. These approaches do not fully account for radiation, i.e., time-dependent effects, which are very important for many common nanosystems, especially large particles.

Beyond the quasistatic regime, modes and resonances have been considered by various approaches in other branches of physics. One of the earliest theoretical works was by Baum on the identification of perfectly conducting targets by electromagnetic pulses relying on integral operators [13]. This, so-called singularity expansion method, was complemented by another approach, based on so-called characteristic modes (eigenmodes) of conducting objects [14]. This work was further developed in [15,16], and the theory has found applications in, e.g., evaluating antenna quality factors independent of excitation [17]. Some studies based on the volume integral operator have been done for dielectric [18–20] and plasmonic [21–23] objects. The volume integral operator involves a strongly singular kernel, which complicates the characterization of the operator spectrum and thus the physical resonances [24–26].

Further approaches include a coupled-dipole description [27], inverse scattering matrix analysis in the Fourier modal method [28,29], and modal solution of the Maxwell differential equations [30,31]. Little to no spectral analysis was presented in these cases.

Recently, the boundary integral operators have been found powerful in the accurate modeling of the linear [32–35] and nonlinear [36] optical properties of plasmonic nanoparticles. Boundary integral operators have been utilized for analyzing the resonances of two-dimensional dielectric bodies [37] and the eigenmodes of three-dimensional dielectric objects [38]. On the other hand, there has been increased interest in

*jouni.makitalo@tut.fi

discovering modal expansions for plasmonic scattering problems, as this enables a meaningful approach to the evaluation of mode volumes and the Purcell factor [39,40]. This factor is proportional to the partial local density of states (LDOS), which determines the spontaneous emission decay rate of a dipole emitter [41]. The modes of the system determine the LDOS, which is then a measurable quantity that is independent of excitation. Thus a theoretically sound approach to modes and resonances by boundary integral operators is called for.

In this paper, we present an approach that allows the modes and resonances of essentially arbitrary nanoparticles to be analyzed in the strict electromagnetic sense, fully accounting for radiation effects. The approach treats the modes and resonances as inherent properties of the particle itself, independent of any incident field. By relying on boundary integral operators, the modes are defined over the spatially bounded surface of the particle and can be related to its resonances. We further show that our approach is compatible with the Mie theory for spherical particles and show calculations for more complicated shapes. By separating the particle properties from the incident field, our approach can provide fundamental information on very general nanoparticle systems. Our approach is applicable to particles made of any piecewise homogeneous material. However, it has particular importance in plasmonics, where the applications are based on detailed tailoring of the near field at the particle surface.

II. BOUNDARY INTEGRAL OPERATORS

Our rigorous electromagnetic approach to modes and resonances in scattering problems is based on a boundary integral formulation, where the modes are defined over the surface of the nanoparticle. The particle occupies a bounded domain V_2 with complex permittivity ϵ_2 and permeability μ_2 as illustrated in Fig. 1. The domain V_1, external to V_2, is unbounded with real permittivity ϵ_1 and permeability μ_1. The particle surface S is assumed C^2 smooth, i.e., a normal $\mathbf{n}$ pointing into V_1 exists at each point on S and varies continuously.

First we consider the direct scattering problem, where incident fields $\mathbf{E}_{\text{inc}}$ and $\mathbf{H}_{\text{inc}}$ are known and the electric fields $\mathbf{E}_l$ and magnetic fields $\mathbf{H}_l$ over domains V_l ($l = 1,2$) are sought. The fields have complex time-harmonic dependence $\exp(-i\omega t)$, satisfy the vector Helmholtz equations [42] in V_1 and V_2, and have tangential continuity on S. The scattered fields $\mathbf{E}_s = \mathbf{E}_1 - \mathbf{E}_{\text{inc}}$ and $\mathbf{H}_s = \mathbf{H}_1 - \mathbf{H}_{\text{inc}}$ must be outwards

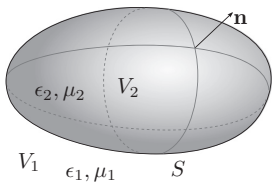

FIG. 1. Prototype geometry and parameters of the scattering problem.

propagating transverse spherical waves far from the particle,

$$\lim_{|\mathbf{r}|\to\infty} \sqrt{\epsilon_1}\mathbf{E}_s \times \mathbf{r} + |\mathbf{r}|\sqrt{\mu_1}\mathbf{H}_s = \mathbf{0}, \tag{1}$$

which is called the Silver-Müller radiation condition. This condition is sufficient to determine a unique solution to the Helmholtz equations with given incident fields. However, the condition renders the Helmholtz operators non-self-adjoint. Furthermore, because the solution domain is unbounded, it is difficult to analyze the modes and resonances using the Helmholtz operator. Specifically, the fields involved are not square-integrable over V_1, as an infinite amount of energy has been scattered in the steady state.

We avoid these issues by reformulating the problem using integral operators, which bring the problem to the compact (bounded and closed) surface S. This is done by introducing the fundamental Green's function $G_l(\mathbf{r},\mathbf{r}') = \exp(ik_l R)/(4\pi R)$ ($R = |\mathbf{r} - \mathbf{r}'|$) for the two domains $l = 1,2$ with wave numbers $k_l = \omega\sqrt{\epsilon_l \mu_l}$. We define boundary integral operators, which map functions $\mathbf{f} : \partial V_l \to \mathbb{C}^3$ defined over the surface to functions defined over the domains V_l:

$$(\mathcal{D}_l\mathbf{f})(\mathbf{r}) = i\omega\mu_l \int_{\partial V_l} G_l(\mathbf{r},\mathbf{r}')\mathbf{f}(\mathbf{r}')dS' - \frac{1}{i\omega\epsilon_l}\nabla \int_{\partial V_l} G_l(\mathbf{r},\mathbf{r}')\nabla_t' \cdot \mathbf{f}(\mathbf{r}')dS', \tag{2}$$

$$(\mathcal{K}_l\mathbf{f})(\mathbf{r}) = \int_{\partial V_l} [\nabla' G_l(\mathbf{r},\mathbf{r}')] \times \mathbf{f}(\mathbf{r}')dS', \tag{3}$$

where $\nabla_t \cdot \mathbf{f}$ is the surface (tangential) divergence.

Through the use of Green's function and Green's identities we may derive the so-called Stratton-Chu equations [42], which give the fields over V_1 and V_2 from functions on S through the integral operators:

$$\Omega_l\mathbf{H}_l = \delta_{l1}\mathbf{H}_{\text{inc}} + \mathcal{D}_l\mathbf{E}_l \times \mathbf{n}_l/\eta_l^2 - \mathcal{K}_l\mathbf{n}_l \times \mathbf{H}_l, \tag{4}$$

$$\Omega_l\mathbf{E}_l = \delta_{l1}\mathbf{E}_{\text{inc}} + \mathcal{D}_l\mathbf{n}_l \times \mathbf{H}_l + \mathcal{K}_l\mathbf{E}_l \times \mathbf{n}_l, \tag{5}$$

where normals $\mathbf{n}_l$ point into V_l and we introduced the impedance $\eta_l = \sqrt{\mu_l/\epsilon_l}$ and the Kronecker delta, δ_{nm}. The number Ω_l equals 1 if $\mathbf{r} \in V_l - \partial V_l$, zero if $\mathbf{r} \notin V_l \cup \partial V_l$, and $1/2$ if $\mathbf{r} \in \partial V_l$. The scattered fields given by the operators satisfy the Silver-Müller conditions. The operators $\mathcal{D}_l$, however, have strongly singular kernels due to the gradient term, which makes the analysis of modes and resonances more challenging.

It is conventional to introduce the equivalent surface current densities to represent the boundary fields:

$$\mathbf{J}_l = \mathbf{n}_l \times \mathbf{H}_l, \tag{6}$$

$$\mathbf{M}_l = \mathbf{E}_l \times \mathbf{n}_l. \tag{7}$$

In terms of these quantities, we obtain the following boundary integral equations:

$$\tfrac{1}{2}\mathbf{J}_l = \delta_{l1}\mathbf{J}_{\text{inc}} + \mathbf{n}_l \times \mathcal{D}_l\mathbf{M}_l/\eta_l^2 - \mathbf{n}_l \times \mathcal{K}_l\mathbf{J}_l, \tag{8}$$

$$\tfrac{1}{2}\mathbf{M}_l = \delta_{l1}\mathbf{M}_{\text{inc}} - \mathbf{n}_l \times \mathcal{D}_l\mathbf{J}_l - \mathbf{n}_l \times \mathcal{K}_l\mathbf{M}_l, \tag{9}$$

where the integration in $\mathcal{K}_l$ is defined in the Cauchy principal value sense [42].

There are various ways to formulate the scattering problem by the use of the Eqs. (8) and (9). However, in the Müller formulation [43], the strong singularities in the operators $\mathcal{D}_l$ cancel out, enabling us to rigorously analyze the physical resonances. Next we derive this formulation. Let $\xi_\epsilon = 1/(\epsilon_1 + \epsilon_2)$ and $\xi_\mu = 1/(\mu_1 + \mu_2)$. Then multiply Eq. (8) by $\mu_l\xi_\mu$ and Eq. (9) by $\epsilon_l\xi_\epsilon$ and subtract the equations corresponding to the two domains. Further, we impose the continuity of the tangential field components as

$$\mathbf{J} = \mathbf{J}_1 = -\mathbf{J}_2, \tag{10}$$

$$\mathbf{M} = \mathbf{M}_1 = -\mathbf{M}_2, \tag{11}$$

and set $\mathbf{n} = \mathbf{n}_1 = -\mathbf{n}_2$ to obtain [43,44]

$$\tfrac{1}{2}\mathbf{J} = \xi_\mu[\mu_1\mathbf{J}_{\rm inc} + (\epsilon_1\mathbf{n}\times\mathcal{D}_1 - \epsilon_2\mathbf{n}\times\mathcal{D}_2)\mathbf{M} + (-\mu_1\mathbf{n}\times\mathcal{K}_1 + \mu_2\mathbf{n}\times\mathcal{K}_2)\mathbf{J}], \tag{12}$$

$$\tfrac{1}{2}\mathbf{M} = \xi_\epsilon[\epsilon_1\mathbf{M}_{\rm inc} + (-\epsilon_1\mathbf{n}\times\mathcal{D}_1 + \epsilon_2\mathbf{n}\times\mathcal{D}_2)\mathbf{J} + (-\epsilon_1\mathbf{n}\times\mathcal{K}_1 + \epsilon_2\mathbf{n}\times\mathcal{K}_2)\mathbf{M}]. \tag{13}$$

This can be arranged into a matrix form,

$$(\mathcal{I} + \mathcal{A}(\omega))\mathbf{f} = \mathbf{g}, \tag{14}$$

where $\mathcal{I}$ is the identity operator, $\mathbf{f} = (\eta_1\mathbf{J},\mathbf{M})$ is the unknown solution, and $\mathbf{g} = (2\eta_1\mu_1\xi_\mu\mathbf{J}_{\rm inc}, 2\epsilon_1\xi_\epsilon\mathbf{M}_{\rm inc})$ is the tangential component of the incident field on S and the matrix entries can be deduced directly from Eqs. (12) and (13). We write the frequency dependency of the operator $\mathcal{A}(\omega)$ explicitly as we are interested in the resonance frequencies.

III. ANALYSIS OF BOUNDARY INTEGRAL OPERATORS

In this section we review some results of functional analysis of linear operators between Hilbert spaces. In the spectral analysis, the concepts of adjoint operator and compact operator are paramount. We denote by $L^2(S)$ a Hilbert space of square-integrable functions over a surface S endowed with an inner product $\langle\cdot,\cdot\rangle$. The *adjoint* of an operator $\mathcal{L} : L^2(S) \to L^2(S)$, denoted by $\mathcal{L}^\dagger$, satisfies $\langle\mathcal{L}\mathbf{f}_1,\mathbf{f}_2\rangle = \langle\mathbf{f}_1,\mathcal{L}^\dagger\mathbf{f}_2\rangle$ for all $\mathbf{f}_1$ and $\mathbf{f}_2$ in $L^2(S)$. A particularly well-studied class of operators are the self-adjoint operators, for which $\mathcal{L} = \mathcal{L}^\dagger$ holds.

The inner product induces the norm $|\mathbf{f}| = \sqrt{\langle\mathbf{f},\mathbf{f}\rangle}$. An operator $\mathcal{L}$ is *bounded* if there exists a positive real number K such that $|\mathcal{L}\mathbf{f}| < K|\mathbf{f}|$ for all $\mathbf{f}$. Bounded operators always have a unique adjoint. A bounded operator is *compact*, if for every sequence in the domain of the operator there exists a convergent subsequence in the image sequence. The intuition behind a compact operator $\mathcal{L}$ is that there exists a finite-dimensional subspace M of the range of $\mathcal{L}$ such that any image $\mathcal{L}\mathbf{f}$ can be approximated to an arbitrary degree by an element of M. Thus compact operators are among the best-understood operators mapping between infinite-dimensional spaces.

The spectrum of an operator $\mathcal{L}$ is defined in terms of the resolvent operator $(\mathcal{L} - \lambda\mathcal{I})^{-1}$ [45]. The complex numbers λ are generally divided into two disjoint subsets: *the spectrum* $\sigma(\mathcal{L})$ and *the resolvent set* $\rho(\mathcal{L}) = \mathbb{C} - \sigma(\mathcal{L})$. A number λ is defined to be in the spectrum $\sigma(\mathcal{L})$, if the resolvent fails to exist as a bounded operator for this number. Otherwise the number λ is said to be in the resolvent set $\rho(\mathcal{L})$. The spectrum can be further decomposed into disjoint sets called the point spectrum (the eigenvalues), the continuous spectrum, and the residual spectrum. Finding these sets is a central problem in the spectral theory of linear operators.

An important property of compact operators is that all nonzero spectral values are eigenvalues [45]. Furthermore, their point spectrum is discrete (despite the name, the point spectrum of an operator is not a discrete set in general) and the elements may be arranged so that they tend towards zero. Operators of the form $\mathcal{I} + \mathcal{L}$, where $\mathcal{L}$ is compact, are called *Fredholm operators of the second kind* [45]. For such operators, resonances can be rigorously identified and this is done in the next section.

We next consider the compactness of the operators $\mathcal{D}_l$ and $\mathcal{K}_l$. Consider a surface integral operator $\mathcal{L}$ of the form

$$(\mathcal{L}f)(\mathbf{r}) = \int_S g(\mathbf{r},\mathbf{r}')f(\mathbf{r}')dS', \tag{15}$$

which maps functions defined on an n-dimensional surface S embedded in $n+1$-dimensional Euclidean space. Such an operator is compact in $L^2(S)$, if the kernel g is of the form

$$g(\mathbf{r},\mathbf{r}') = \frac{g_b(R)}{R^m}, \quad R = |\mathbf{r} - \mathbf{r}'|, \tag{16}$$

with $0 \leqslant m < n$ and g_b is bounded [45]. In our case $n = 2$ holds.

In the electromagnetic scattering problem, we come across three different kinds of integral operators involving the kernel $G(\mathbf{r},\mathbf{r}') = \exp(ikR)/(4\pi R)$. The first one is

$$(\mathcal{D}^s\mathbf{f})(\mathbf{r}) = \int_S G(\mathbf{r},\mathbf{r}')\mathbf{f}(\mathbf{r}')dS'. \tag{17}$$

In this case $m = 1$ holds, so $\mathcal{D}^s$ is compact in $L^2(S)$.

The second one is

$$(\mathcal{D}^h\mathbf{f})(\mathbf{r}) = \nabla\int_S G(\mathbf{r},\mathbf{r}')\nabla'_t\cdot\mathbf{f}(\mathbf{r}')dS'. \tag{18}$$

The kernel is hypersingular (when the gradient is moved under the integral) and the operator is noncompact, even for smooth S. Thus the characterization of the spectrum of this operator is difficult. However, in the Müller formulation, this operator only appears as differences of the form $\mathcal{D}^h_1 - \mathcal{D}^h_2$. The kernel of the operator

$$\mathcal{D}^h_1 - \mathcal{D}^h_2 = \int_S G_d(\mathbf{r},\mathbf{r}')\nabla'_S\cdot\mathbf{f}(\mathbf{r}')dS' \tag{19}$$

is

$$G_d(\mathbf{r},\mathbf{r}') = \frac{1}{4\pi}\sum_{n=0}^{\infty}\frac{n-1}{n!}R^{n-3}[(ik_1)^n - (ik_2)^n](\mathbf{r}-\mathbf{r}'), \tag{20}$$

whose first nonzero element is $n = 2$ [44]. This term is of the form $(\mathbf{r} - \mathbf{r}')/R$, whence the operator is compact.

The third operator is of the form

$$(\mathbf{n}\times\mathcal{K}\mathbf{f})(\mathbf{r}) = \mathbf{n}\times\int_S \nabla'G(\mathbf{r},\mathbf{r}')\times\mathbf{f}(\mathbf{r}')dS', \tag{21}$$

which is compact, provided that the surface is C^2 smooth [45]. The tangential trace $\mathbf{n}\times$ lowers the degree of the strong singularity in $\nabla' G$.

The domain and range of the operator $\mathcal{A}$ in the Müller formulation may be chosen as the Hilbert space of square-integrable functions embedded with the inner product

$$\langle \mathbf{f}_1, \mathbf{f}_2 \rangle = \int_S \mathbf{f}_1^* \cdot \mathbf{f}_2 dS = \int_S \left(\eta_1^2 \mathbf{J}_1^* \cdot \mathbf{J}_2 + \mathbf{M}_1^* \cdot \mathbf{M}_2 \right) dS. \quad (22)$$

IV. RESONANCES AND MODES

A. Full-wave theory

The system must have a resonance if Eq. (14) allows a nonvanishing solution for no incident field,

$$(\mathcal{I} + \mathcal{A}(\omega))\mathbf{f}_0 = 0. \quad (23)$$

This can lead to nonzero solutions $\mathbf{f}_0$ only if the inverse operator $(\mathcal{I} + \mathcal{A}(\omega))^{-1}$ is singular at certain frequencies ω, which are generally complex. Due to the compactness of $\mathcal{A}(\omega)$ as was established in the previous section, the operator $\mathcal{I} + \mathcal{A}(\omega)$ is second-kind Fredholm and the analytic Fredholm theorem is applicable [45]. Consequently, the inverse can have only pole singularities in the region of complex frequency plane where $\mathcal{A}(\omega)$ is analytic. The poles occur at isolated points [46], yielding the complex resonance frequencies, which we denote by ω_n. At all other frequencies, the inverse exists and is analytic. The resonance modes $\mathbf{f}_{0n}$ corresponding to a given ω_n constitute a finite-dimensional space, i.e., there can be only finite degeneracy [45]. The resonance frequencies shift continuously as S changes continuously [45]. *After fixing the geometry and media, the resonances can thus be solved from Eq. (23) with no assumed incident field.*

In the near-infrared and optical regimes, the permittivity of plasmonic materials can be described by the Drude model:

$$\epsilon(\omega)/\epsilon_0 = 1 - \frac{\omega_p^2}{\omega^2 + i\gamma\omega}, \quad (24)$$

where ω_p is the plasma frequency and γ is the damping frequency [47]. This dispersion gives rise to branch-point singularities at zero frequency and at $\omega = (\pm\sqrt{4\omega_p^2 - \gamma^2} - i\gamma)/2$, which give rise to two branch cuts for $\mathcal{A}(\omega)$ that restrict the region of analyticity. The structure of the resonances is illustrated in Fig. 2. The appearance of branch-point singularities due to losses was predicted in [48].

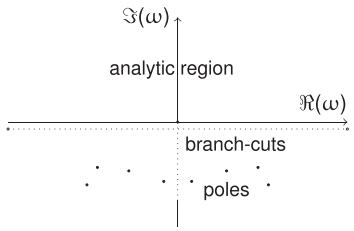

FIG. 2. Illustration of the singularities of inverse boundary integral operator for Drude-type dispersion.

Note that the resonance frequencies must reside in the lower half of the complex plane. This requirement, together with the radiation condition, implies that the scattered fields of the resonance modes $\mathbf{f}_{0n}$ grow exponentially with distance as the waves propagate towards infinity [40]. Thus, instead of using the resonance modes $\mathbf{f}_{0n}$ directly, we will look for eigenmodes defined at real frequencies to establish an expansion of solutions and relate these modes to the resonance modes found at complex frequencies.

We seek possible eigenmodes for a *fixed* real frequency ω as

$$(\mathcal{I} + \mathcal{A}(\omega))\mathbf{f}_n = \lambda_n \mathbf{f}_n, \; n \text{ integer}. \quad (25)$$

Although not explicitly indicated, these modes and eigenvalues depend also on frequency. *Thus for each fixed frequency, we obtain a set of eigenmodes*. This set is *discrete* due to the compactness [45] of $\mathcal{A}(\omega)$. It is then expected that if at a particular frequency ω there exists an eigenvalue λ_n close to zero, the corresponding mode $\mathbf{f}_n$ is nearly resonant.

We then expand the solution at frequency ω in terms of the modes

$$\mathbf{f} = \sum_n \alpha_n \mathbf{f}_n. \quad (26)$$

To relate the excitation of the modes to a given incident field $\mathbf{g}$, we need the coefficients α_n. The eigenmodes of operator $\mathcal{I} + \mathcal{A}$ are not necessarily orthogonal, as the operator $\mathcal{A}$ is not self-adjoint in general. To overcome this problem, we consider the eigenmodes of the adjoint operator $\mathcal{A}^\dagger$. If λ_n is an eigenvalue from Eq. (25) for mode $\mathbf{f}_n$, then its complex conjugate λ_n^* is an eigenvalue of the adjoint operator with corresponding adjoint mode $\mathbf{h}_n$ [45]:

$$(\mathcal{I} + \mathcal{A}^\dagger)\mathbf{h}_n = \lambda_n^* \mathbf{h}_n. \quad (27)$$

The modes and the adjoint modes are biorthogonal in the sense of $(\lambda_n - \lambda_m)\langle \mathbf{f}_n, \mathbf{h}_m \rangle = 0$ [45]. This implies $\langle \mathbf{f}_n, \mathbf{h}_m \rangle = 0$ for all $\lambda_n \neq \lambda_m$. Remember that this biorthogonality applies at a fixed frequency ω.

Through substitution of Eq. (26) to Eq. (14) and using Eq. (25), we obtain for all integers m,

$$\sum_n \alpha_n \lambda_n \langle \mathbf{h}_m, \mathbf{f}_n \rangle = \langle \mathbf{h}_m, \mathbf{g} \rangle. \quad (28)$$

Symmetries in the shape of S may lead to degenerate modes, sharing the same eigenvalue. In this case, the corresponding modes and adjoint modes are not necessarily biorthogonal, and we obtain a finite linear system for coefficients α_n. In the absence of degeneracy, we obtain

$$\alpha_n = \frac{\langle \mathbf{h}_n, \mathbf{g} \rangle}{\lambda_n \langle \mathbf{h}_n, \mathbf{f}_n \rangle}. \quad (29)$$

A small eigenvalue $|\lambda_n|$ can clearly lead to an enhanced response for the respective mode. This indicates a pole of the inverse operator at complex frequency ω_n near ω. To study the response of a particle, we first find its modes $\mathbf{f}_n$, independent of incident field, then evaluate α_n to see how a particular incident field $\mathbf{g}$ couples to the modes.

B. Quasistatic limit

The off-diagonal operators in $\mathcal{A}(\omega)$ [see Eqs. (12) and (13)] are $O(\omega)$ polynomials of frequency, even though the operators $\mathcal{D}_l$ are $O(1/\omega)$. This occurs for the same reason as the cancellation of the strong spatial singularity in the difference $\epsilon_1\mathbf{n}\times\mathcal{D}_1-\epsilon_2\mathbf{n}\times\mathcal{D}_2$ [44]. For this reason, the off-diagonal operators tend to zero as ω tends to zero. This is in contrast to, e.g., the Poggio-Miller-Chang-Harrington-Wu-Tsai (PMCHWT) formulation [49], for which the zero-frequency limit does not exist due to a $1/\omega$ factor. The limit of the operator $\mathcal{K}_l$ is simply

$$\lim_{\omega\to 0}(\mathcal{K}_l\mathbf{f})(\mathbf{r})=(K\mathbf{f})(\mathbf{r})=\int_{\partial V_l}\nabla'\frac{1}{4\pi R}\times\mathbf{f}(\mathbf{r}')dS'. \quad (30)$$

Thus the static limit is

$$\mathcal{A}(0)=2\begin{pmatrix}\frac{\mu_1-\mu_2}{\mu_1+\mu_2}\mathbf{n}\times K & 0\\ 0 & \frac{\epsilon_1-\epsilon_2}{\epsilon_1+\epsilon_2}\mathbf{n}\times K\end{pmatrix}, \quad (31)$$

where the electric and magnetic parts are decoupled.

Then the electrostatic (or quasistatic) formulation is obtained via introduction of the electrostatic potential ϕ so that $\mathbf{E}=-\nabla\phi$:

$$\phi-\lambda K\phi=2\epsilon_1\phi^{\text{inc}}, \quad (32)$$

$$(K\phi)(\mathbf{r})=\frac{1}{2\pi}\int_S\frac{\partial}{\partial n'}\frac{1}{R}\phi(\mathbf{r}')dS', \quad (33)$$

where $\lambda=(\epsilon_2-\epsilon_1)/(\epsilon_2+\epsilon_1)$. This potential formulation has been used to define plasmon resonances in the quasistatic limit [9]. It can be shown that $|\lambda|\geqslant 1$ holds for the eigenvalues λ. This condition is only met in practice if $\Re(\epsilon_2)<0$ holds, which is characteristic of plasmonic materials. Note that in the quasistatic regime, K is not frequency dependent, but ϵ_2 is considered frequency dependent. Thus the eigenvalue λ yields eigenpermittivity ϵ_2, which yields a resonance frequency through a dispersion relation. In the time-harmonic case, the operators depend on both $\epsilon_2(\omega)$ and ω in a nontrivial way such that the frequency dependence cannot be separated from the operators as a simple multiplication by a constant.

The theory of resonances based on the Müller formulation is then a generalization of the quasistatic theory [9]. A curious difference in the spectral structure of the full-wave and quasistatic cases can be observed: in the latter, the imaginary part of a resonance frequency is directly determined by the material damping constant γ. This is also true for all higher-order perturbation corrections, as the quasistatic eigenvalue is always real valued. Consequently, the quasistatics-based perturbation predicts that all resonance frequencies reside on the branch cut. This is not the case in general, and as we shall see in Sec. VII, the resonance frequencies reside rather far off from this branch cut, even for moderately sized nanoparticles. This further suggests that the quasistatics-based perturbation series does not converge towards a correct solution.

V. FINITE-DIMENSIONAL FORMULATION

A. Method of moments

In practice, the solution to Eqs. (23) and (25) may not be found in closed form if the geometry is complicated. To obtain approximate solutions to Eq. (14) by numerical computation, we utilize the method of moments with Galerkin's weighting [50]. The space $L^2(S)$ is approximated by a finite-dimensional space spanned by the Rao-Wilton-Glisson (RWG) functions [51]. An RWG function $\mathbf{b}_n$ is nonzero only over a pair of triangles T_n^+ and T_n^- of areas A_n^+ and A_n^- and the triangles have a common edge of length l_n. The vertices off the common edge are denoted $\mathbf{r}_n^+$ and $\mathbf{r}_n^-$. With these notations,

$$\mathbf{b}_n(\mathbf{r})=\begin{cases}\frac{l_n}{2A_n^+}(\mathbf{r}-\mathbf{r}_n^+), & \mathbf{r}\in T_n^+\\ \frac{l_n}{2A_n^-}(\mathbf{r}_n^--\mathbf{r}), & \mathbf{r}\in T_n^-\\ 0, & \text{otherwise.}\end{cases} \quad (34)$$

The surface divergence of RWG functions exists over $T_n^-\cup T_n^+$ and thus the approximate space is divergence conforming.

We next seek solutions to Eq. (14) from the space spanned by the RWG functions. By the use of the method of moments, a linear system of equations is obtained. We define the following basis moment matrix:

$$B_{mn}=\int_S\mathbf{b}_m\cdot\mathbf{b}_n dS; \quad (35)$$

and the following functions:

$$\mathbf{b}'_n=\begin{cases}(\mathbf{b}_n,\mathbf{0})^T, & n=1,2,\ldots,N\\ (\mathbf{0},\mathbf{b}_n)^T, & n=N+1,N+2,\ldots,2N;\end{cases} \quad (36)$$

and the following matrix:

$$\mathrm{B}'=\begin{pmatrix}\mathrm{B} & 0\\ 0 & \mathrm{B}\end{pmatrix}. \quad (37)$$

The solution is then expanded as

$$\mathbf{f}=\sum_{n=1}^{2N}c_n\mathbf{b}'_n. \quad (38)$$

This expression is inserted into $(\mathcal{I}+\mathcal{A})\mathbf{f}=\mathbf{g}$, which is then tested by $\mathbf{b}'_m$ via the inner product $\langle\cdot,\cdot\rangle$, which results in the following linear system of equations:

$$(\mathrm{B}'+\mathrm{A})\mathbf{x}=\mathbf{y}, \quad (39)$$

where $\mathbf{x}=\{c_1,c_2,\ldots,c_{2N}\}$ and the components of $\mathbf{y}$ are $y_m=\langle\mathbf{b}'_m,\mathbf{g}\rangle$. The components of the matrix A are $A_{mn}=\langle\mathbf{b}'_m,\mathcal{A}\mathbf{b}'_n\rangle$. The linear system of equations is generally well conditioned due to the second-kind Fredholm nature of the operator [44].

The matrix elements A_{mn} involve the evaluation of integrals with weakly singular kernels. The evaluation was done by the use of the singularity subtraction technique [52], where the singular parts are integrated analytically and a seventh-order Gauss-Legendre quadrature is used for the remaining smooth part.

The off-diagonal elements of the operator A require evaluation of the expression

$$I=\int_{T_m^\pm}\mathbf{b}_m\cdot\mathbf{n}\times\nabla\int_{T_n^\pm}G_s(\mathbf{r},\mathbf{r}')\nabla'_t\cdot\mathbf{b}_n dS'dS, \quad (40)$$

where the subscripts 1 and 2 refer to the external and the particle domains, respectively. We denote a combined kernel as $G_s = G_1 - G_2$. The application of partial integration to the outer integral yields

$$I = \int_{\partial T_m^{\pm}} \mathbf{b}_m \cdot \mathbf{l} \int_{T_n^{\pm}} G_s(\mathbf{r},\mathbf{r}') \nabla_t' \cdot \mathbf{b}_n dS' dC - \int_{T_m^{\pm}} \nabla_t \cdot (\mathbf{b}_m \times \mathbf{n}) \int_{T_n^{\pm}} G_s(\mathbf{r},\mathbf{r}') \nabla_t' \cdot \mathbf{b}_n dS' dS, \quad (41)$$

where $\mathbf{l}$ is a unit vector tangent to $\partial T_m^{\pm}$ which has induced orientation from that of S. The second integral vanishes because $\nabla_t \cdot (\mathbf{b}_m \times \mathbf{n}) = 0$ holds for RWG functions. This implies that Galerkin's method with RWG functions as test functions may not be the most accurate discretization scheme for the Müller formulation. This has been analyzed in [53], where the use of the rotated Buffa-Christiansen functions are suggested as test functions. For our purposes, however, the results are sufficiently accurate. Thus

$$I = \int_{\partial T_m^{\pm}} \mathbf{b}_m \cdot \mathbf{l} \int_{T_n^{\pm}} G_s(\mathbf{r},\mathbf{r}') \nabla_t' \cdot \mathbf{b}_n dS' dC. \quad (42)$$

The combined kernel G_s is a continuous function due to the cancellation of $1/R$ terms.

The approximate form of the eigenvalue problem becomes

$$(\mathrm{I} + \mathrm{B}'^{-1}\mathrm{A})\mathbf{x}_n = \lambda_n \mathbf{x}_n. \quad (43)$$

The resonances occur when $\det(\mathrm{I} + \mathrm{B}'^{-1}\mathrm{A}(\omega)) = 0$ holds. The Fredholm property of $\mathcal{I} + \mathcal{A}$ guarantees that if the approximate operator converges towards the original operator with respect to some discretization parameter, then the approximate resonance frequencies also approach the exact resonance frequencies [45].

Usually electromagnetic scattering can be formulated in Lipschitz continuous domains, which allow for sharp corners, but prevent such sharpness that would lead to infinite energy in finite volumes. Being able to allow sharp features is useful, as most numerical schemes consider flat polygonal representations of the boundary surface. However, while the compactness of the operator $\mathcal{A}$ has been established for smooth surfaces, the compactness with a Lipschitz continuous surface is an open issue. Thus an additional spectral structure may be present in the numerical solutions if polygonal surfaces are used. In the approximate context, the matrix representation of the operator has as many eigenvalues as is the dimension of the matrix. Some of the eigenvalues may be related to the additional spectral structure introduced by the numerical scheme.

B. Matrix of adjoint operator

To obtain the modal expansion coefficients, we wish to obtain approximations for the adjoint modes $\mathbf{h}_n$ in the RWG basis. We can use the matrix A for this instead of finding out explicitly what $\mathcal{A}^{\dagger}$ is.

Let us have an operator $\mathcal{A} : H \to H$ and a basis $H_b = \{\mathbf{b}_1, \ldots, \mathbf{b}_N\}$ in a finite-dimensional subspace of H. The operator has an approximate matrix representation A in this basis, so that $A_{mn} = \langle \mathbf{b}_m, \mathcal{A}\mathbf{b}_n \rangle$. The approximate matrix representation of the adjoint operator $\mathcal{A}^{\dagger}$ in basis H_b is

$$\mathrm{A}^{\dagger} = \mathrm{B}^{-1}\mathrm{A}^*\mathrm{B}, \quad (44)$$

where $B_{mn} = \langle \mathbf{b}_m, \mathbf{b}_n \rangle$ holds and A^* is the Hermitian transpose of A. The dual basis is defined by $\langle \mathbf{b}^m, \mathbf{b}_n \rangle = \delta_{mn}$. The B matrices correspond to change from the dual basis $H^b = \{\mathbf{b}^1, \ldots, \mathbf{b}^N\}$ to the primary basis H_b.

C. Evaluation of excitation coefficients

Next, we elaborate on the evaluation of the modal excitation coefficients in the approximate context. Let us expand $\mathbf{f}$ in terms of the eigenmodes as in Eq. (26). Then, in the case of no degeneracy,

$$\alpha_n = \frac{\langle \mathbf{h}_n, \mathbf{g} \rangle}{\lambda_n \langle \mathbf{h}_n, \mathbf{f}_n \rangle} \quad (45)$$

are the coefficients for the solution to the problem $(\mathcal{I} + \mathcal{A})\mathbf{f} = \mathbf{g}$.

Let $\mathbf{h}_n$ be expanded in the RWG basis as

$$\mathbf{h}_n = \sum_m \left(a_m^{h,n} \mathbf{b}_m, b_m^{h,n} \mathbf{b}_m \right). \quad (46)$$

Then

$$\langle \mathbf{h}_n, \mathbf{g} \rangle = \sum_m \left(a_m^{h,n*} c_m^J + b_m^{h,n*} c_m^M \right), \quad (47)$$

where

$$c_m^J = 2\eta_1 \mu_1 \xi_\mu \int_S \mathbf{b}_m \cdot \mathbf{J}_{\mathrm{inc}} dS, \quad (48)$$

$$c_m^M = 2\epsilon_1 \xi_\epsilon \int_S \mathbf{b}_m \cdot \mathbf{M}_{\mathrm{inc}} dS. \quad (49)$$

The coefficients $c_m^{J/M}$ are the excitation coefficients of the vector $\mathbf{y}$ used in the approximate solution of the direct scattering problem for a given excitation source [Eq. (39)]. Thus the summation in Eq. (47) represents the projection of these coefficients to specific modes with index n.

Expand $\mathbf{f}_n$ as

$$\mathbf{f}_n = \sum_m \left(a_m^{f,n} \mathbf{b}_m, b_m^{f,n} \mathbf{b}_m \right). \quad (50)$$

Then the product $\langle \mathbf{h}_n, \mathbf{f}_n \rangle$ can be written as

$$\langle \mathbf{h}_n, \mathbf{f}_n \rangle = \sum_m \sum_{m'} \left(a_m^{h,n*} a_{m'}^{f,n} + b_m^{h,n*} b_{m'}^{f,n} \right) B_{mm'}. \quad (51)$$

To summarize, the expansion coefficients α_n can be evaluated by the use of Eqs. (47) and (51).

VI. SPHERICAL GEOMETRY: CONNECTION TO MIE THEORY

A. Theory

As an important example, we consider spherical particles. This case can also be analyzed by the Mie theory, where the internal and scattered fields are sought by the separation of variables [47]. This leads to the expansion of the fields in terms of transverse-electric (TE) and transverse-magnetic (TM) multipoles and the resonances arise from the poles of the

expansion coefficients [47]. For boundary integral operators, the solution $\mathbf{f}$ is given in terms of tangential traces of the multipoles over S [54].

In this section, we assume that the surface S of the particle is a sphere of radius a. The surface current densities can be expressed in an orthogonal basis of the Hilbert space $L^2(S)$ spanned by functions $\nabla_t Y_{lm}$ and $\mathbf{n}\times\nabla_t Y_{lm}$, where Y_{lm} are the spherical harmonics. The following properties have been discovered [54]:

$$\mathcal{D}_i \nabla_t Y_{lm} = \alpha_{il}\nabla_t Y_{lm}, \tag{52}$$

$$\mathcal{D}_i \mathbf{n}\times\nabla_t Y_{lm} = \beta_{il}\mathbf{n}\times\nabla_t Y_{lm}, \tag{53}$$

$$\mathcal{K}_i \nabla_t Y_{lm} = \gamma_{il}\mathbf{n}\times\nabla_t Y_{lm}, \tag{54}$$

$$\mathcal{K}_i \mathbf{n}\times\nabla_t Y_{lm} = \gamma_{il}\nabla_t Y_{lm}, \tag{55}$$

where

$$\alpha_{il} = \eta_i \psi_l'(x_i)\xi_l'(x_i), \tag{56}$$

$$\beta_{il} = \eta_i \psi_l(x_i)\xi_l(x_i), \tag{57}$$

$$\gamma_{il} = -i/2[\psi_l(x_i)\xi_l'(x_i) + \xi_l(x_i)\psi_l'(x_i)], \tag{58}$$

where $x_i = k_i a$ and ψ_l, ξ_l are Riccati-Bessel functions [47]. We also define $x = k_1 a$ and $Nx = k_2 a$, where $N = k_2/k_1$ is the relative index of refraction. Thus the vector spherical harmonics are eigenfunctions of $\mathcal{D}_i$ and $\mathbf{n}\times\mathcal{K}_i$.

The expansion of the solution in spherical harmonics is

$$\mathbf{f} = \sum_{l=1}^{\infty}\sum_{m=-l}^{l}(a_{lm}\nabla_t Y_{lm} + b_{lm}\mathbf{n}\times\nabla_t Y_{lm}, \\ c_{lm}\nabla_t Y_{lm} + d_{lm}\mathbf{n}\times\nabla_t Y_{lm}). \tag{59}$$

We seek transverse-electric and transverse-magnetic modes of the form

$$\mathbf{f}_{lm}^{\mathrm{TE}} = (a_l \mathbf{n}\times\nabla_t Y_{lm}, b_l \nabla_t Y_{lm}), \tag{60}$$

$$\mathbf{f}_{lm}^{\mathrm{TM}} = (a_l \nabla_t Y_{lm}, b_l \mathbf{n}\times\nabla_t Y_{lm}). \tag{61}$$

The transversality is apparent from $\nabla_t\cdot\mathbf{J} = i\omega\epsilon_1\mathbf{n}\cdot\mathbf{E}_1$, $\nabla_t\cdot\mathbf{M} = i\omega\mu_1\mathbf{n}\cdot\mathbf{H}_1$, and that $\nabla_t\cdot(\mathbf{n}\times\nabla_t\phi) = 0$ holds for all ϕ.

Operating with $\mathcal{A}$ on the TE field gives rise to the eigenvalue problem $\mathrm{A}\mathbf{x} = \chi\mathbf{x}$, where $\mathbf{x} = (a_l, b_l)^T$ and

$$\mathrm{A} = 2\begin{pmatrix} \xi_\mu(\mu_1\gamma_{1l} - \mu_2\gamma_{2l}) & \xi_\mu(-\epsilon_1\alpha_{1l} + \epsilon_2\alpha_{2l}) \\ \xi_\epsilon(-\epsilon_1\beta_{1l} + \epsilon_2\beta_{2l}) & \xi_\epsilon(-\epsilon_1\gamma_{1l} + \epsilon_2\gamma_{2l}) \end{pmatrix}. \tag{62}$$

The transverse-magnetic fields give rise to a similar eigenvalue problem with matrix

$$\mathrm{A} = 2\begin{pmatrix} \xi_\mu(-\mu_1\gamma_{1l} + \mu_2\gamma_{2l}) & \xi_\mu(-\epsilon_1\beta_{1l} + \epsilon_2\beta_{2l}) \\ \xi_\epsilon(\epsilon_1\alpha_{1l} - \epsilon_2\alpha_{2l}) & \xi_\epsilon(\epsilon_1\gamma_{1l} - \epsilon_2\gamma_{2l}) \end{pmatrix}. \tag{63}$$

Note that a 2×2 matrix always has exactly two eigenvalues, which we do not indicate explicitly in χ. A Müller eigenvalue is then given as $\lambda = 1 + \chi$. Thus we get two eigenvalues for each l in the multipole formalism. This is most likely a manifestation of the fact that the resonance frequencies appear as pairs symmetric with respect to the imaginary axis. Complex resonance frequencies ω_n, which are poles of the inverse operator, are found by solving $\det(\mathrm{I} + \mathrm{A}(\omega_n)) = 0$. Even for a sphere this procedure is iterative by nature.

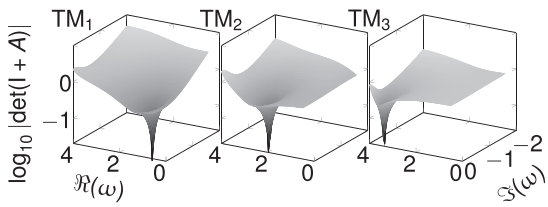

FIG. 3. Plot of the function $\log_{10}|\mathrm{I} + \mathrm{A}(\omega)|$ at complex frequencies for a gold sphere with radius 200 nm. The first three TM modes with $l = 1,2,3$ are considered.

In conclusion, we have the following results:

$$(\mathcal{I} + \mathcal{A})\,\mathbf{f}_{lm}^{\mathrm{TE}} = \lambda_l^{\mathrm{TE}}\mathbf{f}_{lm}^{\mathrm{TE}}, \tag{64}$$

$$(\mathcal{I} + \mathcal{A})\,\mathbf{f}_{lm}^{\mathrm{TM}} = \lambda_l^{\mathrm{TM}}\mathbf{f}_{lm}^{\mathrm{TM}}, \tag{65}$$

i.e., the TE and TM multipolar modes $\mathbf{f}_{lm}^{\mathrm{TE}}$ and $\mathbf{f}_{lm}^{\mathrm{TM}}$ are eigensolutions of Eq. (25). This rigorously links our general theory of modes and resonances to the traditional Mie theory.

B. Results

Consider a gold sphere of radius 200 nm in vacuum. The complex resonance frequencies defined by Eq. (23) can be found with our numerical method. For complex frequencies, we use the Drude model for the permittivity of gold with parameters obtained from fit [55]. Our method shows that the TM modes of order $l = 1,2,3$ are the most important, with resonance frequencies of $\omega_1 = 1.34 - i0.66$ PHz, $\omega_2 = 2.72 - i0.66$ PHz, and $\omega_3 = 3.68 - i0.27$ PHz. These frequencies match the nulls of the respective denominators of the traditional Mie theory, illustrating that Eq. (23) is compatible with it. In Fig. 3 we plot the quantity $\log_{10}|\det(\mathrm{I} + \mathrm{A}(\omega))|$ to illustrate how the poles of the inverse operator occur in our boundary integral approach.

We stress that these resonances were obtained without specifying any incident field. Next we compare these results to the traditional approach that uses an incident probe field. We calculate the extinction spectrum and field enhancement of the sphere for linearly polarized, incident plane-wave and measured permittivity data [56]. The results shown in Fig. 4 are typical for a large sphere: we see a very broad dipole resonance ($l = 1$) and two relatively narrow peaks corresponding to quadrupole ($l = 2$) and octupole ($l = 3$) TM modes. Extinction and field enhancement peaks occur at notably different frequencies, as known for large particles [57]. The frequencies from our theory fall between the ones obtained from extinction and field enhancement. Thus neither

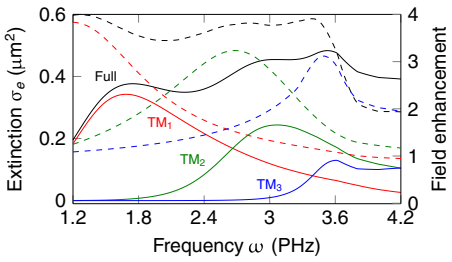

FIG. 4. (Color online) Extinction cross section (solid) and field enhancement (dashed) of a gold sphere with radius 200 nm for a linearly polarized incident plane wave. TM contributions are plotted separately from the full-wave case.

the peaks in extinction nor the peaks in field enhancement should be used to define resonance frequencies.

Next we analyze the eigenvalue spectrum defined by Eq. (25) at a real frequency $\omega = 1.7$ PHz, shown in Fig. 5. We use the analytical equations (64) and (65) and the numerical method of moments applied to Eq. (25) to validate the latter. The eigenvalues computed by the two approaches agree well. The smallest eigenvalues, making possible strong excitation, correspond to the lowest-order modes. Interestingly, the extinction of plane wave is highest due to the dipole mode (TM$_1$), even though its eigenvalue is not the smallest. In addition, the TM$_2$ mode is barely excited in spite of its small eigenvalue. This is possible because coefficients α_n also depend on $\langle \mathbf{h}_n, \mathbf{g} \rangle$, which depends on the form of excitation. Thus the modal approach implies that generally TM$_2$ has a stronger response than TM$_1$, but a plane wave is not optimal for its excitation. Lastly, we clearly observe that the eigenvalues accumulate towards the value 1, which follows directly from the compactness of $\mathcal{A}(\omega)$, as was discussed in Sec. III.

VII. RESONANCES AND MODES OF NONSPHERICAL PARTICLES

The results for the sphere shown in Fig. 4 illustrate that it is very difficult to distinguish individual modes in the extinction spectrum. For spherical particles, we can resort to the multipole expansion, but without our modal theory this is impossible in other geometries. We next demonstrate the power of our approach, without any assumed incident field, by considering prototypical nonspherical structures. We consider three flat gold nanostructures: a circular disk, a disk dimer, and a bar, all with gold thickness of 20 nm. For the disk, we consider the diameters of 120, 160, and 200 nm. For the dimer, we consider the diameter of 120 nm and gap sizes of 20, 40, and 60 nm. For the bar, we consider the width of 120 nm and lengths of 160, 200, and 240 nm.

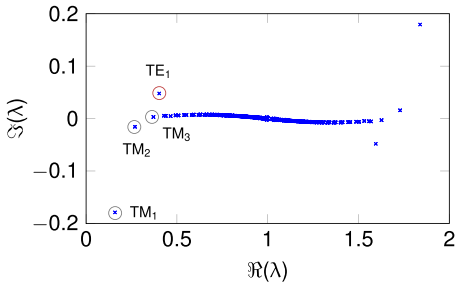

FIG. 5. (Color online) Eigenvalues of I + A at frequency 1.7 PHz for a gold sphere of radius 200 nm. Dots are calculated by method of moments and circles by analytic theory.

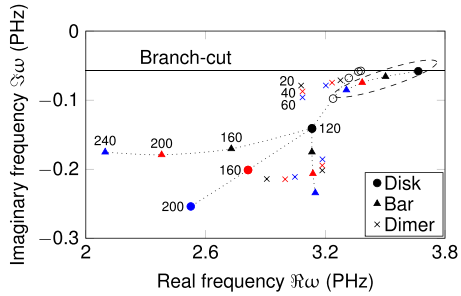

FIG. 6. (Color online) Resonance frequencies in the complex frequency plane. Numbers and colors indicate the varied parameter of particular structure. Dotted lines illustrate the trends in resonance shifts. The degenerate resonance of the disk clearly splits into branches for the bar and dimer. Circles correspond to a down-scaled disk that approaches the quasistatic limit, whence the resonances approach the branch cut. The encircled marks correspond to higher-order resonances.

We utilize the Drude model again to find the complex resonance frequencies of the structures, which are shown in Fig. 6. The resonances exhibit intuitive behavior: increasing particle size or aspect ratio shifts the real part of resonance frequency $\Re\omega_n$ to lower values. The disk resonance is degenerate, but stretching it into a bar splits the resonance into two branches, related to plasmon oscillations along two directions. For the dimer, the degenerate resonances of the two disks produce four branches. This is thus an exact electromagnetic treatment of "mode hybridization" [6,7]. Notice that the resonance frequencies are off the branch cut, where the resonance frequencies are predicted to reside by the quasistatic theory. This emphasizes the importance of radiative effects.

Next we discuss the modes and corresponding radiation patterns, calculated numerically from Eq. (25), at real frequencies close to the complex resonance frequencies of Fig. 6. At each fixed frequency, there is a discrete set of modes, but we only consider a few of those corresponding to lowest-in-magnitude eigenvalues.

In Fig. 7 the modes of the disk of diameter 120 nm at frequency 3.14 PHz are shown. Note that the charge densities for all modes are normalized between -1 and $+1$, as the eigenmodes as such do not have any inherent strength. The first two modes are the typical dipole modes, which are degenerate due to the rotational symmetry. Here the term "dipole mode" is defined rigorously without relying on the multipole theory,

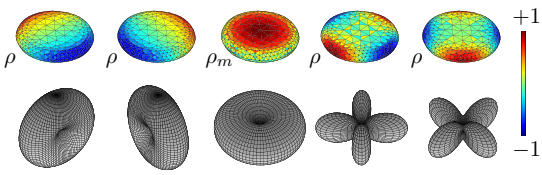

FIG. 7. (Color online) Mode charge densities and radiation patterns at fixed real frequency 3.14 PHz for the gold nanodisk of diameter 120 nm. The charge densities correspond to a time instant of harmonic oscillation and are normalized to unity.

which is strictly defined only for spherical particles. These are plasmon modes that are characterized by accumulating electric surface charge $\rho = \epsilon_0 \mathbf{n} \cdot \mathbf{E}_1$. For the third mode, however, the accumulating quantity is the equivalent surface magnetic charge $\rho_m = \mu_0 \mathbf{n} \cdot \mathbf{H}_1$. Such modes are due to eddy currents and are analogous to TE modes of the sphere. It would be difficult to find such responses by a plane-wave probe field due to polarization mismatch and simultaneous excitation of other modes. The last two modes are again degenerate plasmon modes, but of higher order.

Figure 8 shows the modes of the dimer of gap length 20 nm at frequency 3.14 PHz. The first two modes of the top row are the "dark" hybridized plasmon modes with no radiation along the disk axis. The third mode of the top row and the first mode of the bottom row are the "bright" hybridized plasmon modes. The last two modes of the bottom row are hybridized eddy current, i.e., magnetic modes.

The modes of the bar of length 200 nm at frequency 2.38 PHz are shown in Fig. 9. The first two modes of the top row are the plasmon modes related to oscillation of electrons along the length and width of the bar, respectively. The third mode of the top row is a magnetic mode. The three modes in the bottom row are higher-order plasmon modes, the first two being "dark" and the last being "bright."

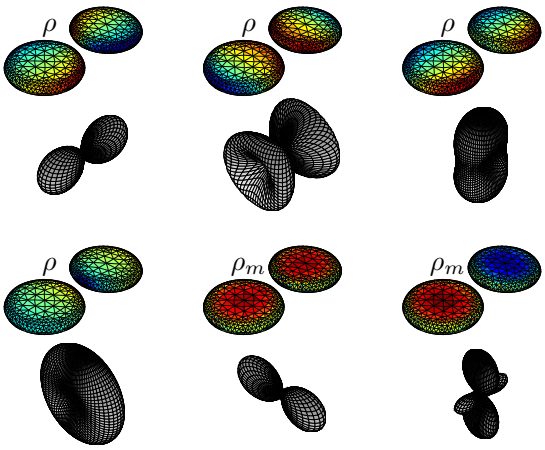

FIG. 8. (Color online) Mode charge densities and radiation patterns at fixed real frequency 3.14 PHz for the gold nanodisk dimer of gap length 20 nm. The color scale is that of Fig. 7.

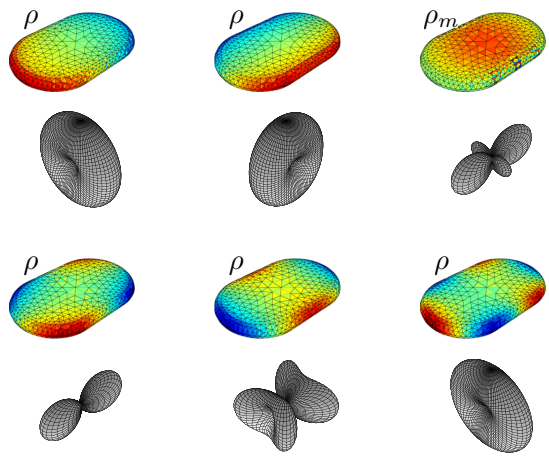

FIG. 9. (Color online) Mode charge densities and radiation patterns at fixed real frequency 2.38 PHz for the gold nanobar dimer of length 200 nm. The color scale is that of Fig. 7.

VIII. DISCUSSION

We now turn to more subtle aspects of our approach. The solution space over S is *separable*, and thus it has a discrete basis (the so-called Schauder basis) [58]. However, it is not yet proven that the eigenmodes $\mathbf{f}_n$ constitute such basis. Nevertheless, we have verified that only a few modes are required to describe typical excited solutions very accurately.

The reason why one obtains an eigenbasis for cavity resonator and waveguide problems is that the governing operator is compact and self-adjoint. The operator K in the quasistatic scattering theory, introduced in Sec. IV B, is also compact and self-adjoint with respect to a certain inner product, which is closely related to energy [59]. In the full-wave scattering problem, the corresponding operator is compact in the Müller formulation, but it is not self-adjoint. The reason for this is that, in the full-wave case, the Green's function is complex valued due to the factor $\exp(ikR)$ as opposed to the static case. This is true for the inner product defined in Eq. (22), but that this is true for any other inner product as well is suggested by the fact that, even for the sphere, the eigenvalues are complex numbers. A prior study of modes for dielectric scatterers considered the PMCHWT formulation, from which a generalized eigenvalue problem was derived [38]. The pertinent operators were pseudo-self-adjoint by construction, but not compact. Thus the full-wave scattering problem may not admit a description by a compact self-adjoint operator.

On the other hand, a discrete basis can be found in the Müller formulation: The Riesz-Schauder theory states that a compact operator has a *singular value decomposition* (SVD) [58]. Thus the range of our operator $\mathcal{A}$ may be rigorously

expanded as

$$\mathcal{A}\mathbf{f} = \sum_{n=1}^{\infty} s_n \langle \mathbf{f}, \mathbf{x}_n \rangle \mathbf{y}_n, \tag{66}$$

where $\mathcal{A}^\dagger \mathcal{A}\mathbf{x}_n = s_n^2 \mathbf{x}_n$ and $\mathcal{A}\mathcal{A}^\dagger \mathbf{y}_n = s_n^2 \mathbf{y}_n$ hold and the numbers s_n are called the singular values. These composite operators are compact because $\mathcal{A}$ is compact, and they are also self-adjoint by construction. Unfortunately, our current understanding is that the singular values s_n are not strictly related to the resonances given by Eq. (23).

The modes and resonances of scatterers have been studied by various integral operator approaches, especially for perfectly conducting bodies. It is interesting how the different formulations lead to different operator properties, allowing resonances to be rigorously identified in one formulation but not in the other. We believe that the resonances, as defined by Eq. (23), are the true physical resonances and any other formulation of the scattering problem should be able to find these. Other formulations may predict additional nonphysical resonances, which is known to happen for, e.g., the electric field integral equation (EFIE) and magnetic field integral equation (MFIE) formulations [49].

As we discussed above, even in the Müller formulation, we may define modes in several ways: as eigenfunctions of the operator $\mathcal{I} + \mathcal{A}(\omega)$ at fixed real frequency, as eigenfunctions $\mathbf{f}_{0n}$ corresponding to the complex resonance frequencies ω_n by $(\mathcal{I} + \mathcal{A}(\omega_n))\mathbf{f}_{0n}$, or as eigenfunctions $\mathbf{y}_n$ appearing in the SVD for a fixed real frequency. On the other hand, in, e.g., the volume integral operator formulation, the domain of the eigenfunctions is the volume of the particle as opposed to the surface in the boundary integral formulation. It is not clear whether these modes map to each other in a trivial way. We feel that understanding the relation between different mode definitions is an open issue that should be investigated in the future.

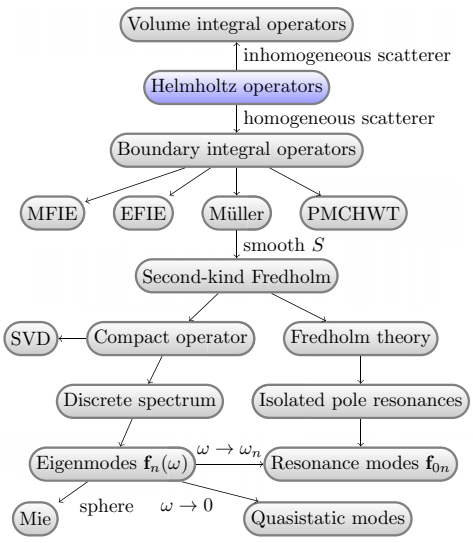

FIG. 10. (Color online) Diagram of the strategy towards the definition of modes and resonances in scattering problems by boundary integral operators.

The various formulations of the scattering problem are illustrated in Fig. 10. For the boundary integral approach, various formulations exist and only a few of them are listed. We emphasize that the Müller formulation leads to theoretically the most rigorous approach to the definition of modes and resonances.

IX. CONCLUSION

We have successfully defined modes and resonances for dielectric and plasmonic scatterers by the use of boundary integral operators in a full-wave approach. We concluded that the Müller formulation admits a rigorous definition of the resonances as properties of the scatterer by relying on the second-kind Fredholm property of the pertinent boundary integral operator. The Fredholm theory allowed us to establish that the resonance frequencies are isolated points in the complex plane, and any other singularities are the possible branch cuts from the material dispersion relation. We further proposed an expansion of solutions with respect to eigenmodes, which are independent of incident field and defined at fixed real frequencies. The second-kind Fredholm property guaranteed the discreteness of the modal expansion as well.

The modes and resonances were connected to the traditional Mie theory in the case of spherical particles. This was accomplished by proving that the boundary restrictions of the multipole fields are eigenfunctions of the considered boundary integral operator. We also showed that the general definition of modes naturally reduced to the earlier quasistatic definitions in the limit of zero frequency.

We presented illustrative examples for the sphere and for nonspherical flat gold nanostructures. The resonance frequencies were found to obey intuitive shifting and splitting behaviors as the geometrical parameters were varied. The near fields and radiation patterns of the corresponding modes at real frequencies were presented and analyzed. The modes were characterized as bright or dark modes and further classified as plasmon or eddy current modes.

In conclusion, our theory provides a unifying framework for the analysis of resonances as well as near and far fields in scattering problems. The approach reveals the important physics of scattering systems directly and can fundamentally change the way these systems are optimized and understood. The present paper has considered plasmonic systems as an example of particular interest. However, the approach is applicable to any material describable by complex permittivity and permeability. Such materials are constantly emerging for nanophotonic applications.

ACKNOWLEDGMENTS

The authors thank Prof. Ralf Hiptmair for assistance with the integral operator theory and Dr. Pasi Ylä-Oijala for helpful advice regarding boundary integral operators. J.M. acknowledges the graduate school of Tampere University of Technology for funding.

[1] U. Kreibig and M. Vollmer, *Optical Properties of Metal Clusters* (Springer-Verlag, Berlin, 1995).

[2] J. Jackson, S. Westcott, L. Hirsch, J. West, and N. Halas, Appl. Phys. Lett. **82**, 257 (2003).

[3] K. Li, M. I. Stockman, and D. J. Bergman, Phys. Rev. B **72**, 153401 (2005).

[4] K. L. Kelly, E. Coronado, L. L. Zhao, and G. C. Schatz, J. Phys. Chem. B **107**, 668 (2003).

[5] M.-W. Chu, V. Myroshnychenko, C. H. Chen, J.-P. Deng, C.-Y. Mou, and F. J. García de Abajo, Nano Lett. **9**, 399 (2008).

[6] E. Prodan, C. Radloff, N. J. Halas, and P. Nordlander, Science **302**, 419 (2003).

[7] P. Nordlander, C. Oubre, E. Prodan, K. Li, and M. Stockman, Nano Lett. **4**, 899 (2004).

[8] D. R. Fredkin and I. D. Mayergoyz, Phys. Rev. Lett. **91**, 253902 (2003).

[9] I. D. Mayergoyz, D. R. Fredkin, and Z. Zhang, Phys. Rev. B **72**, 155412 (2005).

[10] D. E. Gomez, K. C. Vernon, and T. J. Davis, Phys. Rev. B **81**, 075414 (2010).

[11] K. Li, M. I. Stockman, and D. J. Bergman, Phys. Rev. Lett. **91**, 227402 (2003).

[12] M. I. Stockman, S. V. Faleev, and D. J. Bergman, Phys. Rev. Lett. **87**, 167401 (2001).

[13] C. E. Baum, On the Singularity Expansion Method for the Solution of Electromagnetic Interaction Problems, Tech. Rep., DTIC Document, 1971 (unpublished), http://www.dtic.mil/docs/citations/ADA066905.

[14] R. Garbacz and R. Turpin, IEEE Trans. Antennas Propag. **19**, 348 (1971).

[15] R. Harrington and J. Mautz, IEEE Trans. Antennas Propag. **19**, 622 (1971).

[16] R. Harrington and J. Mautz, IEEE Trans. Antennas Propag. **19**, 629 (1971).

[17] M. Capek, P. Hazdra, and J. Eichler, IEEE Trans. Antennas Propag. **60**, 4556 (2012).

[18] R. Harrington, J. Mautz, and Y. Chang, IEEE Trans. Antennas Propag. **20**, 194 (1972).

[19] D. J. Bergman and D. Stroud, Phys. Rev. B **22**, 3527 (1980).

[20] G. Hanson and C. Baum, Interaction Note 517 (1996), http://www.ece.unm.edu/summa/notes/Interaction.html.

[21] J. R. de Lasson, J. Mørk, and P. T. Kristensen, J. Opt. Soc. Am. B **30**, 1996 (2013).

[22] X. Zheng, V. Volskiy, V. K. Valev, G. A. Vandenbosch, and V. V. Moshchalkov, IEEE J. Sel. Top. Quantum Electron. **19**, 4600908 (2013).

[23] X. Zheng, N. Verellen, V. Volskiy, V. K. Valev, J. J. Baumberg, G. A. Vandenbosch, and V. V. Moshchalkov, Opt. Express **21**, 31105 (2013).

[24] N. Budko and A. Samokhin, SIAM J. Sci. Comp. **28**, 682 (2006).

[25] N. V. Budko and A. B. Samokhin, Phys. Rev. Lett. **96**, 023904 (2006).

[26] Y. Zhou, Ph.D. thesis, Harvard University, 2010.

[27] V. A. Markel, J. Opt. Soc. Am. B **12**, 1783 (1995).

[28] N. A. Gippius, T. Weiss, S. G. Tikhodeev, and H. Giessen, Opt. Express **18**, 7569 (2010).

[29] T. Weiss, N. Gippius, S. Tikhodeev, G. Granet, and H. Giessen, J. Opt. Soc. Am. A **28**, 238 (2011).

[30] H. Guo, B. Oswald, and P. Arbenz, Opt. Express **20**, 5481 (2012).

[31] Q. Bai, M. Perrin, C. Sauvan, J.-P. Hugonin, and P. Lalanne, Opt. Express **21**, 27371 (2013).

[32] F. J. de Abajo and A. Howie, Phys. Rev. B **65**, 115418 (2002).

[33] G. W. Bryant, F. J. García de Abajo, and J. Aizpurua, Nano Lett. **8**, 631 (2008).

[34] A. M. Kern and O. J. Martin, J. Opt. Soc. Am. A **26**, 732 (2009).

[35] C. Forestiere, G. Iadarola, G. Rubinacci, A. Tamburrino, L. Dal Negro, and G. Miano, J. Opt. Soc. Am. A **29**, 2314 (2012).

[36] J. Mäkitalo, S. Suuriniemi, and M. Kauranen, Opt. Express **19**, 23386 (2011).

[37] P. Heider, Comput. Math. Appl. **60**, 1620 (2010).

[38] Y. Chang and R. Harrington, IEEE Trans. Antennas Propag. **25**, 789 (1977).

[39] C. Sauvan, J.-P. Hugonin, I. S. Maksymov, and P. Lalanne, Phys. Rev. Lett. **110**, 237401 (2013).

[40] P. T. Kristensen and S. Hughes, ACS Photonics **1**, 2 (2014).

[41] L. Novotny and B. Hecht, *Principles of Nano-optics* (Cambridge University Press, Cambridge, UK, 2006).

[42] J. A. Stratton, *Electromagnetic Theory* (McGraw-Hill College, New York, 1941).

[43] C. Müller, *Foundations of the Mathematical Theory of Electromagnetic Waves* (Springer-Verlag, Berlin, 1969).

[44] P. Ylä-Oijala and M. Taskinen, IEEE Trans. Antennas Propag. **53**, 3316 (2005).

[45] G. W. Hanson and A. B. Yakovlev, *Operator Theory for Electromagnetics: An Introduction* (Springer, New York, 2001).

[46] S. Steinberg, Arch. Rational Mech. Anal. **31**, 372 (1968).

[47] C. F. Bohren and D. R. Huffman, *Absorption and Scattering of Light by Small Particles* (John Wiley & Sons, New York, 2008).

[48] D. Giri and F. Tesche, Electromagnetics **1**, 455 (1981).

[49] R. F. Harrington, J. Electromagnet. Wave. **3**, 1 (1989).

[50] R. F. Harrington, *Field Computation by Moment Methods* (Wiley-IEEE Press, New York, 1993).

[51] S. Rao, D. Wilton, and A. Glisson, IEEE Trans. Antennas Propag. **30**, 409 (1982).

[52] I. Hänninen, M. Taskinen, and J. Sarvas, Prog. Electromagn. Res. **63**, 243 (2006).

[53] P. Ylä-Oijala, S. Kiminki, K. Cools, F. Andriulli, and S. Järvenpää, Int. J. Numer. Model. **25**, 525 (2012).

[54] G. C. Hsiao and R. E. Kleinman, IEEE Trans. Antennas Propag. **45**, 316 (1997).

[55] A. Vial, A.-S. Grimault, D. Macías, D. Barchiesi, and M. L. de la Chapelle, Phys. Rev. B **71**, 085416 (2005).

[56] P. B. Johnson and R. Christy, Phys. Rev. B **6**, 4370 (1972).

[57] B. M. Ross and L. P. Lee, Opt. Lett. **34**, 896 (2009).

[58] M. Reed and B. Simon, *Methods of Modern Mathematical Physics: Functional Analysis* (Gulf Professional Publishing, Houston, TX, 1980), Vol. 1.

[59] I. D. Mayergoyz, *Plasmon Resonances in Nanoparticles* (World Scientific, Singapore, 2013).

Publication III

Reprinted with permission from

J. Mäkitalo, S. Suuriniemi and M. Kauranen. Enforcing symmetries in boundary element formulation of plasmonic and second-harmonic scattering problems. Journal of the Optical Society of America A, **31**, 2821 – 2832 (2014).

Publication IV

Reprinted with permission from

G. Bautista, M. J. Huttunen, J. Mäkitalo, J. M. Kontio, J. Simonen and M. Kauranen. Second-harmonic generation imaging of metal nano-objects with cylindrical vector beams. Nano Letters, **12**, 3207–3212 (2012).

NANO LETTERS

Letter

pubs.acs.org/NanoLett

Second-Harmonic Generation Imaging of Metal Nano-Objects with Cylindrical Vector Beams

Godofredo Bautista,*[,†] Mikko J. Huttunen,[†] Jouni Mäkitalo,[†] Juha M. Kontio,[‡] Janne Simonen,[‡] and Martti Kauranen[†]

[†]Department of Physics and [‡]Optoelectronics Research Center, Tampere University of Technology, Tampere, Finland

Supporting Information

ABSTRACT: We introduce an imaging technique based on second-harmonic generation with cylindrical vector beams that is extremely sensitive to three-dimensional orientation and nanoscale morphology of metal nano-objects. Our experiments and second-harmonic field calculations based on frequency-domain boundary element method are in very good agreement. The technique provides contrast for structural features that cannot be resolved by linear techniques or conventional states of polarization and shows great potential for simple and cost-effective far-field optical imaging in plasmonics.

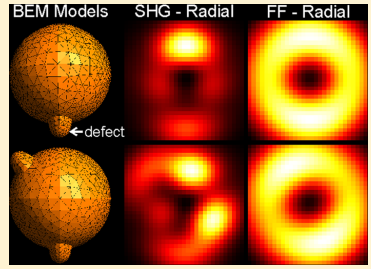

KEYWORDS: *Metal nano-object, second-harmonic generation, cylindrical vector beams, nonlinear microscopy, boundary element method, plasmonics*

The linear optical response of metal nano-objects is mostly governed by the lightning-rod effect and localized surface plasmon (LSP) resonances.[1] The lightning-rod effect arises from the fact that the electric charges accumulate at the geometrically sharp and pointed features of metal structures. Such accumulation is primarily driven by the electric field polarized along the tip axis.[2] On the other hand, the LSP resonances arise from collective oscillations of electrons in the nano-objects and are more sensitive to the excitation wavelength. Furthermore, they depend on the properties of the nano-objects, such as type of metal and geometry, and the properties of the surrounding medium.[1] In addition, they can be controlled by particle interactions, for example, the interparticle distance in an array,[3] by the relative particle orientation in dimers,[4] and by Fano resonances.[5−7]

Imaging metal nano-objects poses a demanding task due to their nanoscale dimensions. Scanning electron microscopy (SEM) and atomic force microscopy (AFM) have been typically used to directly inspect their morphology. Additionally, electron energy-loss spectroscopy,[8] cathodoluminescence,[9] near-field scanning optical microscopy,[10] photoemission electron microscopy,[11] tip-enhanced photoluminescence[12,13] and similar near-field modalities[14,15] have been applied to map the distribution of LSPs and the resulting local-field enhancements. Although such techniques provide high-resolution imaging, their implementation requires complicated instrumentation. Alternatively, far-field microscopy schemes exploiting linear and nonlinear optical processes have been demonstrated. The use of nonlinear optical processes has an advantage in terms of resolution and provides additional sources of contrast due to multiphoton interactions. Furthermore, these multiphoton processes may even be amplified by the strong local fields generated in the vicinity of metal nano-objects. Such techniques have been demonstrated using two-photon excited luminescence,[16] nonlinear four-wave mixing,[17] and harmonic generation.[18−23]

Of the far-field nonlinear techniques, second-harmonic generation (SHG), which is the conversion of the incident optical field at frequency ω to the second-harmonic field at frequency 2ω, is the simplest and most common. In recent years, SHG has been used to characterize various metal nano-objects such as nanodots,[24] L-shaped nanoparticles,[25,26] T-shaped nanodimers,[27] split-ring resonators,[28] G-shaped nanostructures,[29] twisted-cross nanodimers,[30] and sharp tips.[12,13,31] The main advantages of SHG lie in the added sensitivity toward local fundamental fields due to the nonlinear interaction and in its sensitivity to structural symmetry.[1] Moreover, it has been shown that subwavelength-sized deformations from ideal structures can lead to undesired symmetry breakings and thus affect the overall nonlinear responses.[19,32−37] This structural sensitivity is very hard to achieve using other optical techniques.

Simultaneously, there has been growing interest in polarization beam shaping particularly for doughnut-shaped cylindrical vector beams (CVBs) with azimuthal (AP) and radial polarizations (RP).[38] When these beams are focused, the intensity distributions of their transverse electric-field components preserve the doughnut-shaped intensity patterns and

Received: March 28, 2012
Revised: May 14, 2012
Published: May 15, 2012

corresponding polarizations.[1,39] However when all the electric-field components are considered, the RP beam focus exhibits a Gaussian-like intensity distribution due to the presence of a strong field component along the optical axis, usually referred to as longitudinal component.[40] Although AP and RP beams have been shown to be versatile orientation probes in far-field optical microscopy of single molecules,[41] nanocrystals[42,43] and metal nanoparticles,[44,45] these reports are mainly restricted to the use of linear optical processes. On the other hand, SHG microscopy using RP beams has been demonstrated for orientation imaging of biological structures.[46]

In this Letter, we show that SHG with focused CVBs is extremely sensitive to the three-dimensional (3D) orientation and morphology of metal nano-objects. To verify this technique, we image the SHG intensity distribution in individual subwavelength-sized gold nanobumps and nanocones using focused AP and RP beams. To understand the experimental SHG images, we provide SHG field calculations based on the frequency-domain boundary element method (BEM). The technique is shown to provide contrast for structural features that cannot be discriminated by linear techniques or conventional states of polarization.

Arrays of gold nanobumps and nanocones with different particle-to-particle distances were fabricated on glass substrates using ultraviolet-nanoimprint lithography (UV-NIL) combined with electron-beam evaporation.[31] The master template was fabricated on a silicon wafer using electron-beam lithography. The resulting patterns on the template were then transferred to polydimethylsiloxane stamp. Next, a glass substrate was coated with a 600 nm thick poly(methyl methacrylate) film, a germanium intermediate layer, and a UV-NIL resist layer (Amonil, AMO GmbH). A mask aligner (EVG 620) using the PDMS stamp was then used for nanoimprinting. Reactive ion etching was used to form cylindrical hole patterns in the resist exposing the substrate surface. Next, layers of titanium adhesion (20 nm) and gold (100−400 nm) were deposited using an electron-beam evaporator. Depending on the amount of the gold used in the evaporation, nanobumps (height ∼ 100 nm) or nanocones (height ∼ 300−400 nm) can be fabricated. Lastly, lift-off was performed in Microposit Remover 1165 resist stripper (Shipley Co.) with ultrasonic agitation. Shown in Figure 1a is a SEM image of a region in the fabricated array of gold nanobumps with a period of 2 μm. A SEM image of a nanobump with a base diameter of 160 nm and a height of 80 nm is depicted in Figure 1b. The residual in-plane anisotropy of the nanobump is used for sensitive 2D orientation imaging using SHG with CVBs. On the other hand, a SEM image of a nanocone with a base diameter of 150 nm, a height of 300 nm, and a tip diameter of 20 nm is shown in Figure 1c. The resulting conical geometry is used for 3D orientation imaging as well as field localization.

To characterize the nano-objects, we used a custom-built stage-scanning SHG microscope operating in reflection. A mode-locked femtosecond Nd:glass laser (wavelength 1060 nm, pulse length 200 fs, repetition rate 82 MHz) was used for excitation. Upon polarization cleaning, collimation and expansion, the output beam was directed to the back-aperture of an infinity-corrected (50×, 0.8 NA) and strain-free microscope objective. The objective was used to focus the beam onto the sample which is mounted on a three-axis motorized translation stage. The reflected fundamental and SHG signals were collected by the same objective and spectrally discriminated by a dichroic mirror. To extract the backscattered

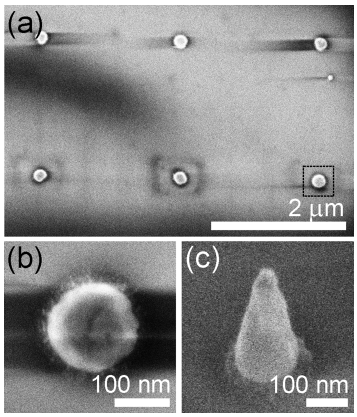

Figure 1. (a) SEM image of an array of gold nanobumps on glass in top view. Close-up SEM images of the (b) gold nanobump in the boxed region in panel a and (c) a gold nanocone in oblique view.

SHG signal, appropriate optical filters, a tube lens and a cooled photomultiplier tube were used. The SHG origin of the signal was verified before imaging by measuring the quadratic dependence of the signal on the laser intensity. A bright-field imaging arm was also implemented to view the sample area of interest. The 800 nm diameter of the beam focus permitted us to collect signals from individual nanoparticles that are free from coupling effects due to indirect excitation of neighboring particles.[47] Moreover, the spot size used was always smaller than the period of the imaged arrays. To achieve AP or RP laser beams with high polarization purity, a radial polarization converter (ARCoptix, S.A.) and a spatial filter in tandem before the dichroic filter were used. Throughout the imaging experiments, average power levels of less than 5 mW were used. The power levels were verified to be below the damage threshold of the samples by comparing the SEM images acquired before and after SHG imaging.

To address the origin of the SHG response from the nanobumps and nanocones, we performed surface SHG modeling based on the frequency-domain BEM.[48] Here, the electromagnetic scattering problem was formulated by using the Stratton−Chu integral operators and by enforcing the interface conditions on the particle surface. To obtain approximate solutions, the problem was discretized by using the Method of Moments with Galerkin's testing. The Rao−Wilton−Glisson basis functions were chosen meaning that the particle surface was described by a triangle mesh and the representation of the tangential components of the electric and magnetic fields on the surface was of first order.

BEM allows a focused beam to be used as an excitation source. Furthermore, the construction and factorization of the dense system matrix, which are the most time-consuming parts of the method, were done only once per beam scan image. When the beam location was shifted, only the source vector needed to be re-evaluated. Thus the measured beam scan images could be simulated within reasonable computation times. In the computations, the measured refractive index of gold reported by Johnson and Christy was used.[49] The surrounding medium was taken to be vacuum and for simplicity, the substrate was neglected. The far-field optical images for a nanobump and a nanocone with different

morphologies were calculated at the fundamental and second-harmonic frequencies. The signal was collected in reflection as the beam was scanned over a 1.5 × 1.5 μm^2 sized area centered on the particle. The NA was set to 0.8 and the filling factor was set to 1. To qualitatively represent an ideal particle, the dimensions of the nanobump and nanocone triangle meshes were deduced from the SEM and AFM measurements.

For comparison, we also acquired SHG images of the array depicted in Figure 1a using a linearly polarized (LP) beam (Figure 2a). At the location of the nanobumps, single bright

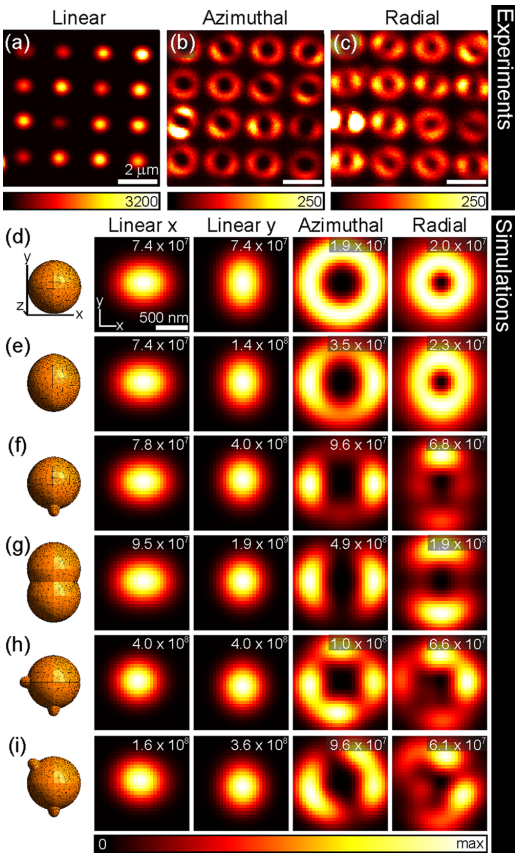

Figure 2. Experimental SHG images of gold nanobumps using focused (a) LP, (b) AP, and (c) RP beams. Calculated far-field SHG images of an (d) ideal nanobump, (e) nanobump with asymmetric base, and (f–i) nanobumps with a bump defect at different configurations using focused LP along *x*, LP along *y*, AP, and RP beams. The calculated images are normalized to the incident beam amplitude and their maximum intensity values (au) are shown. The different triangle meshes used in the calculations are also shown.

spots are seen, which are associated with the excitation of LSPs that oscillate at the plane of the nanobump base. These in-plane LSP oscillations are induced by the transverse field components of the focused LP beam, which is dominantly polarized along the polarization direction of the unfocused beam. Although the observed variations of the SHG intensity levels can indicate possible anisotropy due to the noncircular base, it is difficult to distinguish the direction of in-plane anisotropy of the individual nanobumps based on a single image using a LP beam. Conventionally, the in-plane orientation of an anisotropic nano-object, for example, a nanorod, can be inferred from several images acquired by varying the polarization direction of the LP beam with the additional costs in measurement time and image processing.

Shown in Figures 2b and 2c are the SHG images of the same region using focused AP and RP beams. At the exact location of the nanobumps, dark spots were observed due to the lack of exciting transverse field components of the focused beams. In addition, the absence of SHG intensities at the exact location of the nanobumps using the focused RP beam implied that the excited out-of-plane LSP oscillations did not lead to significant SHG at the chosen excitation wavelength, due to the bluntness of the tips of the nanobumps resulting in small and relatively weak local-field enhancements. This is in contrast with conical structures with sharp tips, where the longitudinal field component of the focused RP beam couples strongly with the tip axis.[2] Thus, doughnut-shaped intensity patterns which surround the dark spots are expected when an ideal nanobump is imaged by focused CVBs. However, for AP excitation, we also observed doughnut-shaped intensity patterns with two enhanced lobes that surround the dark spot. Similar patterns rotated by 90° were evident in the SHG images using the RP beam. We associated these patterns with possible in-plane anisotropy of the nanobump base.

We then calculated the SHG far-field images for an ideal nanobump and nanobumps with varied morphologies under focused LP, AP and RP beams (Figures 2d–i). For the ideal nanobump (Figure 2d), a height of 80 nm and a circular base with diameter of 160 nm was chosen corresponding to an average fabricated nanobump. For the defective nanobump cases, we considered nanobumps with an asymmetric base (Figure 2e) and nanobumps with a small defect at different configurations (Figures 2f–i). For the nanobump with asymmetric base, a height of 80 nm and an ellipsoidal base with a length ratio of 1.1 of the major (176 nm) and minor axes (160 nm) was selected. For the nanobump with a small defect, a small bump positioned at one side of the ideal nanobump was used (Figure 2f). To demonstrate the effect of defect size, an additional nanobump case with a large bump (Figure 2g) defect was used. To examine the role of multiple sources of anisotropy that contribute to symmetry breaking, two nanobumps with two small and same-sized defects that are locally positioned at the base of the nanobump were used. Both of these nanobumps exhibit a small bump positioned at one side of the ideal nanobump along the *y*-axis and differ only in the position of the second small bump. Here, we only considered the cases where the symmetry planes differ by 22.5° with respect to the *z*-axis (Figures 2h and 2i).

The different nanobump cases are distinguished poorly by a focused LP beam with strong polarizations along the *x*- and *y*-axes. Although the use of a focused LP beam with strong polarization along the *y*-axis changed slightly the maximum intensity values and Gaussian-like images, a single SHG image using a focused LP beam is not sufficient to discriminate ideal and defective nanobumps. Moreover with LP, the ellipticity of the image is in the range of 0–19%, where the actual value will be difficult to distinguish in practice.

Under focused CVBs however, the ideal and defective nanobumps are clearly discriminated. The SHG images of an

dx.doi.org/10.1021/nl301190x | *Nano Lett.* 2012, 12, 3207–3212

ideal nanobump resemble perfect doughnut-shaped patterns (Figure 2d) as expected from the radial symmetry of the CVBs and the highly symmetric nanobump. Moreover due to nonlinear effects, the SHG images appeared to have narrower line widths than the scattering images obtained at the fundamental wavelength (Supporting Information).[18] On the other hand, the SHG images of the defective nanobumps (Figures 2e–i) corresponded to asymmetric and distorted doughnut-shaped images, which can be correlated with the properties and location of the defect.

When a nanobump with asymmetric base with a major axis along the *y*-axis (Figure 2e) is considered, the AP and RP beams resulted in different images, which indicated the presence of in-plane anisotropy at the nanobump base along the *y*-axis. Furthermore due to the radial symmetry of the CVBs, it is expected that a nanobump with asymmetric base with a major axis along the *x*-axis results in similar SHG images that are perpendicular to the previous case (Supporting Information). For an asymmetric nanobump imaged by AP (RP) beam, the line segment connecting the two enhanced lobes in the doughnut-shaped SHG image was found to be oriented perpendicular (parallel) to its longer axis. Similar images were observed for a highly anisotropic structure as exemplified by a nanorod with an in-plane aspect ratio of 2 (Supporting Information). Analogously for a metal nanorod imaged by a focused AP (RP) beam under linear excitation, the line segment connecting the two intensity lobes was found to be oriented perpendicular (parallel) to its longer axis.[44,45] Although low degrees of in-plane asymmetry can be also seen under linear scattering with CVBs (Supporting Information), the inherent properties of SHG with CVBs can provide more sensitivity for microscopy as we will show in the following discussions.

When a nanobump with a small bump positioned at one side of the ideal nanobump along the *y*-axis was considered (Figure 2f), the AP and RP beams yielded very distinctive SHG images agreeing well with the SHG experiment. Similarly, due to the radial symmetry of the CVBs, a nanobump with a small bump positioned along the *x*-axis produced asymmetric doughnut-shaped SHG images rotated by 90° (Supporting Information). Again, the line segment connecting the two enhanced lobes in the doughnut-shaped SHG images using the AP (RP) beam indicated the shorter (longer) axis of the nanobump. Moreover, the unequal intensities of the enhanced lobes indicated the presence of a clear defect at the nanobump base, which modified the expected SHG signals. We further note that the asymmetries in the enhanced lobes are affected by the size of the bump defect. At the extreme case where the bump defect is as large as the original bump (Figure 2g), the SHG images would resemble the response of an asymmetric nanoparticle similar to a rod.

At this point, we emphasize that other kinds of shape variations and defects in the nanobumps can cause additional deviations from the expected SHG patterns due to the shifts in the LSP resonances (Figures 2h and 2i). However, based on these results, nanobumps with the considered morphologies can be well resolved by SHG microscopy with CVBs. Such capability will be essentially impossible to achieve without introducing nonlinearity in the excitation scheme with CVBs (Supporting Information).

Next, we imaged nanocones using SHG microscopy. The SHG images of the nanocone in Figure 1c using AP and RP beams are shown in Figures 3a and 3b, respectively. The SHG

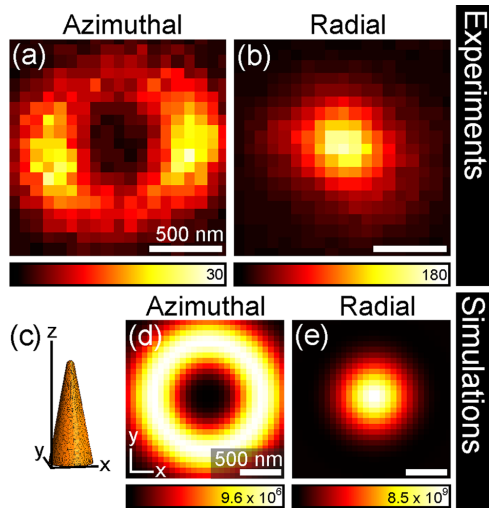

Figure 3. Experimental SHG images of a gold nanocone in Figure 1c using focused (a) AP and (b) RP beams. The triangle mesh used for the ideal nanocone is shown in (c). Calculated far-field SHG images of an ideal nanocone using focused (d) AP and (e) RP beams. The calculated images are separately normalized to the incident beam amplitude and their maximum intensity values (au) are shown.

image of the nanocone using the AP beam resulted in a doughnut-shaped intensity pattern. The slight asymmetry of the SHG pattern was attributed to anisotropy and defects at the nanocone base. On the other hand, the SHG image using the RP beam gave rise to a Gaussian-like image centered at the location of the nanocone. The SHG signals are associated with the excitation of LSPs along the cone axis further strengthened by the lightning-rod effect. The experimental SHG images agreed well with the calculated SHG images (Figures 3d and 3e). In the calculations, a triangle mesh for an ideal nanocone with a height of 300 nm, a tip diameter of 20 nm and a circular base with diameter of 150 nm was used. Additionally, we note that the cone functions as a probe of the fields polarized along the cone axis and the resulting image distribution arises from the SHG signal of an effective dipole oriented along the cone axis as verified previously.[21]

We then tested the sensitivity of the imaging technique to nanocones with different orientation and morphology (Supporting Information). Shown in Figure 4a is a SEM image of an array of nanocones with a period of 2 μm with labels that indicate representative cases of normal (C2, C3, C4, C5, and C7) and bent nanocones (C1 and C6). SHG microscopy images of the chosen region using AP and RP beams are depicted in Figures 4d and 4e, respectively. Focusing an AP beam led to doughnut-shaped intensity patterns surrounding the nanocones (Figure 4d). As noted earlier, the asymmetry in the doughnut-shaped patterns using an AP beam indicates in-plane anisotropy of the nanocone base. Furthermore, the variation in the collected signals suggests the influence of the SHG response that arises from the coupling of the transverse field components of the AP focus to other sources of in-plane anisotropy such as bent tips as seen in the SHG images of the bent nanocones.

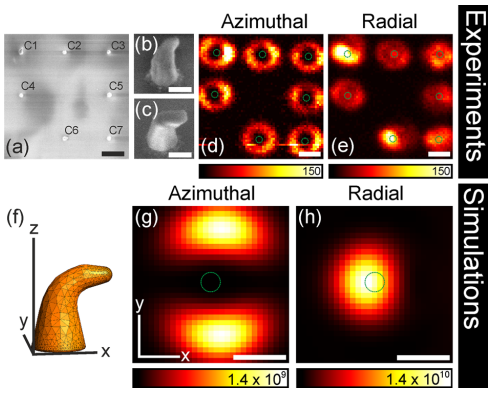

Figure 4. (a) Top view SEM image of a region in the fabricated array of gold nanocones. Oblique SEM images of bent nanocones (b) C1 and (c) C6. SHG images of the same region using focused (d) AP and (e) RP beams. The triangle mesh used for the bent nanocone is shown in (f). Calculated far-field SHG images of bent nanocone using focused (g) AP and (h) RP beams. The calculated images are separately normalized to the incident beam amplitude and their maximum intensity values (au) are shown. The length of the scale bars corresponds to (a,d,e) 1 μm, (b,c) 150 nm, and (g,h) 500 nm. For clarity, the locations of the nanocones are marked with green circles in (d,e,g,h).

On the other hand, focusing a RP beam resulted in varying SHG intensity patterns (Figure 4e). As discussed earlier, nonvanishing intensities at the exact location of the nanocones are observed due to the excitation of LSPs along the nanocone axis. However, the observed variation in the SHG intensities indicates possible shifts in the LSPs of the individual nanocones due to differences in height (Supporting Information). Upon verification using AFM, the heights of nanocones C1, C2, C3, C4, C5, C6, and C7 were found to be 206, 452, 302, 426, 360, 235, and 352 nm, respectively. Furthermore, the collected signals may be influenced by differences in tip sharpness, presence of defects near the tips, and in-plane anisotropy of the nanocones that distort the expected SHG images. In addition, the SHG signals from the bent nanocones under a RP focus were found to be stronger than the other cones (~1 order of magnitude), suggesting the excitation of polarization dependent resonances of the bent cones under inhomogeneous field distributions (Supporting Information).

In order to provide understanding of the results in Figures 4d and 4e, we simulated the SHG responses from a bent nanocone. We used the nanocone model with the height of 300 nm and a slightly larger tip diameter (~40 nm) that is deformed in the *x*-direction. By considering the case of such lowered symmetry, we predict the occurrence of polarization dependent resonances, not present in the ideal cone (Supporting Information). The calculated SHG image of the bent nanocone using the AP beam yielded two asymmetric lobes due to coupling of the transverse fields with the LSPs of the bent nanocone and agreed well with experiment (Figure 4g). The calculated SHG image using the RP beam, on the other hand, resulted in an asymmetric Gaussian-shaped image (Figure 4h) where the hotspot is locally shifted away from the bent tip and agreed well with the experiment. The inhomogeneous field distribution of a focused RP beam is expected to be more sensitive to the location and features of the bent nanocone than the transverse field distribution of a focused AP beam. Thus depending on the morphology and location of the bent nanocones under the RP beam focus, polarization-dependent LSP oscillations that contribute to the overall SHG response are excited (Supporting Information). Nevertheless, we emphasize that the imaging technique is very sensitive to the 3D orientation and morphology of the metal nano-objects. Generally, by comparing the simulated scattering images of the nanocone at the fundamental and second-harmonic wavelengths, we see that the latter ones have more contrast to them (Supporting Information). Therefore, the technique provides contrast for structural features that cannot be resolved by linear techniques or conventional states of polarization.

In conclusion, we have demonstrated an imaging technique that is extremely sensitive to the 3D orientation and morphology of individual metal nano-objects. Our method is based on SHG microscopy using CVBs. We correlated our SHG experiments with SEM images and performed second-harmonic field calculations based on frequency-domain BEM. The experimental results agree well with calculations. Our technique allows precise characterization of individual nano-objects in the far-field, which provides an alternative to complicated near-field approaches. In addition, we emphasize that independent of the quantitative analysis the real value of our experimental technique arises from the fact that its qualitative properties provide information that is not available from alternative techniques. Furthermore, the technique opens additional avenues for subwavelength field shaping in the vicinity of plasmonic nanostructures[30] and furthers optimization of fabrication models and nanoparticle architectures with distinct and tailorable plasmonic properties.[25]

■ ASSOCIATED CONTENT

Supporting Information

Additional discussions related to the experiments and SHG modeling based on BEM for the nanobumps and nanocones are provided. This material is available free of charge via the Internet at http://pubs.acs.org.

■ AUTHOR INFORMATION

Corresponding Author

*E-mail: godofredo.bautista@tut.fi.

Notes

The authors declare no competing financial interest.

■ ACKNOWLEDGMENTS

This work was supported by Grants 134973 and 135084 from the Academy of Finland. M.J.H. acknowledges support from the Graduate School of Modern Optics and Photonics in Finland and Emil Aaltonen Foundation. J.M. and J.M.K. acknowledge support from the Graduate School of the Tampere University of Technology.

■ REFERENCES

(1) Novotny, L.; Hecht, B. *Principles of Nano-Optics*; Cambridge University Press: New York, 2006.
(2) Novotny, L.; Bian, R. X.; Xie, X. S. *Phys. Rev. Lett.* **1997**, *79*, 645.
(3) Romero, I.; Aizpurua, J.; Bryant, G. W.; García De Abajo, F. J. *Opt. Express* **2006**, *14*, 9988.
(4) Tabor, C.; Van Haute, D.; El-Sayed, M. A. *ACS Nano* **2009**, *3*, 3670.

(5) Wang, H.; Wu, Y.; Lassiter, B.; Nehl, C. L.; Hafner, J. H.; Nordlander, P.; Halas, N. J. *Proc. Natl. Acad. Sci. U.S.A.* **2006**, *103*, 10856.
(6) Fedotov, V. A.; Rose, M.; Prosvirnin, S. L.; Papasimakis, N.; Zheludev, N. I. *Phys. Rev. Lett.* **2007**, *99*, 147401.
(7) Christ, A.; Martin, O. J. F.; Ekinci, Y.; Gippius, N. A.; Tikhodeev, S. G. *Nano Lett.* **2008**, *8*, 2171.
(8) Nelayah, J.; Kociak, M.; Stephan, O.; García de Abajo, F. J.; Tence, M.; Henrard, L.; Taverna, D.; Pastoriza-Santos, I.; Liz-Marzan, L. M.; Colliex, C. *Nat. Phys.* **2007**, *3*, 348.
(9) Vesseur, E. J. R.; De Waele, R.; Kuttge, M.; Polman, A. *Nano Lett.* **2007**, *7*, 2843.
(10) Olmon, R. L.; Krenz, P. M.; Jones, A. C.; Boreman, G. D.; Raschke, M. B. *Opt. Express* **2008**, *16*, 20295.
(11) Brüche, E. *Z. Phys.* **1933**, *86*, 448.
(12) Beversluis, M. R.; Bouhelier, A.; Novotny, L. *Phys. Rev. B* **2003**, *68*, 115433.
(13) Fleischer, M.; Stanciu, C.; Stade, F.; Stadler, J.; Braun, K.; Heeren, A.; Häffner, M.; Kern, D. P.; Meixner, A. J. *Appl. Phys. Lett.* **2008**, *93*, 111114.
(14) García de Abajo, F. J. *Rev. Mod. Phys.* **2010**, *82*, 209.
(15) Vogelgesang, R.; Dmitriev, A. *Analyst* **2010**, *135*, 1175.
(16) Bouhelier, A.; Beversluis, M. R.; Novotny, L. *Appl. Phys. Lett.* **2003**, *83*, 5041.
(17) Danckwerts, M.; Novotny, L. *Phys. Rev. Lett.* **2007**, *98*, 026104.
(18) Zayats, A. V.; Sandoghdar, V. *J. Microsc.* **2001**, *202*, 94.
(19) Butet, J.; Duboisset, J.; Bachelier, G.; Russier-Antoine, I.; Benichou, E.; Jonin, C.; Brevet, P.-F. *Nano Lett.* **2010**, *10*, 1717.
(20) Takahashi, S.; Zayats, A. V. *Appl. Phys. Lett.* **2002**, *80*, 3479.
(21) Bouhelier, A.; Beversluis, M.; Hartschuh, A.; Novotny, L. *Phys. Rev. Lett.* **2003**, *90*, 013903.
(22) Lippitz, M.; van Dijk, M. A.; Orrit, M. *Nano Lett.* **2005**, *5*, 799.
(23) Kim, S.; Jin, J.; Kim, Y.-J.; Park, I.-Y.; Kim, Y.; Kim, S.-W. *Nature* **2008**, *453*, 757.
(24) Canfield, B. K.; Husu, H.; Kontio, J.; Viheriälä, J.; Rytkönen, T.; Niemi, T.; Chandler, E.; Hrin, A.; Squier, J. A.; Kauranen, M. *New J. Phys.* **2008**, *10*, 013001.
(25) Husu, H.; Siikanen, R.; Mäkitalo, J.; Lehtolahti, J.; Laukkanen, J.; Kuittinen, M.; Kauranen, M. *Nano Lett.* **2012**, *12*, 673.
(26) Canfield, B. K.; Kujala, S.; Jefimovs, K.; Turunen, J.; Kauranen, M. *Opt. Express* **2004**, *12*, 5418.
(27) Canfield, B. K.; Husu, H.; Laukkanen, J.; Bai, B.; Kuittinen, M.; Turunen, J.; Kauranen, M. *Nano Lett.* **2007**, *7*, 1251.
(28) Feth, N; Linden, S.; Klein, M. W.; Decker, M.; Niesler, F. B. P.; Zeng, Y.; Hoyer, W.; Liu, J.; Koch, S. W.; Moloney, J. V.; Wegener, M. *Opt. Lett.* **2008**, *33*, 1975.
(29) Valev, V. K.; Smisdom, N.; Silhanek, A. V.; De Clercq, B.; Gillijns, W.; Ameloot, M.; Moshchalkov, V. V.; Verbiest, T. *Nano Lett.* **2009**, *9*, 3945.
(30) Huttunen, M. J.; Bautista, G.; Decker, M.; Linden, S.; Wegener, M.; Kauranen, M. *Opt. Mater. Express* **2011**, *1*, 46.
(31) Kontio, J. M.; Husu, H.; Simonen, J.; Huttunen, M. J.; Tommila, J.; Pessa, M.; Kauranen, M. *Opt. Lett.* **2009**, *34*, 1979.
(32) Wang, H.; Goodrich, G. P.; Tam, F.; Oubre, C.; Nordlander, P.; Halas, N. J. *J. Phys. Chem. B* **2005**, *109*, 11083.
(33) Canfield, B. K.; Kujala, S.; Laiho, K.; Jefimovs, K.; Turunen, J.; Kauranen, M. *Opt. Express* **2006**, *14*, 950.
(34) Husu, H.; Canfield, B. K.; Laukkanen, J.; Bai, B.; Kuittinen, M.; Turunen, J.; Kauranen, M. *Appl. Phys. Lett.* **2008**, *93*, 183115.
(35) Klein, M. W.; Enkrich, C.; Wegener, M; Linden, S. *Science* **2006**, *313*, 502.
(36) van Nieuwstadt, J. A. H.; Sandtke, M.; Harmsen, R. H.; Segerink, F. B.; Prangsma, J. C.; Enoch, S; Kuipers, L. *Phys. Rev. Lett.* **2006**, *97*, 146102.
(37) McMahon, M. D.; Lopez, R.; Haglund, R. F.; Ray, E. A.; Bunton, P. H. *Phys. Rev. B* **2006**, *73*, 041401.
(38) Kogelnik, H.; Li, T. *Appl. Opt.* **1966**, *5*, 1550.
(39) Youngworth, K. S.; Brown, T. G. *Opt. Express* **2000**, *7*, 77.
(40) Dorn, R.; Quabis, S.; Leuchs, G. *Phys. Rev. Lett.* **2003**, *91*, 233901.
(41) Novotny, L.; Beversluis, M. R.; Youngworth, K. S.; Brown, T. G. *Phys. Rev. Lett.* **2001**, *86*, 5251.
(42) Chizhik, A. I.; Chizhik, A. M.; Khoptyar, D.; Bär, S.; Meixner, A. J. *Nano Lett.* **2011**, *11*, 1131.
(43) Chizhik, A. M.; Chizhik, A. I.; Gutbrod, R.; Meixner, A. J.; Schmidt, T.; Sommerfeld, J.; Huisken, F. *Nano Lett.* **2009**, *9*, 3239.
(44) Failla, A. V.; Qian, H.; Qian, H.; Hartschuh, A.; Meixner, A. J. *Nano Lett.* **2006**, *6*, 1374.
(45) Züchner, T.; Failla, A. V.; Steiner, M.; Meixner, A. J. *Opt. Express* **2008**, *16*, 14635.
(46) Yew, E. Y. S.; Sheppard, C. J. R. *Opt. Commun.* **2007**, *275*, 453.
(47) Khunsin, W.; Brian, B.; Dorfmuller, J.; Esslinger, M.; Vogelgesang, R.; Etrich, C.; Rockstuhl, C.; Dmitriev, A.; Kern, K. *Nano Lett.* **2011**, *11*, 2765.
(48) Mäkitalo, J.; Suuriniemi, S.; Kauranen, M. *Opt. Express* **2011**, *19*, 23386.
(49) Johnson, P. B.; Christy, R. W. *Phys. Rev. B* **1972**, *6*, 4370.
(50) Juan, M. L.; Righini, M.; Quidant, R. *Nat. Photonics* **2011**, *5*, 349.

Publication V

Reprinted with permission from

R. Czaplicki, J. Mäkitalo, R. Siikanen, H. Husu, J. Lehtolahti, M. Kuittinen and M. Kauranen. Second-harmonic generation from metal nanoparticles: resonance enhancement versus particle geometry. Nano Letters, **15**, 530 – 534 (2015).

NANO LETTERS

Letter

pubs.acs.org/NanoLett

Second-Harmonic Generation from Metal Nanoparticles: Resonance Enhancement versus Particle Geometry

Robert Czaplicki,*[,†] Jouni Mäkitalo,[†] Roope Siikanen,[†] Hannu Husu,[†] Joonas Lehtolahti,[‡] Markku Kuittinen,[‡] and Martti Kauranen[†]

[†]Department of Physics, Tampere University of Technology, P.O. Box 692, FI-33101 Tampere, Finland

[‡]Institute of Photonics, University of Eastern Finland, P.O. Box 111, FI-80101 Joensuu, Finland

Supporting Information

ABSTRACT: We demonstrate that optical second-harmonic generation (SHG) from arrays of noncentrosymmetric gold nanoparticles depends essentially on particle geometry. We prepare nanoparticles with different geometrical shapes (L and T) but similar wavelengths for the polarization-dependent plasmon resonances. In contrast to recent interpretations emphasizing resonances at the fundamental frequency, the T shape leads to stronger SHG when only one, instead of both, polarization component of the fundamental field is resonant. This is explained by the character of plasmon oscillations supported by the two shapes. Our numerical simulations for both linear and second-order responses display unprecedented agreement with measurements.

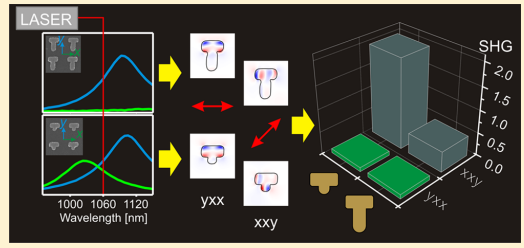

KEYWORDS: *Metal nanoparticles, nonlinear optics, second-harmonic generation, plasmonic resonances*

The interaction of light with metal nanoparticles can be described in terms of collective oscillations of conduction electrons, giving rise to localized surface plasmon resonances (LSPRs).[1] The properties of LSPRs can be tuned widely by changing the size, shape, and dielectric environment of the particles.[2] When the particles are arranged in arrays, the overall response is also affected by the coupling between the individual particles.[3−6]

An important consequence of LSPRs is the strong enhancement of the local electromagnetic fields ("hot spots"), which can boost nonlinear optical effects in nanostructures.[7,8] One of the nonlinear effects that can be enhanced is second-harmonic generation (SHG), which converts two photons at a fundamental frequency into one photon at the doubled frequency. As an even-order nonlinear process, SHG is limited by the noncentrosymmetry requirement of the material structure. This condition is most convenient to achieve with structures that look noncentrosymmetric even when viewed at normal incidence. The samples can then be investigated at normal incidence, such that the incoming and outgoing optical fields have components mostly in the sample plane. This ensures that the fields would not couple to the (traditional) surface nonlinearity of, for example, a bare sample substrate, which has a strong out-of-plane character. In consequence, the nonlinear responses must arise from the designed symmetry of the nanostructure.

A large variety of noncentrosymmetric metal nanostructures have been investigated by SHG during the past decade, including L-shaped,[9,10] T-shaped,[11] and G-shaped[12−14] particles, split-ring resonators (SRRs),[15] dimers,[16,17] oligomers,[18] nanocups,[19] or even more complicated shapes.[20] The importance of LSPRs at the fundamental[20−24] and/or second-harmonic frequency[20,22−24] has also been emphasized. The strong nonlinear response requires a LSPR at the fundamental frequency,[22] yet it is possible to use resonances at multiple wavelengths.[23] However, the resonance at the second-harmonic frequency has also been considered to be a loss mechanism, at least for the case of gold SRRs.[22]

Importantly, the strong local fields associated with plasmon resonances cannot overcome the noncentrosymmetry requirement. This is particularly evident for nanodimers separated by a nanogap. Nanogaps can give rise to very strong local fields, nevertheless, centrosymmetric dimers suppress SHG very efficiently.[25] In addition, the relation between plasmon resonances, particle symmetry, and associated local-field distributions can be very complicated.[26] Symmetry breaking is also essentially a qualitative concept. It is therefore a completely open question how the geometry of various noncentrosymmetric shapes and their plasmon resonances affect the second-order nonlinear response and how this response can be most efficiently utilized.

In this Letter, we investigate this crucial question by using arrays of noncentrosymmetric nanoparticles of different geometrical shapes and show that their SHG response cannot be understood only in terms of resonance effects. Instead, the

Received: October 10, 2014
Revised: December 15, 2014
Published: December 18, 2014

DOI: 10.1021/nl503901e
Nano Lett. 2015, 15, 530−534

directions of plasmon oscillations supported by the particle geometry and associated local-field distributions play an essential role. In order to show this, we prepare arrays with L- and T-shaped particles, both having at least one resonance close to the fundamental wavelength. In contrast to earlier interpretations, we find that the strongest SHG responses are not necessarily associated with optimizing the resonances for the fundamental field. In some cases, the resonance conditions need to be compromised in order to obtain a favorable coupling of the plasmonic oscillations to the second-order response.

Our samples consist of arrays of 20 nm thick gold nanoparticles fabricated by standard electron-beam lithography and lift-off techniques. As a substrate, we use a 0.5 mm thick fused silica plate coated with 4 nm thick chromium adhesion layer. The particles are covered by a 20 nm thick protective layer of fused silica. We choose particles of different noncentrosymmetric geometries (L- and T-shapes) that have strongly dichroic resonances for light polarized along the *x*- and *y*-axes as defined in Figure 1. The particles are arranged in

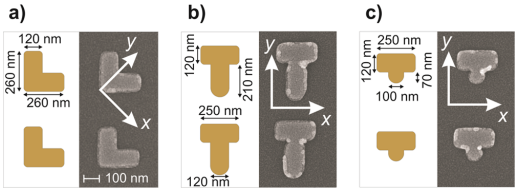

Figure 1. Design and scanning electron microscopy images of (a) sample L, (b) sample T_b, and (c) sample T_s. The coordinate systems, dimensions, and scale bar are also shown.

square arrays of 500 nm period. The reference sample (sample L) consists of the L-shaped nanoparticles with symmetric arms of width 120 nm and length 260 nm (Figure 1a).[6,10] The T-shaped particles (samples T_b and T_s) have the upper horizontal section of the same geometry, width 120 nm and length 250 nm, but the lower vertical section is different. It is either 120 nm wide and 210 nm long in the case of sample T_b (Figure 1b) or 100 nm wide and 70 nm long in the case of sample T_s (Figure 1c). Such geometries result in either *x*- or *y*-polarized resonances or both to be near the wavelength of the laser used in our SHG experiments (1060 nm).

The linear spectra of the samples were determined by measuring their extinction at normal incidence for *x* and *y* polarizations (Figure 2). Light from a halogen bulb was coupled to an optical fiber and then collimated using a microscope

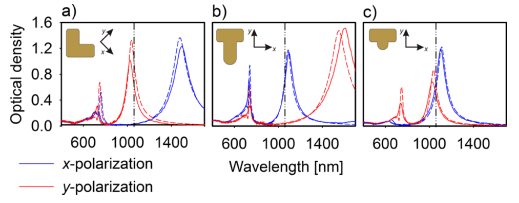

Figure 2. Polarized extinction spectra of (a) sample L, (b) sample T_b, and (c) sample T_s. The solid lines denote measured spectra and dashed lines the calculated ones. The fundamental wavelength of our laser (1060 nm) is marked as vertical dash-dotted line. Coordinate systems and particle geometries are shown as insets.

objective and pinhole in front of the sample. The light after the sample was focused to another fiber with a lens and directed to a spectrometer (Avantes AvaSpec-2048 for visible and Avantes NIR256 for infrared spectral range).

Sample L exhibits resonances for *x*- and *y*-polarized light at the wavelengths of 1494 and 1023 nm, respectively. The latter resonance is thus close to the fundamental wavelength of the SHG experiments (1060 nm). Sample T_b also has spectrally well-separated resonances. The *x*-polarized resonance at 1096 nm is now near the fundamental wavelength, but the *y*-polarized resonance is at a longer wavelength (1611 nm). For sample T_s, both resonances are near the fundamental wavelength, the resonance wavelengths being 1105 nm for *x*- and 1023 nm for *y*-polarization. The resonances closest to the laser wavelength do differ somewhat in their strength. However, the laser wavelength is within one-half line width from the line center for each case. All samples have additional resonances at around 760 nm that are related to plasmon oscillations along the width of the arms (L)[27] or sections (T_b, T_s) and to higher order modes.

The SHG measurements were performed in transmission at normal incidence using an Nd:glass laser (200 fs pulses at 1060 nm wavelength, average output power 150 mW, 82 MHz) as a source of fundamental light. The laser beam was weakly focused and its polarization was cleaned with a high-quality Glan polarizer. A half-wave plate was used to change the linear input polarization, while the analyzer in front of the detector allowed only one selected polarization component of the second-harmonic field to be detected.

The symmetry group of all samples is C_{1v}, which allows nonvanishing SHG signals for the in-plane components *yyy*, *yxx*, and *xxy* = *xyx* of the nonlinear response tensor,[28] which describes the effective nonlinearity of the whole sample. Here, the first letter refers to the polarization of SHG radiation and the two last letters describe the polarization of the fundamental field. The forbidden tensor components, for example, *xxx* and *xyy*, are very low as are the SHG signals related to them, also indicating high quality of the samples.[10] Note that for the case of mixed input polarizations, the allowed tensor components *yyy* and *yxx*, which can be determined individually by using *y*- or *x*-polarized input light, respectively, give rise to *y*-polarized signals. However, the mixed input polarizations are only used to access the tensor component *xxy* = *xyx* by detecting *x*-polarized light.

The results for SHG measurement are summarized in Figure 3. SHG from arrays of L-shaped gold nanoparticles has been previously studied,[10] thus such a sample is a well-understood reference for the present work. Consequently, the SHG signals in Figure 3 were normalized to the dominant tensor component *yyy* of sample L, for which the polarization of the

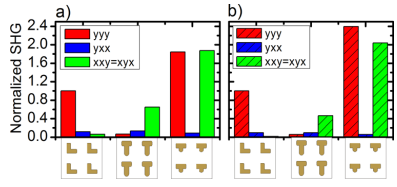

Figure 3. (a) Measured and (b) calculated from the near field distribution, SHG signals from studied samples normalized to *yyy* component of sample L.

DOI: 10.1021/nl503901e
Nano Lett. 2015, 15, 530−534

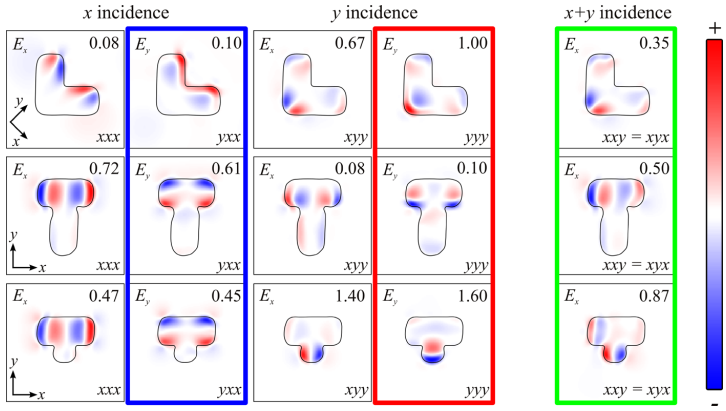

Figure 4. *x*- and *y*-polarization components of the near fields at the second-harmonic wavelength calculated at a plane 15 nm after the gold nanoparticles. The shown quantity corresponds to the real part of the field at a moment when the real part of the strongest spot is maximum. Sample L (top row), sample T_b (middle row), and sample T_s (bottom row) for *x*-polarized, *y*-polarized, and *x* + *y* polarized input beam at the fundamental wavelength, respectively. The numbers in the right upper corners show the maximum field amplitudes normalized to that for the *yyy* component of L. The input polarizations are indicated above the figures and the calculated SHG components are shown in the left upper corners. The labels in the right bottom corner show the tensor components that contribute to each panel. The near fields related to allowed tensor components are framed with thick blue, red, and green lines, where the colors represent the colors of SHG signals from Figure 3 (and Figure S2 in Supporting Information).

fundamental wavelength (*y*) is resonant. We thus have a double resonance at the fundamental wavelength in the sense that both field components corresponding to the two last indices of the tensor component are resonant. When the incident polarization is nonresonant (*x*), the allowed component (*yxx*) is very weak. The component with mixed input polarizations (*xxy* = *xyx*, one resonant and one nonresonant), however, is even weaker (Figure 3) as observed also in earlier studies.[6] This result already deviates from the expectation that the resonance characteristics can be used to explain the SHG responses of metal nanostructures.

For sample T_b, the *y*-polarized fundamental wavelength is nonresonant and the allowed component *yyy* is weak. The allowed, doubly resonant component *yxx* is expected to have strong SHG signal if only resonance characteristics and symmetry rules are considered, but this component is weak as well. On the other hand, the fundamental field containing both *x* and *y* components (*xxy* = *xyx*) gives rise to the only strong SHG signal for sample T_b.

The incident field of sample T_s is always resonant since the *x*- and *y*-polarized resonances are close to the wavelength of our laser (see Figure 2c). Hence, all the allowed components are expected to yield strong SHG signals on the basis of resonance considerations. However, only the components *xxy* = *xyx* and *yyy* have strong SHG signals, and these signals are exceptionally strong. The component *yxx*, which is also allowed, however, has a much weaker SHG signal.

At first sight, these results are surprising, because they do not agree with the expectation that plasmonic resonances at the fundamental frequency are beneficial for the nonlinear responses.[22] Focusing solely on resonances, however, neglects an additional important factor that the total SHG response of a particle is obtained by integrating the local response over the particle shape. In consequence, the local-field distributions play an important, yet subtle, role in determining the integrated response. In order to understand the second-harmonic responses from our samples, we model their extinction spectra, SHG local fields and far-field SHG signals using the boundary element method (BEM)[29−38] where we also take into account the periodicity and the substrate.

So as to replicate experimental conditions in the calculations as well as possible, we used the outlines of the particles from the SEM images instead of the ideal shapes to model the geometry. The comparison in Figure 2 between the extinction spectra shows very good quantitative agreement between the measured and simulated results, which is essential for the reliable simulation of the SHG measurements (Figure 3b).

We simulated the SHG from the structures by considering only the dominant susceptibility component χ_{nnn} of the local response of the metal−air interfaces, where *n* is the direction of the local surface normal.[16,39,40] The generated SHG near fields were calculated on a plane 15 nm from the particle toward the detector. This allows us to intuitively study how the observed overall SHG signals are built up from the local responses. According to the Rayleigh−Sommerfeld diffraction theory

$$S_i = \left| \int E_i dS \right|^2, \quad i = x, y, z$$

where S_i is the far-field signal for the field component *i*, E_i is the respective second-harmonic field component, and the integration is over the plane of Figure 4. We used this equation to arrive at the signals shown in Figure 3b once the near fields had been obtained from the BEM modeling.

This equation also shows that even strong local responses cancel in the total signal if they produce out-of-phase SHG wavelets in the far-field.[25] This occurs when equal hot spots are obtained on symmetrically opposite sides of the particle, where the local surface normals point in opposite directions, and one is interested in the total signal polarized in the direction of this particular surface normal.

Our calculations were performed for the fundamental wavelength of the laser used in the experiment, which is 1060 nm. Note that the results for the overall SHG signals (Figure 3b) exhibit essentially quantitative agreement between the

DOI: 10.1021/nl503901e
Nano Lett. 2015, 15, 530−534

experiment and theory for all the samples investigated. The minor differences can be attributed to small deviations in the exact wavelengths and strengths of the plasmon resonances between experiment and modeling. Particularly, such differences can affect the results in the case of sample T_s, where both resonances are close to each other and to the fundamental wavelength. To confirm this, we repeated the calculations for the wavelength 1068 nm where the simulated relative optical densities for the two resonances match better with those for the 1060 nm in the experiment (Supporting Information, Figure S1). The agreement between the experiment and calculations is then even higher (Supporting Information, Figure S2).

The calculated SHG near fields (Figure 4) provide a simple physical interpretation of how the near fields add up in the measured overall signals. The salient features of this approach are easiest to understand by considering the *xxx* component, which is forbidden by symmetry for all samples. Although the *x*-polarized SHG near fields are strong for the two T particles, they are out-of-phase at the left and right ends of the horizontal section, thus interfering destructively in the measured far-field signal.[41]

For sample L, the *x*-polarized input field is nonresonant and the hot spots are weak, giving rise to weak SHG signals (*yxx* component of L in Figure 4). The *y*-polarized input field, oscillating along the arms of the L, results in hot spots at the end of the arms and at the corner of the L. The *y*-component of the latter hot spot (red) is by far the strongest, whereas the out-of-phase parts (blue) remain weak, thus leading to strong *y*-polarized SHG radiation (*yyy* component of L in Figure 4). When the input field is polarized along one of the arms ($x + y$ incidence of L), the hot spots reproduce those for the *y*-polarized input, because only this input component is resonant. However, the *x*-components of these hot spots have essentially symmetric out-of-phase parts, which give rise to only very weak over component $xxy = xyx$, as also evident in Figure 3.

The specific particle geometry of sample T_b and *x*-polarized input field leads to plasmon oscillations mainly along the horizontal section. This gives rise to strong hot spots at the ends of the section. However, the *y*-polarized near fields have approximately equal in-phase and out-of-phase parts, thus suppressing the measured overall SHG signal from component *yxx*. We emphasize that this suppression occurs even though the *x*-polarized input is resonant and the component is allowed. The oscillations caused by *y*-polarized input field, which is nonresonant, result only in weak hot spots at the ends (corners) of the horizontal section. Consequently, the overall SHG signal remains weak for the *yyy* component of sample T_b (Figure 3). The mixed input polarization $x + y$ supports asymmetry of hot spots across the total shape of the particle. Although only the *x*-component of the input field is resonant, the strong asymmetry of the *x*-polarized local field gives rise to a reasonably strong overall signal for tensor component $xxy = xyx$. Importantly, this signal is much stronger than that from the doubly resonant *yxx* component.

The particle shape of sample T_s is similar to that of sample T_b. The main difference is in the vertical section, which is now replaced by a shorter and narrower one. Such a change tunes the *y*-polarized resonance to a shorter wavelength, so that both input polarizations are near-resonant. The *x*-polarized resonance is almost at the same wavelength as for sample T_b and the optical density levels are comparable. Such similarity leads to analogous result for *yxx* component of sample T_s, which is weak due to the cancellation of the SHG fields. For *y*-polarized input field, very strong hot spots appear at the bottom part of the vertical section. The *y*-polarized hot spot is highly asymmetric in *y*-direction, which leads to a strong signal from component *yyy*. As a result, the *yyy* SHG signal from sample T_s is twice as strong as from sample L (Figure 3). Similarly to sample T_b, the input field polarized in $x + y$ direction causes strong asymmetry of hot spots across the entire particle (Figure 4). In this case, both input polarizations are resonant and the fields couple favorably with component $xxy = xyx$, which also leads to twice as strong SHG signal as the dominant signal from sample L. Note also that, compared to the amount of nonlinear material used, sample T_s is about a factor of 2.5 more efficient nonlinear generator than sample L.

The above analysis shows that although L- and T-shaped nanoparticles belong to the same symmetry group and have at least one of the resonances near the fundamental wavelength, the second-harmonic responses from such structures are quite different. In fact, the behavior of the T-shaped nanoparticles is rather peculiar. When illuminated with *x*-polarized light, the SHG signals from relatively strong hot spots cancel, leading to a weak total signal. In other words, this geometry is not favorable for cross coupling between oscillations in the *x*- and *y*-directions, which would be required for the allowed SHG signal represented by component *yxx*. This occurs because the T-geometry allows a direct oscillation along its horizontal section. In this respect, the T-particles behave for *x* polarization very similarly as a plain horizontal bar for which SHG is forbidden by symmetry. Consequently, the existence of a resonance at the fundamental wavelength brings no benefit for the generation of a strong SHG signal. Interesting is also the strong *x*-polarized SHG generated by $x + y$-polarized input field. Some of the local-field components in this case are weaker than under doubly resonant conditions. However, the loss in the strength of the field components is more than compensated by the asymmetry of hot spots, which leads to better optimization of the local-field distributions in the nanostructure. The latter case can be also associated with rotation of polarization in SHG, which is possible for samples of certain symmetry.[42] Our T_s particles do not deviate very much from triangles, which belong to the symmetry group D_3. Similarly to the results reported by Konishi et al., T_s is able to rotate incident polarization by 45° in SHG.

In conclusion, we have shown that particle geometry combined with the polarization of the incident field play crucial roles in second-harmonic generation from arrays of metal nanoparticles. The nonlinear response can therefore not be explained simply by plasmonic resonance enhancement of either fundamental or second-harmonic fields, especially when particles of different geometry are compared. In the present work, the most striking result is the symmetry allowed *yxx* component of T-shaped samples. On the basis of resonances and overall symmetry rules only, the SHG signal should be high due to the fact that the fundamental *x*-polarization is resonant and the hot spots of the local field are strong. However, the geometry of the particle leads to cancellation of the strong local signals from the hot spots and thus the overall SHG signal from *yxx* is weak. On the other hand, a weaker field with only one resonant component is sufficient to yield a strong SHG signal. The geometry of the particles therefore supersedes the resonant effects. This issue needs to be carefully considered when new types of nanostructures are designed for strong nonlinear optical responses. In order to obtain efficient strong nonlinear

DOI: 10.1021/nl503901e
Nano Lett. 2015, 15, 530−534

response, the geometry of nanostructures needs to be designed to support plasmon resonances and optimized local fields.

■ ASSOCIATED CONTENT

Supporting Information

Table with the details of the plasmon resonances of the samples, the extinction spectra of sample T_s, and the calculated second-harmonic signals at a wavelength slightly detuned from the actual laser wavelength. This material is available free of charge via the Internet at http://pubs.acs.org.

■ AUTHOR INFORMATION

Corresponding Author

*E-mail: robert.czaplicki@tut.fi.

Present Address

(H.H.) nLIGHT Corporation, Sorronrinne 9, FI-08500 Lohja, Finland

Notes

The authors declare no competing financial interest.

■ ACKNOWLEDGMENTS

This work was supported by the Academy of Finland (132438, 265682). J.M. acknowledges the Graduate School of Tampere University of Technology for funding.

■ REFERENCES

(1) Kauranen, M.; Zayats, A. V. *Nat. Photon* **2012**, *6*, 737−748.
(2) Maier, S. A. *Plasmonics: Fundamentals and Applications*; Springer: New York, 2007.
(3) Zhao, L.; Kelly, K. L.; Schatz, G. C. *J. Phys. Chem. B* **2003**, *107*, 7343−7350.
(4) Auguié, B.; Barnes, W. L. *Phys. Rev. Lett.* **2008**, *101*, 143902.
(5) Chu, Y.; Schonbrun, E.; Yang, T.; Crozier, K. B. *Appl. Phys. Lett.* **2008**, *93*, 181108.
(6) Husu, H.; Siikanen, R.; Mäkitalo, J.; Lehtolahti, J.; Laukkanen, J.; Kuittinen, M.; Kauranen, M. *Nano Lett.* **2012**, *12*, 673−677.
(7) Li, K.; Stockman, M. I.; Bergman, D. J. *Phys. Rev. Lett.* **2003**, *91*, 227402.
(8) Stockman, M. I.; Bergman, D. J.; Anceau, C.; Brasselet, S.; Zyss, J. *Phys. Rev. Lett.* **2004**, *92*, 057402.
(9) Canfield, B.; Kujala, K.; Jefimovs, K.; Turunen, J.; Kauranen, M. *Opt. Express* **2004**, *12*, 5418−5423.
(10) Czaplicki, R.; Zdanowicz, M.; Koskinen, K.; Laukkanen, J.; Kuittinen, M.; Kauranen, M. *Opt. Express* **2011**, *19*, 26866−26871.
(11) (a) Klein, M. W.; Wegener, M.; Feth, N.; Linden, S. *Opt. Express* **2007**, *15*, 5238−5247;(b) *Opt. Express* **2008**, *16*, 8055−8055.
(12) Valev, V. K.; Silhanek, A. V.; Verellen, N.; Gillijns, W.; Van Dorpe, P.; Aktsipetrov, O. A.; Vandenbosch, G. A. E.; Moshchalkov, V. V.; Verbiest, T. *Phys. Rev. Lett.* **2010**, *104*, 127401.
(13) Valev, V. K.; Zheng, X.; Biris, C. G.; Silhanek, A. V.; Volskiy, V.; De Clercq, B.; Aktsipetrov, O. A.; Ameloot, M.; Panoiu, N. C.; Vandenbosch, G. A. E.; Moshchalkov, V. V. *Opt. Mater. Express* **2011**, *1*, 36−45.
(14) Valev, V. K. *Langmuir* **2012**, *28*, 15454−15471.
(15) Klein, M. W.; Enkrich, C.; Wegener, M.; Linden, S. *Science* **2006**, *313*, 502−504.
(16) Canfield, B. K.; Husu, H.; Laukkanen, J.; Bai, B.; Kuittinen, M.; Turunen, J.; Kauranen, M. *Nano Lett.* **2007**, *7*, 1251−1255.
(17) Husu, H.; Canfield, B. K.; Laukkanen, J.; Bai, B.; Kuittinen, M.; Turunen, J.; Kauranen, M. *Appl. Phys. Lett.* **2008**, *93*, 183115.
(18) Thyagarajan, K.; Butet, J.; Martin, O. J. F. *Nano Lett.* **2013**, *13*, 1847−1851.
(19) Zhang, Y.; Grady, N. K.; Ayala-Orozco, C.; Halas, N. J. *Nano Lett.* **2011**, *11*, 5519−5523.
(20) Aouani, H.; Navarro-Cia, M.; Rahmani, M.; Sidiropoulos, T. P. H.; Hong, M.; Oulton, R. F. O.; Maier, S. A. *Nano Lett.* **2012**, *12*, 4997−5002.
(21) McMahon, M. D.; Ferrara, D.; Bowie, C. T.; Lopez, R.; Haglund, R. F., Jr. *Appl. Phys., B* **2007**, *87*, 256−265.
(22) Niesler, F. B. P.; Feth, N.; Linden, S.; Wegener, M. *Opt. Lett.* **2011**, *36*, 1533−1535.
(23) Thyagarajan, K.; Rivier, S.; Lovera, A.; Martin, O. J. F. *Opt. Express* **2012**, *20*, 12860−12865.
(24) Park, S.; Hahn, J. W.; Lee, J. Y. *Opt. Express* **2012**, *20*, 4856−4870.
(25) Berthelot, J.; Bachelier, G.; Song, M.; Rai, P.; Colas des Francs, G.; Dereux, A.; Bouhelier, A. *Opt. Express* **2012**, *20*, 10498−10508.
(26) Ross, B. M.; Lee, L. P. *Opt. Lett.* **2009**, *34*, 896−898.
(27) Husu, H.; Mäkitalo, J.; Laukkanen, J.; Kuittinen, M.; Kauranen, M. *Opt. Express* **2010**, *18*, 16601−16606.
(28) Canfield, B.; Kujala, S.; Jefimovs, K.; Svirko, Y.; Turunen, J.; Kauranen, M. *J. Opt. A* **2006**, *8*, S278−S284.
(29) Rao, S.; Wilton, D.; Glisson, A. *IEEE Trans. Antennas Propag.* **1982**, *30*, 409−418.
(30) Umashankar, K.; Taflove, A.; Rao, S. M. *IEEE Trans. Antennas Propag.* **1986**, *34*, 758−766.
(31) Harrington, R. F. *Field Computation by Moment Methods*; Wiley-IEEE Press: New York, 1993.
(32) Aizpurua, J.; Hanarp, P.; Sutherland, D. S.; Käll, M.; Bryant, G. W.; García de Abajo, F. J. *Phys. Rev. Lett.* **2003**, *90*, 057401.
(33) Romero, I.; Aizpurua, J.; Bryant, G. W.; García De Abajo, F. J. *Opt. Express* **2006**, *14*, 9988−9999.
(34) Bryant, G. W.; García de Abajo, F. J.; Aizpurua, J. *Nano Lett.* **2008**, *8*, 631−636.
(35) Kern, A. M.; Martin, O. J. F. *J. Opt. Soc. Am. A* **2009**, *26*, 732−740.
(36) Mäkitalo, J.; Suuriniemi, S.; Kauranen, M. *Opt. Express* **2011**, *19*, 23386−23399.
(37) Forestiere, C.; Capretti, A.; Miano, G. *J. Opt. Soc. Am. B* **2013**, *30*, 2355−2364.
(38) Butet, J.; Gallinet, B.; Thyagarajan, K.; Martin, O. J. F. *J. Opt. Soc. Am. B* **2013**, *30*, 2970−2979.
(39) Wang, F. X.; Rodriguez, F. J.; Albers, W. M.; Ahorinta, R.; Sipe, J. E.; Kauranen, M. *Phys. Rev. B* **2009**, *80*, 233402.
(40) Bachelier, G.; Butet, J.; Russier-Antoine, I.; Jonin, C.; Benichou, E.; Brevet, P.-F. *Phys. Rev. B* **2010**, *82*, 235403.
(41) Butet, J.; Thyagarajan, K.; Martin, O. J. F. *Nano Lett.* **2013**, *13*, 1787−1792.
(42) Konishi, K.; Higuchi, T.; Li, J.; Larsson, J.; Ishii, S.; Kuwata-Gonokami, M. *Phys. Rev. Lett.* **2014**, *112*, 135502.

DOI: 10.1021/nl503901e
Nano Lett. 2015, 15, 530−534

Tampereen teknillinen yliopisto
PL 527
33101 Tampere

Tampere University of Technology
P.O.B. 527
FI-33101 Tampere, Finland

ISBN 978-952-15-3522-2
ISSN 1459-2045